Lecture 1

Scope of Boundary Layer (BL) Meteorology

In classical fluid dynamics, a boundary layer is the layer in a nearly inviscid fluid next to a surface in which frictional drag associated with that surface is significant (term introduced by Prandtl, 1905). Such boundary layers can be *laminar* or *turbulent*, and are often only mm thick.

In atmospheric science, a similar definition is useful. The *atmospheric boundary layer* (ABL, sometimes called P[lanetary] BL) is the layer of fluid directly above the Earth's surface in which significant fluxes of momentum, heat and/or moisture are carried by turbulent motions whose horizontal and vertical scales are on the order of the boundary layer depth, and whose circulation timescale is a few hours or less (Garratt, p. 1). A similar definition works for the ocean.

The complexity of this definition is due to several complications compared to classical aerodynamics.

i) Surface heat exchange can lead to thermal convection

ii) Moisture and effects on convection

iii) Earth's rotation

iv) Complex surface characteristics and topography.

BL is assumed to encompass surface-driven dry convection. Most workers (but not all) include shallow cumulus in BL, but deep precipitating cumuli are usually excluded from scope of BLM due to longer time for most air to recirculate back from clouds into contact with surface.

Air-surface exchange

BLM also traditionally includes the study of fluxes of heat, moisture and momentum between the atmosphere and the underlying surface, and how to characterize surfaces so as to predict these fluxes (roughness, thermal and moisture fluxes, radiative characteristics). Includes plant canopies as well as water, ice, snow, bare ground, etc.

Characteristics of ABL

The boundary layer itself exhibits dynamically distinct sublayers

i) Interfacial sublayer - in which molecular viscosity/diffusivity dominate vertical fluxes

ii) Inertial layer - in which turbulent fluid motions dominate the vertical fluxes, but the dominant scales of motion are still much less than the boundary layer depth. This is the layer in which most surface wind measurements are made.

- Layers (i) + (ii) comprise the surface layer. Coriolis turning of the wind with height is not evident within the surface layer.

iii) Outer layer - turbulent fluid motions with scales of motion comparable to the boundary layer depth ('large eddies').

- At the top of the outer layer, the BL is often capped by an *entrainment zone* in which turbulent BL eddies are entraining non-turbulent free-atmospheric air. This entrainment zone is often associated with a stable layer or inversion.
- For boundary layers topped by shallow cumulus, the outer layer is subdivided further into

subcloud, transition, cumulus and inversion layer.

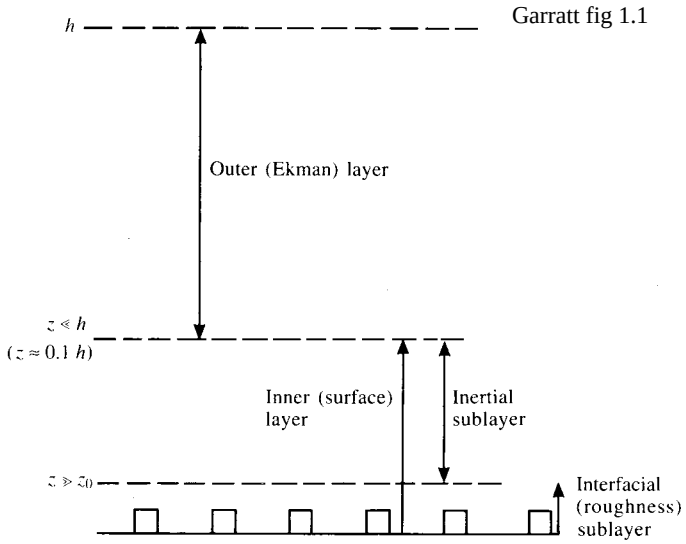

Boundary layers are classified as *unstable* if the air moving upward in the turbulent motions tends to be buoyant (less dense) than in the downdrafts, and *stable* if the reverse is true. If there is negligible buoyancy transport within the BL, it is called *neutral*. On a hot sunny morning, surface heating causes the boundary layer to become strongly unstable, and convect vigorously with outer layer updrafts of 1-3 m s^{-1} which are a few tenths of a K warmer than the downdrafts, transporting several hundred W m^{-2} of heat upward. In desert regions such BLs can grow to a depth of 5 km or more by afternoon, though typical summer early afternoon BL depths over Midwest, Seattle, etc. are 1-2 km. At night, the surface cools by radiation. The BL depth can become as little as 50 m on a clear calm night, and the BL tends to be *stable*, with weak downward buoyancy fluxes. Rarely is an ideal neutral ABL observed, but with strong winds, buoyancy effects can become relatively unimportant, especially for winds over the oceans blowing along contours of constant SST.

Typical ABLs over the ocean tend to be slightly unstable, with little diurnal cycle due to the near-constancy of SST. BL depths vary from a few hundred m in regions of warm advection to 1.5-3 km where cold advection has led to shallow cumuli (subtropical trade wind belts, cold air outbreaks). In regions of deep convection, a BL top can be difficult to define.

Within the ocean, there is also an oceanic BL driven by surface wind stress and sometimes convection, and considerably affected by the absorption of radiation in the upper ocean. It is usually but not always stable. The oceanic BL can vary from a few m deep to a few km deep in isolated locations (e. g. Labrador Sea) and times where oceanic deep convection is driven by intense cold air advection overhead.

Applications and Relevance of BLM

The boundary layer is the part of the atmosphere in which we live and carry out most human activities. Furthermore, almost all exchange of heat, moisture, momentum, naturally occurring particles, aerosols, and gasses, and pollutants occurs through the BL. Specific applications

i) *Climate simulation and NWP* - parameterization of surface characteristics, air-surface exchange, BL thermodynamics fluxes and friction, and cloud. No climate model can succeed without some consideration of the boundary layer. In NWP models, a good boundary layer is critical to proper prediction of the diurnal cycle, of low-level winds and convergence, of

effects of complex terrain, and of timing and location of convection. Coupling of atmospheric models to ocean, ice, land-surface models occurs through BL processes.

ii) *Air Pollution and Urban Meteorology* - Pollutant dispersal, interaction of BL with mesoscale circulations. Urban heat island effects.

iii) *Agricultural meteorology* - Prediction of frost, dew, evapotranspiration.

iv) *Aviation* - Prediction of fog formation and dissipation, dangerous wind-shear conditions.

v) *Remote Sensing* - Satellite-based measurements of surface winds, skin temperature, etc. involve the interaction of BL and surface, and must often be interpreted in light of a BL model to be useful for NWP.

History of BLM

1900 - 1910 • Development of laminar boundary layer theory for aerodynamics, starting with a seminal paper of Prandtl (1904).
• Ekman (1905,1906) develops his theory of laminar Ekman layer.

1910 - 1940 • Taylor develops basic methods for examining and understanding turbulent mixing
• Mixing length theory, eddy diffusivity - von Karman, Prandtl, Lettau

1940 - 1950 • Kolmogorov (1941) similarity theory of turbulence

1950 - 1960 • Buoyancy effects on surface layer (Monin and Obuhkov, 1954)
• Early field experiments (e. g. Great Plains Expt. of 1953) capable of accurate direct turbulent flux measurements

1960 - 1970 • The Golden Age of BLM. Accurate observations of a variety of boundary layer types, including convective, stable and trade-cumulus. Verification/calibration of surface similarity theory.

1970 - 1980 • Introduction of resolved 3D computer modelling of BL turbulence (large-eddy simulation or LES). Application of higher-order turbulence closure theory.

1980 - 1990 • Major field efforts in stratocumulus-topped boundary layers (FIRE, 1987) and land-surface, vegetation parameterization. Mesoscale modeling.

1990 - The Age of Technology
• New surface remote sensing tools (lidar, cloud radar) and extensive space-based coverage of surface characteristics;
• LES as a tool for improving parameterizations and bridging to observations.
• Coupled ocean-atmosphere-ice-biosphere and medium-range forecast models create stringent accuracy requirements for BL parameterizations.
• Accurate routine mesoscale modelling for urban air flow; coupling to air pollution
• Boundary layer - deep convection interactions (e. g. TOGA-COARE, 1992)

Why is the boundary layer turbulent?

We characterize the BL by turbulent motions, but we could imagine a laminar BL in which there is a smooth transition from the free-tropospheric wind speed to a no-slip condition against a surface (e .g. a laminar Ekman layer). Such a BL would have radically different characteristics than are observed.

Steady Ekman BL equations (z = height, surface at $z = 0$, free troposphere is z) :

$$-fv = \nu \, d^2u/dz^2$$

$$f(u - G) = \nu \, d^2v/dz^2$$

$$u(0) = 0, \; u(\infty) = G$$

$$v(0) = 0, \; v(\infty) = 0$$

Solution ($\zeta = z/\delta$) for BL velocity profile

$$u(z) = G(1 - e^{-\zeta} \cos \zeta)$$

$$v(z) = G \, e^{-\zeta} \sin \zeta$$

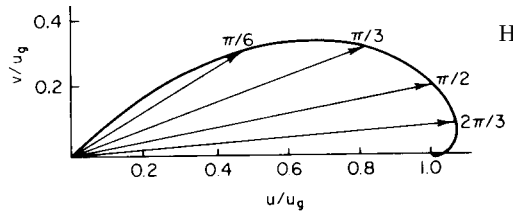

Holton, fig. 5.4

Fig. 5.4 Hodograph of the wind components in the Ekman spiral solution. The arrows show the velocity vectors for several levels in the Ekman layer, while the spiral curve traces out the velocity variation as a function of height. Points labeled on the spiral show the values of γz, which is a nondimensional measure of height.

Flow adjusts nearly to geostrophic within Ekman layer depth $\delta = (2\nu/f)^{1/2}$ of the surface.With a free tropospheric (geostrophic) velocity of G in the x direction, the kinematic molecular viscosity of air $\nu = 1.4\times10^{-5}$ m^2 s^{-1} and a Coriolis parameter $f = 10^{-4}$ s^{-1} , $\delta =$ 0.5 m, which is far thinner than observed!

Hydrodynamic Instability

Laminar BLs like the Ekman layer are not observed in the atmosphere because they are *hydrodynamically unstable*, so even if we could artificially set such a BL up, perturbations would rapidly grow upon it and modify it toward a more realistic BL structure. Three forms of hydrodynamic instability are particularly relevant to BLs:

i) Shear instability

ii) Kelvin-Helmholtz instability

iii) Convective (Rayleigh-Benard) instability

By examining these types of instability, we can not only understand why laminar boundary layers are not observed, but also gain insight into some of the turbulent flow structures that are observed. The

Shear Instability

Instability of an unstratified shear flow $U(z)$ occuring at high Reynolds numbers Re = VL/ν,

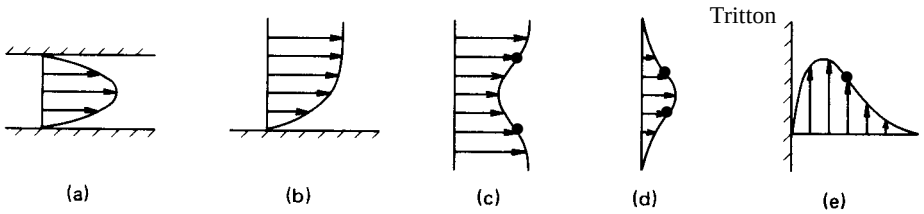

Figure 17.13 To illustrate that the velocity profiles of (a) pipe flow, (b) a boundary layer, (c) a wake, (d) a jet, and (e) a free convection boundary layer are all shear flows.

Some shear flows. Dots indicate inflection points.

where V is a characteristic variation in the velocity across the shear layer, which has a characteristic height L. Here, 'high' means at least 10^3; an ABL with a shear $V = 10$ m s^{-1} through a boundary layer of depth 1 km would have

$$\mathrm{Re} = (10 \text{ m s}^{-1})(1000 \text{ m})/ (10^{-5} \text{ m}^2 \text{ s}^{-1}) = 10^9,$$

which is plenty high!

Inviscid shear flows can be linearly unstable only if they have an *inflection point* where $d^2U/dz^2 = 0$ (Rayleigh's criterion, 1880) and are definitely unstable if the vorticity dU/dz has an extremum somewhere inside the shear layer, not on a boundary (Fjortoft's criterion, 1950). This excludes profiles such as linear shear flows or pipe flows between boundaries, but some such profiles are in fact unstable at small but nonzero viscosity, and may still break down into turbulence. The Ekman layer profile has an inflection point, so is subject to shear instability (as well as a second class of instability at moderately large Re of a few hundred).

In shear instability a layer of high vorticity rolls up into isolated vortices. A good example is the von Karman vortex street that forms the the wake behind a moving obstacle.

94. Kármán vortex street behind a circular cylinder at R=140. Water is flowing at 1.4 cm/s past a cylinder of diameter 1 cm. Integrated streaklines are shown by electrolytic precipitation of a white colloidal smoke, illuminated by a sheet of light. The vortex sheet is seen to grow in width downstream for some diameters. *Photograph by Sadatoshi Taneda*

van Dyke, p. 56

Kelvin-Helmholtz Instability

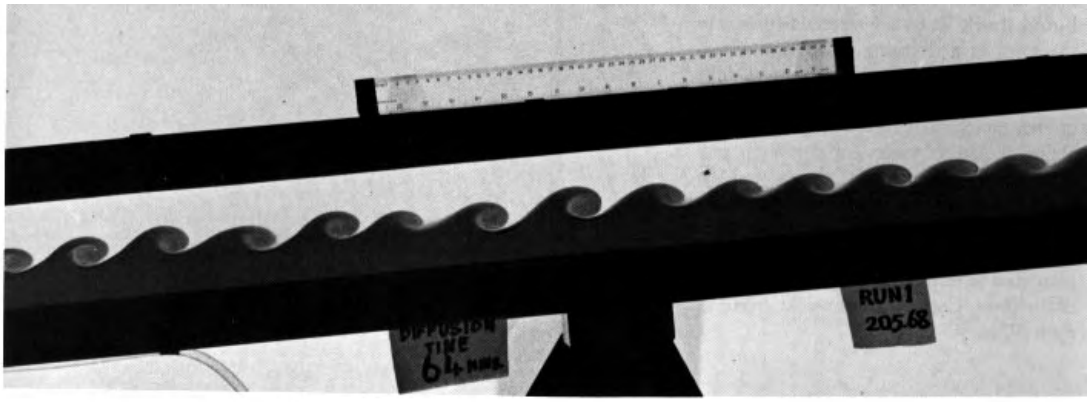

145. Kelvin-Helmholtz instability of stratified shear flow. A long rectangular tube, initially horizontal, is filled with water above colored brine. The fluids are allowed to diffuse for about an hour, and the tube then quickly tilted six degrees, setting the fluids into motion. The brine accelerates uniformly down the slope, while the water above similarly accelerates up the slope. Sinusoidal instability of the interface occurs after a few seconds, and has here grown nonlinearly into regular spiral rolls. *Thorpe 1971*

van Dyke, p. 85

For an inviscid stratified shear layer with an inflection point, instability of the shear layer may still occur if the stratification is sufficiently weak. Shear instability at the interface between two layers of different densities was first investigated by Helmholtz (1868). Miles (1960) showed that for a continuously varying system, instability cannot occur if the static stability, as measured by buoyancy frequency N is large enough that

$$\mathrm{Ri} = N^2/(dU/dz)^2 > 1/4 \text{ throughout the shear layer}$$

For lesser values of Ri, instability usually does occur. The general form of this criterion can be rationalized by considering the mixing of two parcels of fluid of volume V at different heights. In a flow relative coordinate system:

Lower parcel has height $-\delta z$, initial density $\rho - \delta\rho$, velocity $-\delta U$.

Upper parcel has height δz, initial density $\rho + \delta\rho$, velocity δU.

Here $\delta U = (dU/dz)\delta z$, and $\delta\rho = (d\rho/dz)\delta z$, where $N^2 = -(g/\rho)(d\rho/dz)$. For simplicity we consider an incompressible fluid, and assume each parcel has volume V, at heights. The total initial energy of the parcels is

$$\begin{aligned} E_i &= KE_i + PE_i \\ &= 0.5V\{(\rho - \delta\rho)(-\delta U)^2 + (\rho + \delta\rho)(\delta U)^2\} + V\{(\rho - \delta\rho)g(-\delta z) + (\rho + \delta\rho)g(\delta z)\} \\ &= V\{\rho(\delta U)^2 + 2g\delta\rho\delta z\} \end{aligned}$$

If the parcels are homogenized in density and momentum,

Lower parcel has height $-\delta z$, final density ρ, velocity 0.

Upper parcel has height δz, final density ρ, velocity 0.

The total final energy is

$$\begin{aligned} E_f &= KE_f + PE_f \\ &= 0 + V\{\rho g(-\delta z) + \rho g(\delta z)\} = 0 , \end{aligned}$$

so the change in total energy is:

$$\Delta E = E_f - E_i = -V\{\rho(\delta U)^2 + 2g\delta\rho\delta z\}$$
$$= V\rho(\delta z)^2\{-(dU/dz)^2 + 2N^2\}.$$

An energy reduction occurs if $(dU/dz)^2 > 2N^2$, i. e. if Ri < 1/2. In this case, residual energy is available to stir up eddy circulations. The reason this argument gives a less restrictive criterion for instability than an exact argument is that momentum is not fully homogenized in instabilities of a shear layer.

Convection

Thermal convection occurs if the potential density decreases with height in some layer. Classically, this instability has been studied by considering convection between two parallel plates in an incompressible fluid. The lower plate is heated to a fixed temperature that is larger than that of the upper plate. In the absence of convection, the temperature profile within the fluid would vary linearly with height due to conduction. If the plates are a distance h apart and have a temperature difference ΔT, and if the fluid has kinematic viscosity ν and thermal diffusivity κ (= 2×10^{-5} m^2 s^{-1} for air), then convective instability occurs when the Rayleigh number

$$Ra = h^3\Delta B/\nu\kappa > 1700$$

Here ΔB is the buoyancy change $-g\Delta\rho/\rho$ associated with a temperature increase of ΔT at a given pressure; for air and other ideal gasses, $\Delta B = g\Delta T / T$. The instability is a circulation with cells with comparable width to height, a property of thermal convection observed even when Ra is much larger. Rolls and hexagonal patterns are equally unstable.

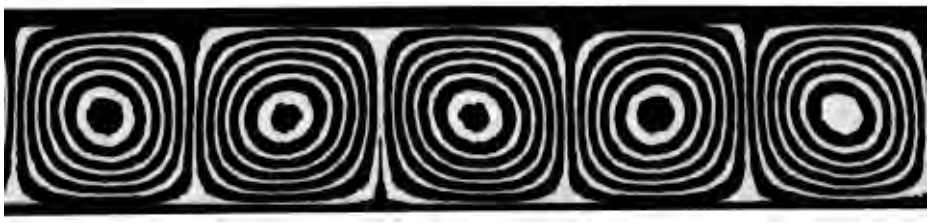

Slightly unstable convection in silicone oil van Dyke p. 82

In the presence of a mean shear, the fastest growing convective instabilities are rolls aligned along the shear vector, as seen in the cloud streets below.

Fig. 7.2. Convective clouds in an unstable layer, aligned in 'streets' along the direction of shear. (Compare with fig. 4.14 pl. x, which shows clouds formed by a shear instability and aligned across the flow. The form of 'billow' clouds can vary widely according to the relative importance of shear and convection.) (Photograph: R. S. Scorer.) Turner

For ABL convection, the surface skin temperature can be a few kelvins warmer than the typical boundary layer air temperature. Even with a small $\Delta T = 1$ K, we can estimate $\Delta B = (10\ \text{m s}^{-2})(1\ \text{K})/(300\ \text{K}) = 0.03\ \text{m s}^{-2}$, $h = 1000$ m, and

$$\text{Ra} = (0.03\ \text{m s}^{-2})(1000\ \text{m})^3 /(1.4\times10^{-5}\ \text{m}^2\ \text{s}^{-1})(2\times10^{-5}\ \text{m}^2\ \text{s}^{-1}) = 10^{17}\ !$$

so the atmosphere is very far indeed from the instability threshold due to the large lengthscales and small viscosities.

Transition to turbulence

Each of these instabilities initially has a simple, regular circulation pattern. However, if the fluid is sufficiently inviscid, three-dimensional secondary instabilities grow on the initial circulation, and the flow becomes complex, irregular in time, and develops regions in which there are motions on a variety of scales. This is a transition into turbulent motion. We don't generally see this transition in the ABL, since the ideal basic state on which the initial instability grows is rarely realized.

102. Instability of an axisymmetric jet. A laminar stream of air flows from a circular tube at Reynolds number 10,000 and is made visible by a smoke wire. The edge of the jet develops axisymmetric oscillations, rolls up into vortex rings, and then abruptly becomes turbulent. *Photograph by Robert Drubka and Hassan Nagib*

Lecture 2. Turbulent Flow

166. Turbulent water jet. Laser-induced fluorescence shows the concentration of jet fluid in the plane of symmetry of an axisymmetric jet of water directed downward into water. The Reynolds number is approximately 2300. The spatial resolution is adequate to resolve the Kolmogorov scale in the downstream half of the photograph. *Dimotakis, Lye & Papantoniou 1981*

Note the diverse scales of eddy motion and self-similar appearance at different lengthscales of the turbulence in this water jet. Only eddies of size $0.01L$ or smaller are subject to substantial viscous dissipation.

Description of Turbulence

Turbulence is characterized by disordered, eddying fluid motions over a wide range of length-scales. While turbulent flows still obey the deterministic equations of fluid motion, a small initial perturbation to a turbulent flow rapidly grows to affect the entire flow (loss of predictability), even if the external boundary conditions such as pressure gradients or surface fluxes are unchanged. We can imagine an infinite family or *ensemble* of turbulent flows all forced by the same boundary conditions, but starting from a random set of initial flows. One way to create such an ensemble is by adding random small perturbations to the same initial flow, then looking at the resulting flows at a much later time when they have become decorrelated with each other.

Turbulent flows are best characterized statistically through **ensemble averaging**, i. e. averaging some quantity of interest across the entire ensemble of flows. By definition, we cannot actually measure an ensemble average, but turbulent flows vary randomly in time and (along directions of symmetry) in space, so a sufficiently long time or space average is usually a good approximation to the ensemble average. Any quantity a (which may depend on location or time) can be partitioned

$$a = \bar{a} + a' ,$$

where $\bar{a}$ is the **ensemble mean** of a, and a' is the fluctuating part or perturbation of a. The ensemble mean of a' is zero by definition; a' can be characterized by a probability distribution whose spread is characterized by the **variance** $\overline{a'a'}$. One commonly referred to measure of this type is the turbulent kinetic energy (TKE) per unit mass,

$$\text{TKE} = \frac{1}{2}(\overline{u'u'} + \overline{v'v'} + \overline{w'w'})$$

This is proportional to the variance of the magnitude of the velocity perturbation:

$$\text{TKE} = \frac{1}{2}\overline{q'q'} \ , \quad q' = (u'^2 + v'^2 + w'^2)^{1/2}.$$

We may also be interested in **covariances** between two quantities a and b. These might be the same field measured at different locations or times (i. e., the spatial or temporal autocorrelation), or different fields measured at the same place and time (e. g. the upward eddy heat flux is proportional to the covariance $\overline{w'T'}$ between vertical velocity w and temperature T). Variances and covariances are called **second-order moments** of the turbulent flow. These take a longer set of measurements to determine reliably than ensemble means.

The temporal autocorrelation of a perturbation quantity a' measured at a fixed position,

$$R(T) = \frac{\overline{a'(t)a'(t+T)}}{\overline{a'(t)a'(t)}}$$

can be used to define an **integral time scale**

$$\tau_a = \int_0^\infty R(T)\,dT$$

which characterizes the timescale over which perturbations of a are correlated. One may similarly

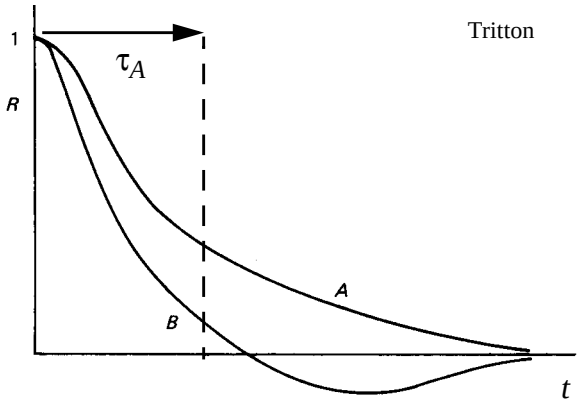

Figure 20.5 Typical correlation curves.

define an integral length scale.

One commonly referred-to statistic for turbulence in which buoyancy forces are important involves third-order moments. The vertical velocity **skewness** is defined

$$S = \frac{\overline{w'w'w'}}{\overline{w'w'}^{3/2}}$$

The skewness is positive where perturbation updrafts tend to be more intense and narrower than perturbation downdrafts, e. g. in cumulus convection, and is negative where the downdrafts are more intense and narrower, e. g. at the top of a stratocumulus cloud. Skewness larger than 1 indicates quite noticeable asymmetry between perturbation up and downdrafts.

Fourier spectra in space or time of perturbations are commonly used to help characterize the distribution of the fluctuations over different length and time scales. For example, given a long time series of a quantity $a(t)$, we can take the Fourier transform of its autocovariance to get its temporal **power spectrum**.vs. frequency ω,

$$\tilde{S}_a(\omega) = \frac{1}{2\pi}\int_{-\infty}^{\infty} \overline{a'(t)a'(t+T)}\exp(-i\omega T)dT \quad \text{(this is real and positive for all } \omega)$$

Given the power spectrum, one can recover the autocovariance by an inverse Fourier transform, and in particular, the variance is the integral of the power spectrum over all frequencies,

$$\overline{a'(t)a'(t)} = \int_{-\infty}^{\infty} \tilde{S}_a(\omega)d\omega \ ,$$

so we can think of the power spectrum as a partitioning of the variance of a between frequencies.

For spatially **homogeneous** turbulence one can do a 3D Fourier transform of the spatial autocovariance function to obtain the spatial power spectrum vs. wavevector **k**,

$$\hat{S}_a(\mathbf{k}) = \frac{1}{(2\pi)^3}\int_{-\infty}^{\infty} \overline{a'(\mathbf{r})a'(\mathbf{r}+\mathbf{R})}\exp(-i(\mathbf{k}\cdot\mathbf{R}))d\mathbf{k} \ ;$$

again the variance a is the integral of the power spectrum over all wavenumbers,

$$\overline{a'(\mathbf{r})a'(\mathbf{r})} = \int_{-\infty}^{\infty} \hat{S}_a(\mathbf{k})d\mathbf{k}$$

If the turbulence is also **isotropic**, i. e. looks the same from all orientations, then the power spectrum depends only on the magnitude k of the wavenumber, and we can partition the variance into different wavenumber bands:

$$\overline{a'(\mathbf{r})a'(\mathbf{r})} = \int_0^\infty \hat{S}_a(k) 4\pi k^2 dk .$$

In particular, for homogeneous isotropic turbulence we can partition TKE into contributions from all wavenumbers; this is called the **energy spectrum** $E(k)$.

$$\text{TKE} = \frac{1}{2}\overline{q'(\mathbf{r})q'(\mathbf{r})} = \int_0^\infty E(k)dk$$

Roughly speaking, the energy spectrum at a particular wavenumber k can be visualized as being due to eddies whose characteristic size (diameter) is $2\pi/k$.

Turbulent Energy Cascade

Ultimately, boundary layer turbulence is due to continuous forcing of the mean flow toward a state in which shear or convective instabilities grow. These instabilities typically feed energy mostly into eddies whose characteristic size is comparable to the boundary layer depth. When these eddies become turbulent, considerable variability is also seen on much smaller scales. This is often described as an **energy cascade** from larger to smaller scales through the interaction of eddies. It is called a cascade because eddies are deformed and folded most efficiently by other eddies of comparable scales, and this squeezing and stretching transfers energy between nearby lengthscales. Thus the large eddies feed energy into smaller ones, and so on until the eddies become so small as to be viscously dissipated. There is typically a range of eddy scales larger than this at which buoyancy or shear of the mean flow are insignificant to the eddy statistics compared to the effects of other turbulent eddies; in this **inertial subrange** of scales the turbulent motions are roughly homogeneous, isotropic, and inviscid, and if fact from a photograph one could not tell at what lengthscale one is looking, i. e. the turbulence is self-similar.

Dimensional arguments have always played a central role in our understanding of turbulence due to the complexity and self-similarity of turbulent flow. Kolmogorov (1941) postulated that for large Reynolds number, the statistical properties of turbulence above the viscous dissipation scale are independent of viscosity and depend only on the rate at which energy produced at the largest scale L is cascaded down to smaller eddies and ultimately dissipated by viscosity. This is measured

Garratt

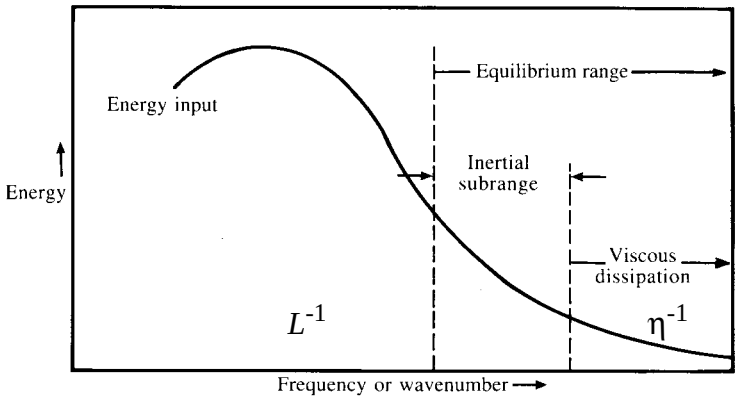

Fig. 2.1 Schematic representation of the energy spectrum of turbulence.

by the average energy dissipation rate ε per unit mass (units of energy per unit mass per unit time, or $m^2\ s^{-3}$). If the largest scale eddies have characteristic eddy velocity V, dimensional analysis implies

$$\varepsilon \propto V^3/L$$

and the dissipation timescale is the eddy turnover timescale L/V (which is typically O(1000 m/1 m s^{-1}) = 1000 s in the ABL.) This means that if its large-scale energy source is cut off, turbulence decays within a few turnover times. The viscous dissipation lengthscale or **Kolmogorov scale** η depends on ε ($m^2 s^{-3}$) and ν ($m^2 s^{-1}$) , so dimensionally

$$\eta = (\nu^3/\varepsilon)^{1/4}\ (\approx 1 \text{ mm for the ABL}) = Re^{-3/4} L$$

Kolmogorov argued that the energy spectrum $E(k)$ within the inertial subrange can depend only on the lengthscale, measured by wavenumber k, and ε. Noting that $E(k)$ has units of TKE/wavenumber = $m^2 s^{-2}/m^{-1} = m^3 s^{-2}$, dimensional analysis implies the famous **-5/3 power law**,

$$E(k) \propto \varepsilon^{-2/3} k^{-5/3}, \qquad L^{-1} << k << \eta^{-1}$$

Similarly, the spatial power spectra of velocity components and scalars a also follow $\hat{S}_a(k) \propto k^{-5/3}$ in the inertial range.

The spatial power spectrum can be measured in one direction by a sensor moving with respect to the boundary layer at a speed U comparable to or larger than V, i. e. if the wind is blowing different turbulent eddies past a sensor on the ground, or if we take measurements from an aircraft.We must invoke **Taylor's ('frozen turbulence') hypothesis** that the statistics of the turbulent field are similar to what we would measure if the turbulent field remained unchanged and just advected by-with the mean speed U. In general, empirically this appears to be a good assumption. Temporal power spectra $\tilde{S}_a(\omega)$ gathered in this way can be converted to spatial power spectral by substituting $\omega = Uk$,

$$\hat{S}_a(k) = U\tilde{S}_a(Uk) \quad \text{for turbulence moving by with mean speed } U$$

Thus, we expect an $\omega^{-5/3}$ temporal power spectrum for scalars and velocity components in the inertial subrange.

The figures below show measurements from a tethered balloon stationed in a convecting cloud-topped boundary layer at 85% of the inversion height. The mean wind of $U = 7$ m s^{-1} is considerable larger than the characteristic large-eddy velocity of $V = 1$ m s^{-1}, so Taylor's hypothesis is safe. The time series shows up and downdrafts associated with large eddies with width and height comparable to the BL depth of 1 km, with turbulent fluctuations associated with smaller eddies. The corresponding temporal power spectrum (triangles) is plotted as $\omega\tilde{S}_a(\omega)$, as expected, this has a $\omega^{-2/3}$ dependence in the inertial range, and decays at low frequencies that correspond to lengthscales larger than L..

The second spectrum (circles) is in the entrainment zone, which is in a very sharp and strong inversion (stable layer) at the BL top. Here, large scale, strong, vertical motions are suppressed, and the turbulence is highly anisotropic at these scales, but at small scales (a few meters or less) an inertial range is still observed.

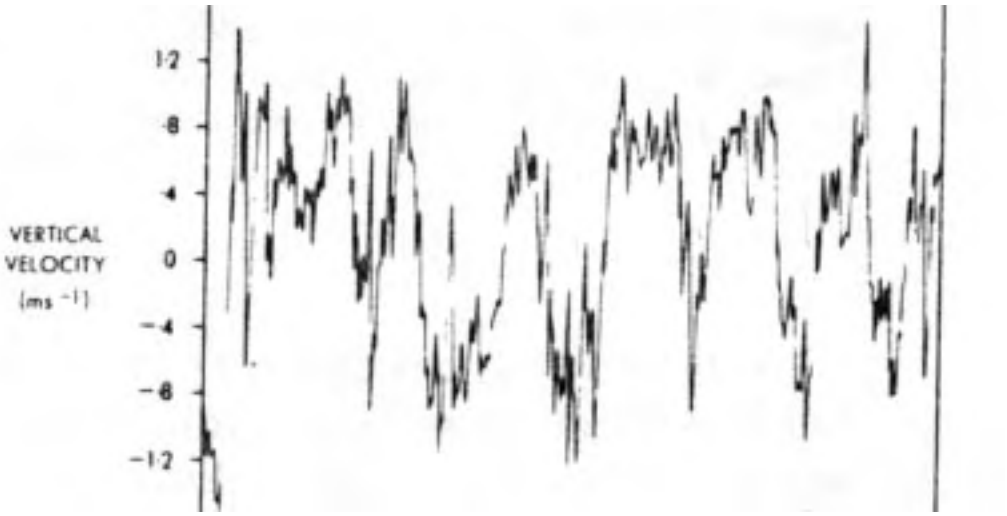

Vertical velocity trace over a 10 minute period, corresponding to an advection distance of 4200 m, in a 1 km deep convecting boundary layer

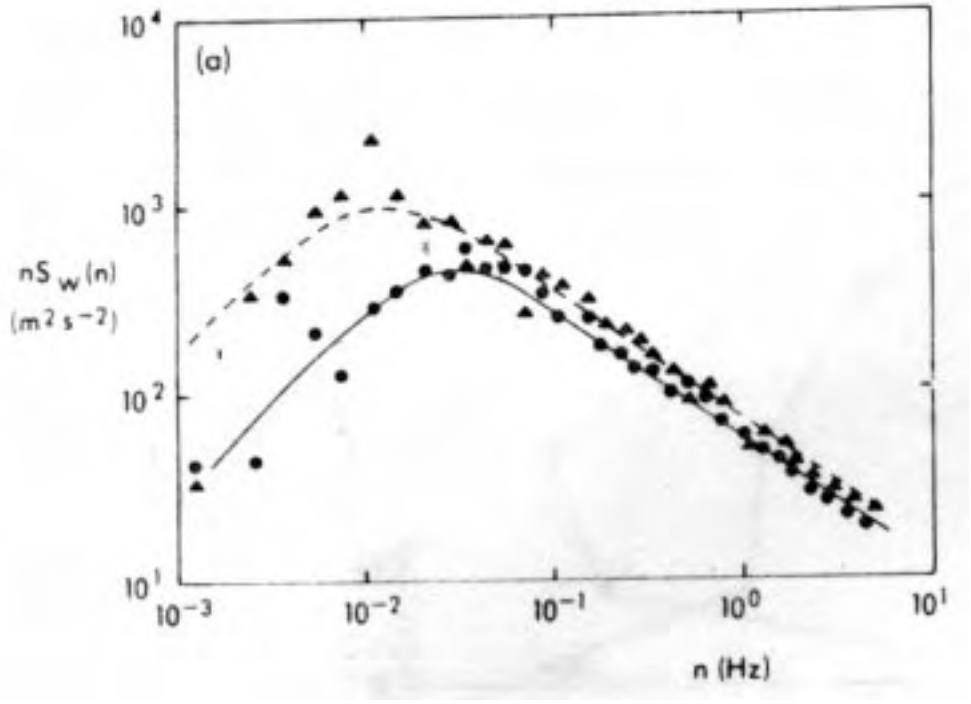

Temporal ower spectrum of vertical velocity. Triangles correspond to height shown above, and circles are in the entrainment zone at BL top.

Interestingly, 2D ‘turbulence’ doesn’t produce an energy cascade to small scales; instead, in 2D (as simulated on the computer) energy tends to be transferred to the largest scale motions permitted by the boundaries, and broad regions of smoothly varying flow appear, interrupted by shear lines and intense long-lived.vortices.

Lecture 3. Turbulent fluxes and TKE budgets (Garratt, Ch 2)

The ABL, though turbulent, is not homogeneous, and a critical role of turbulence is transport and mixing of air properties, especially in the vertical. This process is quantified using ensemble averaging (often called Reynolds averaging) of the hydrodynamic equations.

Boussinesq Equations (G 2.2)

For simplicity, we will use the Boussinesq approximation to the Navier-Stokes equations to describe boundary-layer flows. This is quite accurate for the ABL (and ocean BLs as well), since:

1. The ABL depth O(1 km) is much less than the density scale height O(10 km).
2. Typical fluid velocities are O(1-10 m s^{-1}), much less than the sound speed.

The Boussinesq equations of motion are:

$$\frac{D\mathbf{u}}{Dt} + f\mathbf{k}\times\mathbf{u} = -\frac{\nabla p'}{\rho_0} + b\mathbf{k} + [\nu\nabla^2\mathbf{u}], \text{ where buoyancy } b = g\theta_v'/\theta_0$$

$$\nabla\cdot\mathbf{u} = 0$$

$$\frac{D\theta}{Dt} = S_\theta + [\kappa\nabla^2\theta], \quad S_\theta \approx -\frac{1}{\rho_0 C_p}\frac{\partial R_N}{\partial z} \text{ in the absence of clouds}$$

$$\frac{Dq}{Dt} = S_q + [\kappa_q\nabla^2 q], \quad S_q = 0 \text{ in the absence of precipitation}$$

Here p' is a pressure perturbation, θ is potential temperature, $q = q_v + q_l$ is mixing ratio (including water vapor q_v and liquid water q_l if present), and $\theta_v = \theta(1 + .608q_v - q_l)$ is virtual potential temperature including liquid water loading. S denotes source/sink terms, and ρ_0 and θ_0 are characteristic ABL density and potential temperature. κ and κ_q are the diffusivities of heat and water vapor. The most important source term for θ is divergence of the net radiative flux R_N (usually treated as horizontally uniform on the scale of the boundary layer, though this needn't be exactly true, especially when clouds are present). For noprecipitating BLs, $S_q = 0$.. For cloud-topped boundary layers, condensation, precipitation and evaporation can also be important.

Using mass continuity, the substantial derivative of any quantity a can be written in flux form

$$Da/Dt = \partial a/\partial t + \nabla\cdot(\mathbf{u}a).$$

Ensemble Averaging (G 2.3)

The ensemble average of Da/Dt is:

$$\overline{\frac{Da}{Dt}} = \overline{\frac{\partial a}{\partial t}} + \nabla\cdot\overline{\mathbf{u}a}$$

$$= \frac{\partial}{\partial t}\bar{a} + \frac{\partial}{\partial t}\overline{a'} + \frac{\partial}{\partial x}\overline{(\bar{u}+u')(\bar{a}+a')} + \frac{\partial}{\partial y}\overline{(\bar{v}+v')(\bar{a}+a')} + \frac{\partial}{\partial z}\overline{(\bar{w}+w')(\bar{a}+a')}$$

$$= \frac{\partial}{\partial t}\bar{a} + \nabla\cdot\bar{\mathbf{u}}\bar{a} + \frac{\partial}{\partial x}\overline{u'a'} + \frac{\partial}{\partial y}\overline{v'a'} + \frac{\partial}{\partial z}\overline{w'a'}$$

The three **eddy correlation** terms at the end of the equation express the net effect of the turbulence. Consider a BL of characteristic depth H over a nearly horizontally homogeneous surface. The most energetic turbulent eddies in the boundary layer have horizontal and vertical lengthscale H and (by mass continuity) the same scale U for turbulent velocity perturbations in both the horizontal and vertical. The boundary layer structure, and hence the eddy correlations, will vary horizontally on characteristic scales $L_s >> H$ due to the impacf on the BL of mesoscale and synoptic-scale variability in the free troposphere. If we let {} denote 'the scale of', and assume $\{a'\} = A$, we see that **the vertical flux divergence is dominant**:

$$\left\{\frac{\partial}{\partial x}\overline{u'a'}\right\} = \frac{UA}{L_s} \ll \left\{\frac{\partial}{\partial z}\overline{w'a'}\right\} = \frac{UA}{H}$$

Thus (noting also that $\nabla \cdot \bar{\mathbf{u}} = 0$ to undo the flux form of the advection of the mean),

$$\overline{\frac{Da}{Dt}} \approx \frac{\partial}{\partial t}\bar{a} + \bar{\mathbf{u}} \cdot \nabla \bar{a} + \frac{\partial}{\partial z}\overline{w'a'}$$

If we apply this to the ensemble-averaged heat equation, and throw out horizontal derivatives of θ in the diffusion term using the same lengthscale argument $L_s >> H$ as above, we find

$$\frac{\partial}{\partial t}\bar{\theta} + \bar{\mathbf{u}} \cdot \nabla \bar{\theta} = -\frac{\partial}{\partial z}(\overline{w'\theta'}) + \overline{S_\theta} + \left[\kappa \frac{\partial^2}{\partial z^2}\bar{\theta}\right]$$

Thus, the effect of turbulence on $\bar{\theta}$ is felt through the convergence of the vertical eddy correlation, or **turbulent flux** of θ. The turbulent **sensible and latent heat fluxes** are the turbulent fluxes of θ and q in energy units of W m^{-2}:

Turbulent sensible heat flux = $\rho_0 C_p \overline{w'\theta'}$

Turbulent latent heat flux = $\rho_0 L \overline{w'q'}$

Except in the interfacial layer within mm of the surface, the diffusion term is negligible , so we've written it in square brackets.

If geostrophic wind $\mathbf{u}_g$ is defined in the standard way, the ensemble-averaged momentum equations are

$$\frac{\partial \bar{u}}{\partial t} + \bar{\mathbf{u}} \cdot \nabla \bar{u} = f(\bar{v} - v_g) - \frac{\partial}{\partial z}(\overline{u'w'})$$

$$\frac{\partial \bar{v}}{\partial t} + \bar{\mathbf{u}} \cdot \nabla \bar{v} = -f(\bar{u} - u_g) - \frac{\partial}{\partial z}(\overline{v'w'})$$

Often, but not always, the tendency and advection terms are much smaller than the two terms on the right hand side, and there is an approximate three-way force balance (see figure below) between momentum flux convergence, Coriolis force and pressure gradient force in the ABL such that the mean wind has a component down the pressure gradient. The **cross-isobar flow angle** α is the angle between the actual surface wind and the geostrophic wind.

If the mean profiles of actual and geostrophic velocity can be accurately measured, the momen-

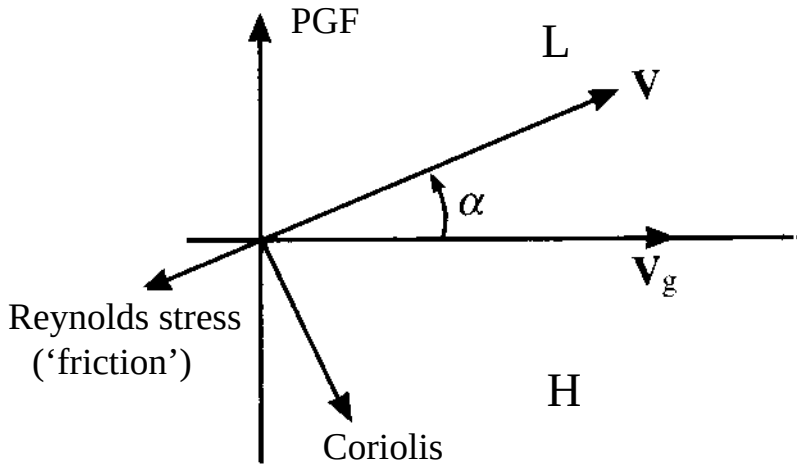

Surface layer force balance in a steady state BL ($f > 0$). Above the surface layer, the force balance is similar but the Reynolds stress need not be along **-V**.

tum flux convergence can be calculated as a residual in the above equations, and vertically integrated to deduce momentum flux. This technique was commonly applied early in this century, before fast-response, high data rate measurements of turbulent velocity components were perfected. It was not very accurate, because small measurement errors in either **u** or $\mathbf{u}_g$ can lead to large relative errors in momentum flux.

In most BLs, the vertical fluxes of heat, moisture and momentum are primarily carried by large eddies with lengthscale comparable to the boundary layer depth, except near the surface where smaller eddies become important. The figure below shows the **cospectrum** of w' and T', which is the Fourier transform of $w'T'$, from tethered balloon measurements at two heights in the cloud-topped boundary layer we plotted in the previous lecture. The cospectrum is positive, i. e. positive correlation between w' and T', at all frequencies, typical of a convective boundary layer. Most of the covariance between w' and T' is at the same low frequencies $n = \omega/2\pi \sim 10^{-2}$ Hz that had the maximum energy. Since the BL is blowing by the tethered balloon at the mean wind speed $\overline{U} = 7$ m s^{-1}, this frequency corresponds to large eddies of wavelength $\lambda = \overline{U}/n = 700$ m, which is comparable to the BL depth of 1 km.

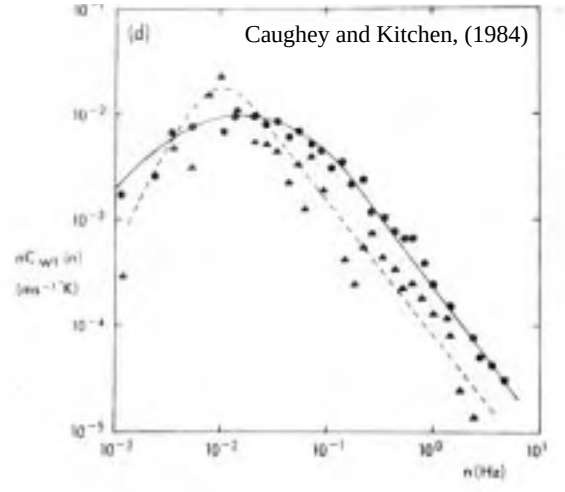

Cospectrum of w' and T' at cloud base (triangles), top (circles) in convective BL.

Turbulent Energy Equation (G 2.5,6)

To form an equation for TKE $\bar{e} = \overline{\mathbf{u}' \cdot \mathbf{u}'}/2$, we dot $\mathbf{u}$ into the momentum equation, and take the ensemble average. After considerable manipulation, we find that for the nearly horizontally homogeneous BL ($H << L_s$),

$$\frac{\partial}{\partial t}\bar{e} + \bar{\mathbf{u}} \cdot \nabla \bar{e} = S + B + T + D$$

where

$$S = -\overline{u'w'}\frac{\partial \bar{u}}{\partial z} - \overline{v'w'}\frac{\partial \bar{v}}{\partial z} \quad \text{(shear production)}$$

$$B = \overline{w'b'} \quad \text{(buoyancy flux)}$$

$$T = -\frac{\partial}{\partial z}\left(\overline{w'e'} + \frac{1}{\rho_0}\overline{w'p'}\right) \quad \text{(transport and pressure work)}$$

$$D = -\nu\overline{|\nabla \times \mathbf{u}|^2} \quad \text{(dissipation, always negative, -ε in Garratt)}$$

Shear production of TKE occurs when the momentum flux is downgradient, i. e. has a component opposite (or 'down') the mean vertical shear. To do this, the eddies must tilt into the shear. Kinetic energy of the mean flow is transferred into TKE. Buoyancy production of TKE occurs where relatively buoyant air is moving upward and less buoyant air is moving downward. Gravitational potential energy of the mean state is converted to TKE. Both *S* and *B* can be negative at some or all levels in the BL, but together they are the main source of TKE, so the vertical integral of *S* + *B* over the BL is always positiveThe transport term mainly fluxes TKE between different levels, but a small fraction of TKE can be lost to upward-propagating internal gravity waves excited by turbulence perturbing the BL top. The dissipation term is the primary sink of TKE, and formally is related to enstrophy. In turbulent flows, the enstrophy is dominated by the *smallest* (dissipation) scales, so *D* can be considerable despite the smallness of ν.

Usually, the left hand side (the 'storage' term) is smaller than the dominant terms on the right hand side. The figure on the next page shows typical profiles of these terms for a daytime convectively driven boundary layer and a nighttime shear-driven boundary layer. In the convective boundary layer, transport is considerable. Its main effect is to homogenizing TKE in the vertical . With vertically fairly uniform TKE, dissipation is also uniform, except near the ground where it is enhanced by the surface drag . Shear production is important only near the ground (and sometimes at the boundary layer top). In the shear-driven boundary layer, transport and buoyancy fluxes are small everywhere, and there is an approximate balance between shear production and dissipation.

The **flux Richardson number**

$$\mathrm{Ri}_f = -B/S$$

characterizes whether the flow is stable ($\mathrm{Ri}_f > 0$), neutral ($\mathrm{Ri}_f \approx 0$), or unstable ($\mathrm{Ri}_f < 0$).

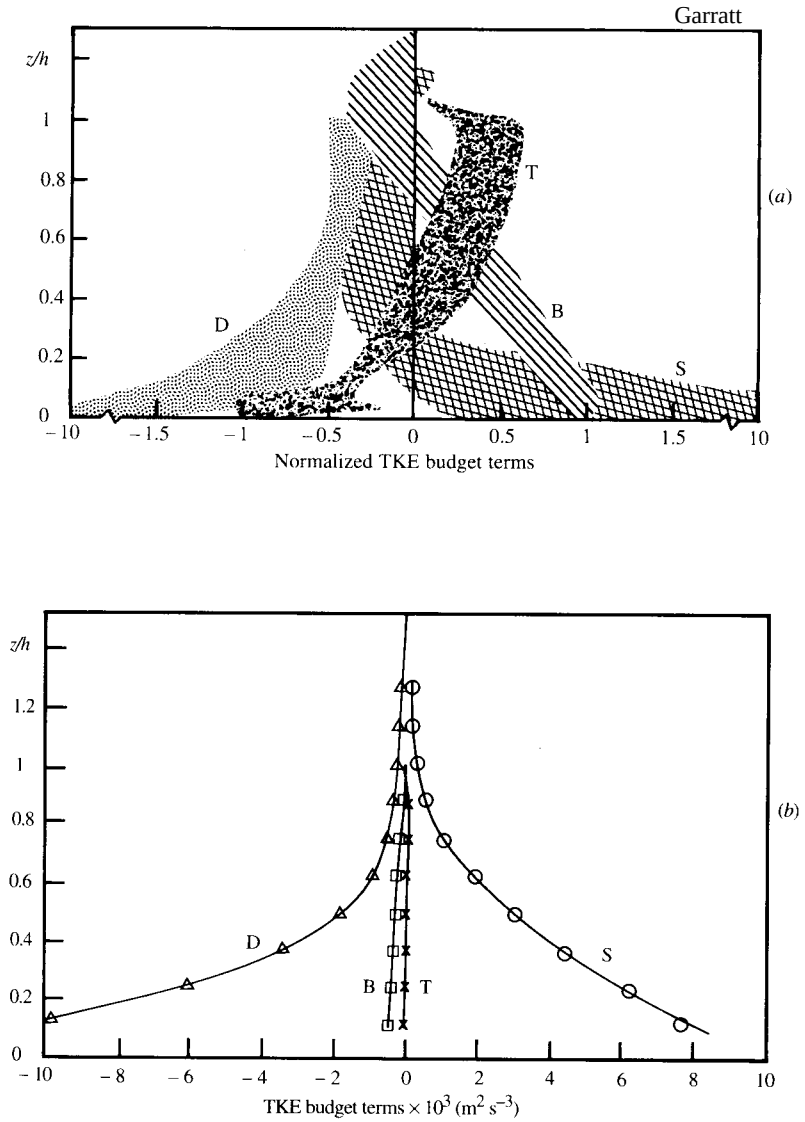

Fig. 2.4 Terms in the TKE equation (2.74b) as a function of height, normalized in the case of the clear daytime ABL (*a*) through division by w_*^3/h; actual terms are shown in (*b*) for the clear night-time ABL. Profiles in (*a*) are based on observations and model simulations as described in Stull (1988; Figure 5.4), and in (*b*) are from Lenschow *et al.* (1988) based on one aircraft flight. In both, B is the buoyancy term, D is dissipation, S is shear generation and T is the transport term. Reprinted by permission of Kluwer Academic Publishers.

Lecture 4. Boundary Layer Turbulence and Mean Wind Profiles

Turbulence Closure Models (G 2.4)

The equations for ensemble averaged quantities involve the divergence of the eddy correlations, which arise from averaging the nonlinear advection terms. Similarly, prognostic equations for the ensemble averaged second-order correlations include averages of triple correlations, etc...so this approach does not lead to a closed set of equations. In a **turbulence closure** model (TCM), higher-order correlations are parameterized in terms of lower-order correlations to close the system. In a first-order TCM, all second-order correlations are parameterized in terms of the mean fields. In a second-order TCM, 1st and second order moments are prognosed, but third-order correlations are parameterized in terms of them. TCMs of up through third order have been used. Third order TCMs can do a fairly realistic job of predicting the profiles of mean fields and even second-order moments, but are quite complicated and computationally intensive.

First-order turbulence closure, mixing length theory, and eddy diffusivity

For now, we will just introduce first-order turbulence closure, which is the most common parameterization of turbulent mixing currently used in large-scale numerical models such as GCMs. The usual approach is inspired by **mixing length theory** (Prandtl 1925). We idealize eddies as taking random fluid parcels from some level, and advecting them up or down over some characteristic height or *mixing length* δz at some characteristic speed V, where the fluid parcel gets homogenized with the other air at that level. Except near the surface, the transport is primarily by eddies whose scale is the boundary layer depth, so we think of V as the large-eddy velocity and δz as proportional to the boundary layer height scale H. Near the surface, a different scaling applies, which we discuss later. At any location, half the time there is an updraft with $w_u' = V$ carrying fluid upward from an average height $z - \delta z/2$, and the other half of the time there is a downdraft with $w_d' = -V$ carrying fluid downward from an average height $z + \delta z/2$. Consider the corresponding vertical flux of some advected quantity a. In updrafts,

$$a_u' = \bar{a}(z - \delta z/2) - \bar{a}(z)$$

If we assume that $\bar{a}$ varies roughly linearly between $z - \delta z/2$ and z, then

$$a_u' \approx - \frac{\delta z}{2}\frac{d\bar{a}}{dz}$$

Similarly, in downdrafts,

$$a_d' = \bar{a}(z + \delta z/2) - \bar{a}(z) \approx \frac{\delta z}{2}\frac{d\bar{a}}{dz}$$

Hence, taking the ensemble average,

$$\overline{w'a'} = \frac{1}{2}(w_u' a_u' + w_d' a_d') \approx -K_a \frac{d\bar{a}}{dz} \ , \text{ where } K_a = V\delta z/2$$

Thus the eddy flux of a is always down the mean gradient, and acts just like diffusion with an **eddy diffusivity** K_a. For typical ABL scales $V = 1$ m s^{-1}, $\delta z = 1$ km, and mixing length theory would predict $K_a = 500$ m^{2}s^{-1}. Most first order turbulence closure models assume that turbulence acts as an eddy diffusivity, and try to relate V and δz to the profiles of velocity and static stability; more on how this is done later when we talk about parameterization.

Observing the BL

The turbulent nature of BL flow presents special challenges for observations and modeling. On the other hand, its nearness to the surface makes surface-based observing systems particularly useful. Chapter 10 of Stull's book (handout) is an excellent summary of sensors (and the principles by which they work), types of measurement and analysis methods for ABL observations. It also has a list of major BL field experiments through early 1987 and describes numerical modelling of boundary layer turbulence. Fast response sensors capable of in-situ measurements of turbulent perturbations in velocity components, temperature, pressure, humidity and some trace gases (such as CO_2) from different platforms, e.g. an airplane, balloon, mast, or surface site are now widely available, and can be used to calculate vertical turbulent fluxes and moments. Due to the sensitivity of the instruments and their high data rate, these measurements are restricted to dedicated field experiments. Remote sensors measure waves generated or modified by the atmosphere at locations distant from the sensor. Active remote sensorsgenerate sound (sodar), light (lidar), or other EM waves (e. g. radar). Passive remote sensors, rely on electromagnetic waves generated by the earth (infrared, microwave), the atmosphere (infrared), or the sun (visible). Remote sensors can often scan over a large volume and are invaluable in characterizing aspects of the vertical structure of the BL, but typically provide poor time and space resolution. However, Doppler lidar (in clear air with some scatterers) and mm-wave radar (in cloud) have proved capable of resolving larger turbulent eddies and characterizing some of the turbulent statistics of the flow, and are particularly useful for characterizing the structure of the entrainment zone at the top of the boundary layer.

Large-eddy simulation

Numerical modeling, in particular **large-eddy simulation (LES)** has also become a formidable tool for understanding BL turbulence. A two or preferably three-dimensional numerical domain somewhat deeper than the anticipated boundary layer depth H, and at least 2-3H wide, is covered by a grid of points. A typical domain size for an ABL simulation might be 5×5×2 km The grid spacing must be small enough to accurately resolve the larger eddies which are most energetic and transport most of the fluxes. Grid spacings of 100 m in the horizontal and 50 m in the vertical are adequate for a convective boundary layer without a strong capping inversion. Such a simulation might run nearly in real time on a fast workstation. Higher resolution (10-20 m) is required near strong inversions and for stable, shear-driven BLs, putting such simulations at the edge of what can currently be done on a workstation. The Boussinesq equations or some other approximation to the dynamical equations are discretized on the grid. A **subgridscale** model is used to parameterize the effects of unresolved eddies on the resolved scale. There is no consensus on the ideal subgrid-scale model. Luckily, as long as the grid-spacing is fine enough, LES simulations have been found to be relatively insensitive to this. One can understand this as a consequence of the turbulent energy cascade, in which energy fluxes down to small scales in a manner relatively independent of the details of the viscous drain. In an LES, the energy cascade must be terminated at the grid scale, but as long as the grid-scale is in the inertial range and the grid-scale eddies are efficiently damped, this should not affect the statistics of the large eddies.

The simulation is started from an idealized, usually nonturbulent initial profile,and forced with realistic surface fluxes, geostrophic winds, etc. Small random perturbations are added to some field such as temperature; these seed shear or convective instability which develops into a quasi-steady turbulent flow, typically within an hour or two of simulated time for ABL simulations. The simulation is run for a few more hours and flow statistics and structures from the quasi-steady period are analyzed. For cloud-topped boundary layers, radiative fluxes and a model of cloud mi-

crophysics are also part of the LES.

Intercomparisons between different LES codes and comparisons with data show that for a convective boundary layer without a strong capping inversion, the simulation statistics are largely independent of the LES code used, building confidence in the approach. For cloud-topped boundary layers, different codes agree on the vertical structure of the large eddies within the BL, but predict considerably different rates of entrainment or free-tropospheric air for the same forcing. This is not surprising, as most current LES models are run with 25-50 m resolution at the inversion, which is often insufficient. As soon as other physical parameterizations, such as cloud microphysics, radiation, or land-surface models are coupled into the LES, the results are only as good as the weakest parameterization! Thus, LES models of most realistic BLs are illuminating, but are no substitute for observations.

Laboratory Experiments

Turbulence is important in many contexts outside atmospheric science, such as aerodynamics, hydraulics, oceanography, astrophysics, etc. Most of our fundamental understanding of turbulence derives from laboratory experiments with these contexts in mind. Convection has been studied, mainly in liquids, in tanks a few cm to a few m in size. Shear flows have been studied in water tunnels or rotating tanks. Salt can be used to produce stratification. Turbulence can be created by stirring or passing moving fluid through a grid. Many sophisticated visualization techniques, using dye, in-situ sensors, laser velocimetry, etc. are used. Many simple models of atmospheric turbulence are 'tuned' based on laboratory results.

Typical boundary layer profiles

Mixing length theory predicts that vigorous turbulence should strongly diffuse vertical gradients of mean quantities in the BL, resulting in a 'well-mixed' BL with only slight residual vertical gradients. How well does turbulence mix up observed boundary layers? For clear unstable (convective) BLs, mixed layer structure is observed in $\overline{\theta}$, usually in $\overline{q}$, and often in $\overline{u}$, $\overline{v}$ (with slight veering of the wind with height.

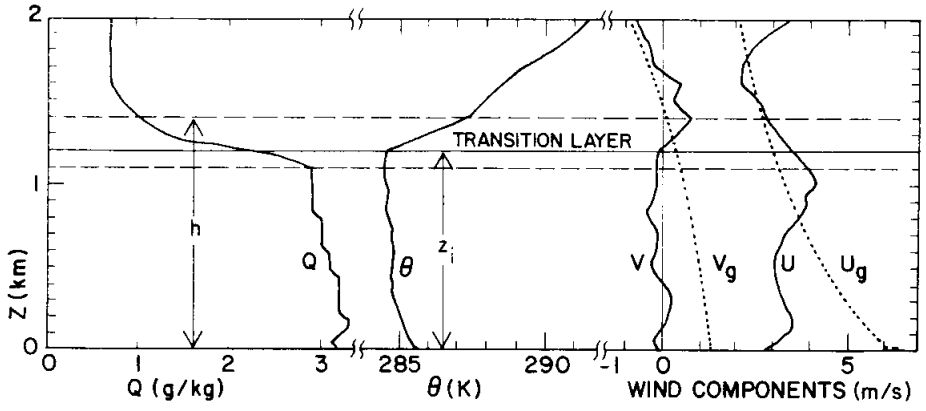

Arya

Fig. 6.5 Measured wind, potential temperature, and specific humidity profiles in the PBL under convective conditions on day 33 of the Wangara Experiment. [From Deardorff (1978).]

Typical mixed layer structure of a convective boundary layer (visible even in *u*, *v*).

Arya

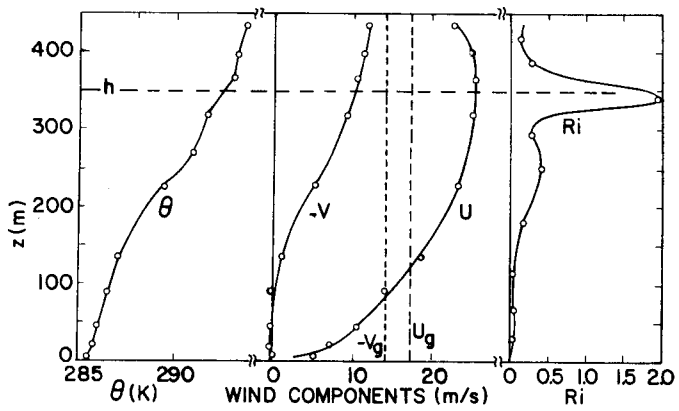

Fig. 6.7 Observed vertical profiles of mean wind components and potential temperature and the calculated Ri profile in the nocturnal PBL under moderately stable conditions. [From Deardorff (1978); after Izumi and Barad (1963).]

For moderately stable BLs in which turbulence is largely continuous in space and time, the BL is far from well-mixed, but the Richardson number Ri remains less than 1/4 (see figure above). In extremely stable boundary layers, the turbulence is sporadic and the mean Ri can be 1 or more (see below). The low-level veering of the wind with height is much larger in very stable boundary lay-

Arya

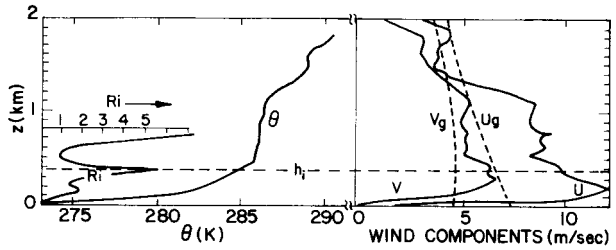

Fig. 6.8 Observed wind and potential temperature profiles under very stable (sporadic turbulence) conditions at night during the Wangara Experiment. [From Deardorff (1978).]

ers, where most of the surface stress is distributed as momentum flux convergence near to the bottom of the BL (see below).

Arya, fig. 6.10

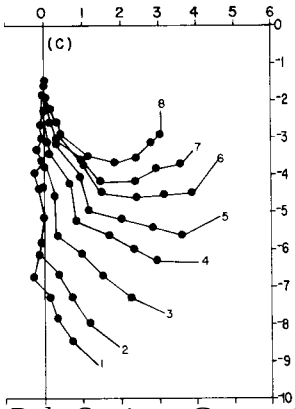

Wind hodographs at South Pole Station. Categories 1-8 correspond to increasingly stable BLs; dots are composites of measurements at 0.5, 1, 2, 4, 8, 12, 16, 20, 24, 32 m *y*-axis is in surface wind direction. Note large turning of wind with height in stable BLs.

Lecture 5. Surface roughness and the logarithmic sublayer

(Garratt, Ch 3: similarity theory; Ch. 4: surface characteristics)

Near a solid boundary, in the 'surface layer', vertical fluxes are transported primarily by eddies with a lengthscale much smaller than in the center of the BL. A very successful similarity theory is based on dimensional reasoning (Monin and Obuhkov, 1954). It postulates that near any given surface, the wind and thermodynamic profiles should be determined purely by the height z above the surface (which scales the eddy size) and the surface fluxes which drive turbulence:

1. Surface mom. flux $\overline{u'w'}_0$ (often expressed as **friction velocity** $u_* = (\overline{u'w'}_0)^{1/2}$)
2. Surface buoyancy flux $B_0 = \overline{w'b'}_0$

One can construct from these fluxes the

Obuhkov length $L = -u_*^3/kB_0$ (positive for stable, negative for unstable BLs)

Here $k = 0.4$ is the **von Karman constant**, whose physical significance we'll discuss shortly. In the ABL, a typical u_* might be 0.3 m s^{-1} and a typical range of buoyancy flux would be -3×10^{-4} m^{2}s^{-3}(nighttime) to 1.5×10^{-2} m^{2}s^{-3}(midday) (i. e. a virtual heat flux of -10 W m^{-2} at night, 500 W m^{-2} at midday), giving L = 200 m (nighttime) and -5 m (midday).

The logarithmic sublayer (Garratt, p. 41)

At height z, the characteristic eddy size, velocity, and buoyancy scale with z, u_*, and B_0/u_*. If the buoyant acceleration acts over the eddy height, it would make a vertical velocity $(z\delta b)^{1/2} = (zB_0/u_*)^{1/2}$. If $z < |L|$, this buoyancy driven contribution to the vertical velocity is much smaller than the shear-driven inertial velocity scale u_*, so buoyancy will not significantly affect the eddies. In this case, the mean wind shear will depend only on u_* and z, so dimensionally

$$d\bar{u}/dz = u_*/kz \quad (z < |L|) \tag{1}$$

This can also be viewed in terms of mixing length theory, with eddy diffusion

$K_m \propto$ (velocity)(length) = $(u_*)(kz)$

$\overline{u'w'}_0 = -K_m d\bar{u}/dz \;\Rightarrow\; u_*^2 = ku_*z\, d\bar{u}/dz$ (equivalent to (1))

The von Karman constant k is the empirically determined constant of proportionality in (1). Integrating, we get the **logarithmic velocity profile law**:

$$\bar{u}(z)/u_* = k^{-1} \ln(z/z_0) \quad (z << |L|) \tag{2}$$

The constant of integration z_0 depends on the surface and is called the **roughness length**. It is loosely related to the typical height of closely spaced surface obstacles, often called roughness elements (e. g. water waves, trees, buildings, blades of grass). It depends on the distribution as well as the height h_c of roughness elements (see figure below), but as a rule of thumb,

$$z_0 \sim 0.1h_c$$

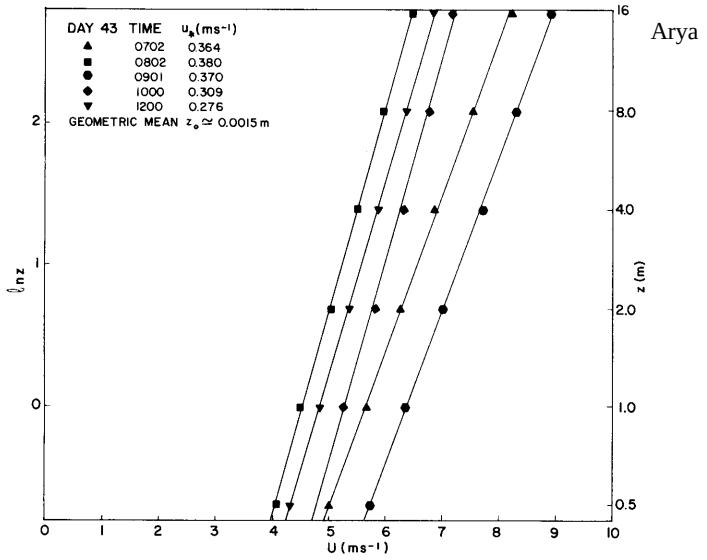

Arya

Fig. 10.4 Comparison of the observed wind profiles in the neutral surface layer of day 43 of the Wangara Experiment with the log law [Eq. (10.6)] (solid lines). [Data from Clarke *et al.* (1971).]

Example of logarithmic velocity profile in a neutral surface layer.

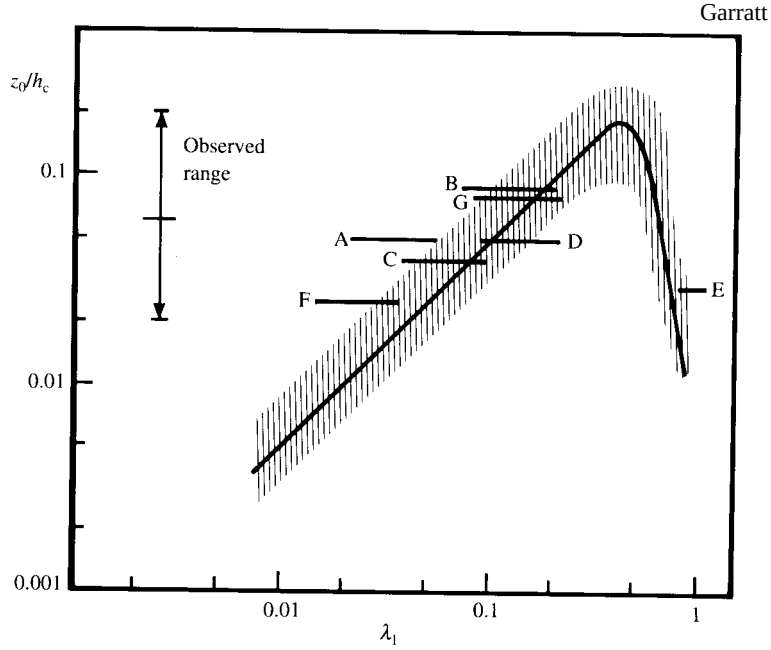

Garratt

Fig. 4.1 Variation of z_0/h_c with element density, based on the results of Kutzbach (1961), Lettau (1969) and Wooding *et al.* (1973), represented by the shaded area and solid curve. Some specific atmospheric data are also shown as follows: A and B, trees; C and D, wheat; E, pine forest; F, parallel flow in a vineyard; G, normal flow in a vineyard. Analogous wind-tunnel data are described in Seginer (1974). From Garratt (1977b).

Dependence of roughness length on density λ of roughness elements.

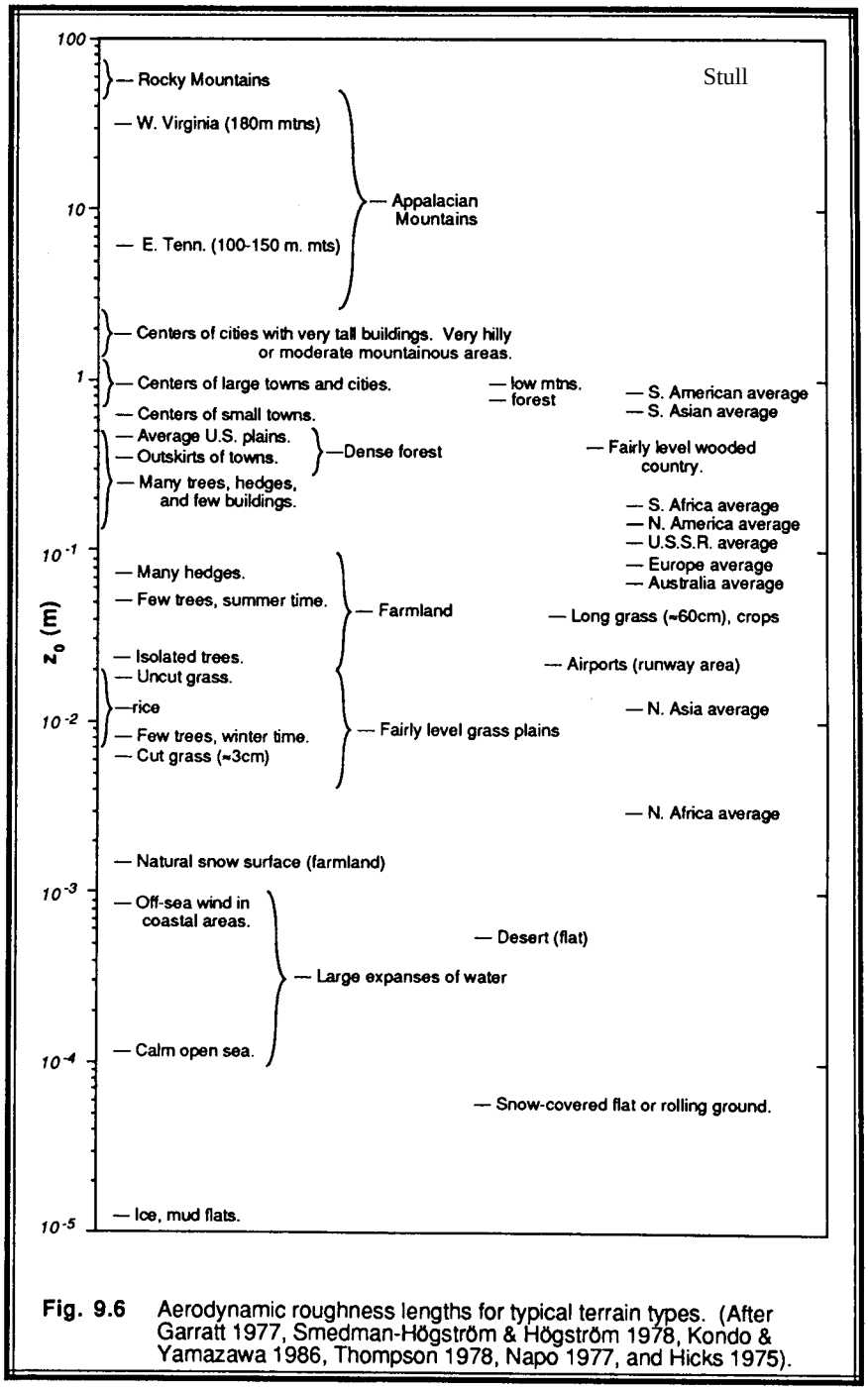

Fig. 9.6 Aerodynamic roughness lengths for typical terrain types. (After Garratt 1977, Smedman-Högström & Högström 1978, Kondo & Yamazawa 1986, Thompson 1978, Napo 1977, and Hicks 1975).

z_0 varies greatly depending on the surface, but a typical overall value for land surfaces is $z_0 = 0.1$ m (see table on next page). In the rare circumstance that the surface is so smooth that the viscous sublayer is deeper than roughness elements,

$$z_0 \sim 0.1\nu/u_* \sim 0.015 \text{ mm for } u_* = 0.1 \text{ m s}^{-1}$$

Near the surface, the log profile fits best if z is offset by a **zero-plane displacement** d_0 which lies between 0 and the height h_c of roughness elements, and is typically roughly $0.7h_c$.

$$\bar{u}(z)/u_* = k^{-1} \ln([z-d_0]/z_0) \quad (z << |L|) \tag{3}$$

Roughness of Water Surfaces (Garratt, p. 97-100)

The roughness of a water surface depends on wind speed and the spectrum of waves. A strong wind blowing from S to N across the SR 520 bridge shows the importance of fetch on wave spectrum. On the south side, large waves will be crashing onto the bridge deck. On the N side, the water surface will be nearly smooth except for short wavelength ripples ('cats paws') associated with wind gusts. As one looks further N from the bridge, one sees chop, then further downwind, longer waves begin to build. It can take a fetch of 100 km for the wave spectrum to reach the steady state or fully developed sea assumed by most formulas for surface roughness. It is thought that much of the wind stress is associated with boundary layer separation at sharp wave crests of breaking waves or whitecaps, which start forming at wind speeds of 5 m s^{-1} and cover most of the ocean surface at wind speeds of 15 m s^{-1} or more.

For wind speeds below 2.5 m s^{-1}, the water surface is approximately aerodynamically smooth, and the viscous formula for z_0 applies. For intermediate wind speeds, the flow is aerodynamically smooth over some parts of the water surface but rough around and in the lee of the breaking whitecaps, and for wind speeds above 10 m s^{-1} it is fully rough. For rough flow, Charnock (1955) suggested that z_0 should depend only on the surface stress on the ocean and the gravitational restoring force, i. e., u_* and g, leading to **Charnock's formula**:

$$z_0 = \alpha_c u_*^2/g, \quad (\alpha_c = 0.016 \quad 20\% \text{ from empirical measurements}).$$

This formula appears reasonably accurate for 10 m wind speeds of 4-50 m s^{-1}. For 10 m wind speeds of 5-10 m s^{-1}, this gives roughness lengths of 0.1 - 1 mm, much less than almost any land surface. Even the heavy seas under in a tropical storm have a roughness length less than mown grass! This is because (a) the large waves move along with the wind, and (b) drag seems to mainly be due to the vertical displacements involved directly in breaking, rather than by the much larger amplitude long swell. The result is that near-surface wind speeds tend to be much higher over the ocean, while surface drag tends to be smaller over the ocean than over land surfaces.

Snow and Sand Surfaces (Garratt, p. 87-88)

The roughness of sand or snow surfaces also increases of wind speed, apparently due to suspension of increasing numbers of particles. Charnock's dimensional argument again applies, and remarkably, the same α_c appears to work well, though now the minimum z_0 is larger (typically at least 0.05 mm), associated with the roughness of the underlying solid surface.

Bulk Aerodynamic Drag Formula (Garratt, p. 100-101)

Suppose that a wind measurement is taken at a standard reference level z_R within the log layer (A typical shipboard height of z_R = 10 m is often used for ocean measurements). Then (ignoring zero-plane displacement for simplicity), $\bar{u}(z_R) = u_* k^{-1} \ln(z_R/z_0)$. The bulk aerodynamic formula relates the surface stress $\rho_0 \overline{u'w'}$ to the reference wind speed in terms of a drag coefficient C_{DN} which depends on surface roughness:

$$-\rho_0 \overline{u'w'} = \rho_0 u_*^2 = \rho_0 C_{DN} \bar{u}^2(z_R),$$

Arya

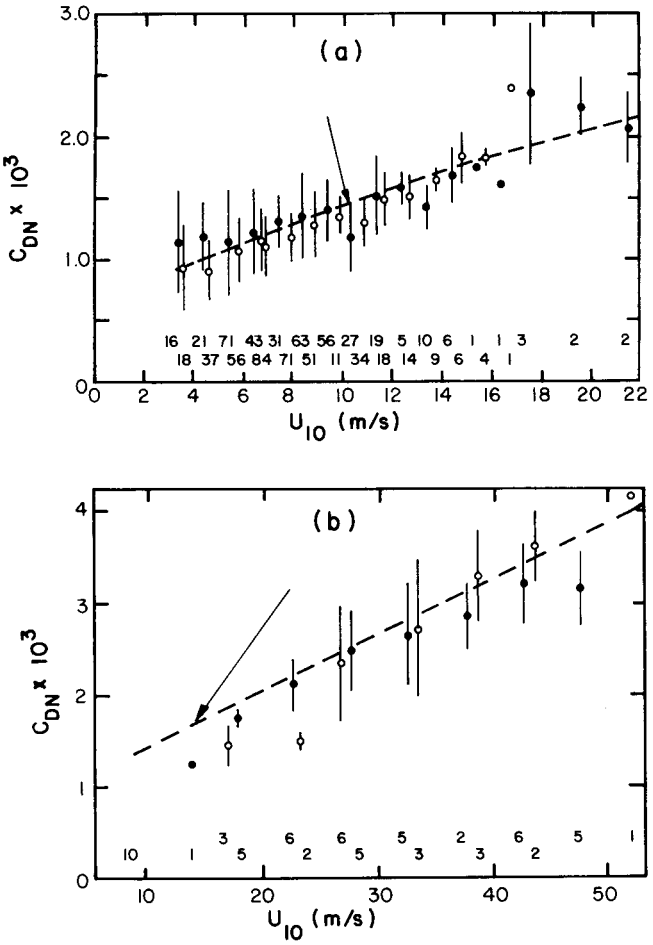

Fig. 13.4 Neutral drag coefficient as a function of wind speed at a 10-m height compared with Charnock's formula [Eq. (13.5), indicated by the arrows in (a) and (b)] with $a = 0.0144$. Block-averaged values are shown for (a) 1-m sec^{-1} intervals, based on eddy correlation and profile methods, and (b) 5-m sec^{-1} intervals, based on geostrophic departure method and wind flume simulation experiments. [After Garratt (1977).]

(4)

Garratt

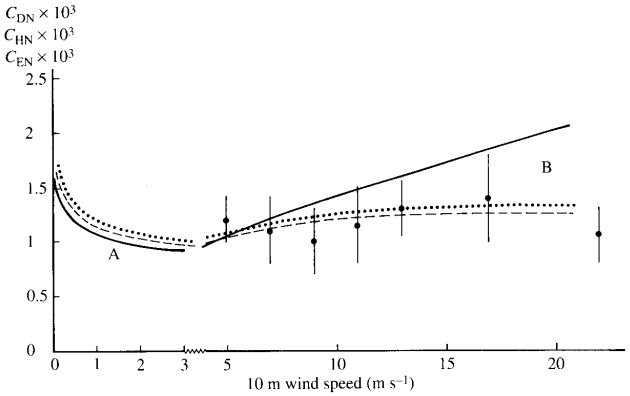

Fig. 4.9 Drag coefficient C_{DN}, heat transfer coefficient C_{HN} and water vapour transfer coefficient C_{EN} as functions of the 10 m wind speed. Curves A are for smooth flow: solid curve C_{DN} (Eq. 4.22); pecked curve, C_{HN} (Eqs. 4.10 and 4.26a); dotted curve, C_{EN} (Eqs. 4.11 and 4.26b). Curves B are for rough flow: solid curve, C_{DN} (Eq. 4.23); pecked curve, C_{HN} (Eqs. 4.10 and 4.27); dotted curve, C_{EN} (Eqs. 4.11 and 4.28). Observational data are from Large and Pond (1982).

$$C_{DN} = k^2/\{\ln(z_R/z_0)\}^2 \quad (5)$$

The *N*, for 'neutral', in the suffix is to remind us that this formula only applies if when $z_R << |L|$, which for typical reference heights (2 m or 10 m) requires fairly neutrally stratified conditions, as are often observed over the oceans but less often over land. For z_R = 10 m wind speed and z_0 = 0.1 m, $C_{DN} = 8 \times 10^{-3}$

Over the water, C_{DN} is a function of surface roughness u_* and hence implicitly of wind speed. While Charnock's formula gives an awkward transcendental equation to solve for C_{DN} in terms of $\bar{u}(z_R)$, a good approximation using mean 10 m wind speed u_{10} is:

$$C_{DN} = (0.75 + 0.067u_{10}) \times 10^{-3} \quad \text{(water, neutrally stratified BL)}$$

Heat and Moisture Transfer in Neutral Conditions

Let *a* be a scalar (θ, *q*, etc.) transported by the turbulence. In the log-layer, we again might hope for a flux-gradient relation of the form

$$\overline{w'a'} = K_a d\bar{a}/dz, \quad K_a = k_a z u_*$$

The nondimensional constant k_a need not equal the von Karman constant, since momentum perturbations of fluid parcels are affected by eddy-induced pressure gradients, while scalars are not. However, empirical measurements do suggest that $k_a = k$ in a neutral BL. A scale for turbulent perturbations a' in the log layer is:

$$a_* = \overline{w'a'}|_0/u_*$$

Since the flux is approximately equal to its surface value throughout the surface layer,

$$d\bar{a}/dz = -\overline{w'a'}|_0 / (kzu_*) = -a_*/kz$$

$$\bar{a}(z) - \bar{a}_0 = -a_*/k \ln(z/z_{0a})$$

This has the same logarithmic form as the velocity profile, but the scaling length z_{0a} need not be (and usually isn't) the same as z_0. In fact, it is often much smaller, because pressure (form) drag on roughness elements helps transfer momentum between the interfacial (viscous) sublayer around roughness elements to the inertial sublayer . No corresponding nonadvective transfer mechanism exists for scalars, so they will be transferred less efficiently out of the interfacial layer ($z_a < z_0$) unless their molecular diffusivity is much larger than that of heat.

This can be converted into a bulk aerodynamic formula like (5), but the transfer coefficient may be different:

$$\rho_0\overline{w'a'} = \rho_0 C_{aN}\bar{u}(z_R)\{\bar{a}_0 - \bar{a}(z_R)\},$$

$$C_{aN} = k^2/\{\ln(z_R/z_0)\ln(z_R/z_{0a})\}$$

For most land surfaces, the heat and moisture scaling lengths z_{0H} and z_{0q} are 10-30% as large as z_0, resulting in typical C_{HN} of 0.7-0.95 C_{DN} . For water surfaces, the heat and moisture coefficients are comparable to C_{DN} for 10 m winds of 7 m s^{-1} or less, but remain around 1-1.5 $\times 10^{-3}$ rather than increasing as wind speed increases. This corresponds to heat and moisture scaling lengths appropriate for laminar flow even at high wind speeds. For instance, ECMWF uses z_{0H}, z_{0q} = (0.4, 0.62)ν/u_* following Brutsaert (1982).

Bulk aerodynamic formulas are quite accurate as long as (i) an appropriate transfer coefficient

Arya

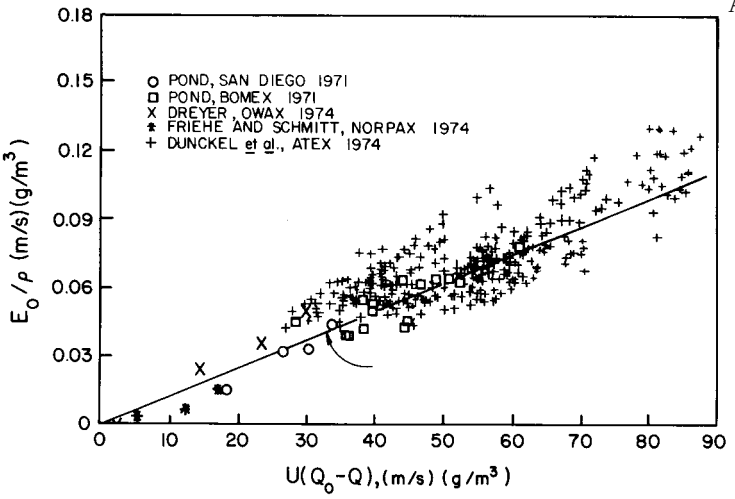

Fig. 13.6 Observed moisture flux at the sea surface as a function of $U(Q_0 - Q)$ compared with Eq. (13.8) with $C_W = 1.32 \times 10^{-3}$, indicated by the arrow. [After Friehe and Schmitt (1976).]

is used for the advected quantity, the reference height, and the BL stability, and (ii) Temporal variability of the mean wind speed or air-sea differences are adequately sampled. The figure below shows comparisons between direct (eddy-correlation) measurements of moisture flux in nearly neutrally stratified BLs over ocean surfaces compared with a bulk formula with constant $C_q = 1.32 \times 10^{-3}$. In individual cases, discrepancies of up to 50% are seen (which are as likely due to sampling scatter in the measured fluxes as to actual problems with the bulk formula), but the overall trend is well captured. However, due to this type of scatter, no two books or papers seem to exactly agree on the appropriate formulas to use, though all agree within about 20%.

Lecture 6. Monin-Obuhkov similarity theory (Garratt 3.3)

Because so many BL measurements are made within the surface layer (i. e. where wind veering with height is insignificant) but stratification effects can be important at standard measurement heights of 2 m (for temperature and moisture) and 10 m (for winds), it is desirable to correct the log-layer profiles for stratification effects.

Based on the scaling arguments of last lecture, Monin and Obuhkov (1954) suggested that the vertical variation of mean flow and turbulence characteristics in the surface layer should depend only on the surface momentum flux as measured by friction velocity u_*, the buoyancy flux B_0, and the height z. One can form a single nondimensional combination of these, which is traditionally chosen as the **stability parameter**

$$\zeta = z/L$$

The logarithmic scaling regime of last time corresponds to $\zeta << 1$.

Thus, within the surface layer, we must have

$$(kz/u_*)(\partial\overline{u}/\partial z) = \phi_m(\zeta) \quad (1)$$

$$(kz/\overline{\theta}_*)(\partial\overline{\theta}/\partial z) = \phi_h(\zeta) \quad (2)$$

where $\phi_m(\zeta)$ and $\phi_h(\zeta)$ are **universal similarity functions** which relate the fluxes of momentum and θ (i. e. sensible heat) to their mean gradients. Other adiabatically conserved scalars should behave similarly to θ since the transport is associated with eddies which are too large to be affected by molecular diffusion or viscosity. To agree with the log layer scaling, $\phi_m(\zeta)$ and $\phi_h(\zeta)$ should approach 1 for small ζ.

We can express (1) and (2) in other equivalent forms. First, we can regard them as defining surface layer **eddy viscosities**:

$$K_m = -\overline{u'w'} / (\partial\overline{u}/\partial z) = u_*^2/(\phi_m(\zeta)\, u_*/kz) = ku_*z / \phi_m(\zeta)$$

$$K_h = -\overline{w'\theta'} / (\partial\overline{\theta}/\partial z) = u_*\theta_*/(\phi_h(\zeta)\, \theta_*/kz) = ku_*z / \phi_h(\zeta)$$

By analogy to the molecular Prandtl number, the **turbulent Prandtl number** is their ratio:

$$\mathrm{Pr}_t = K_m / K_h = \phi_h(\zeta) / \phi_m(\zeta)$$

Another commonly used form of the similarity functions is to measure stability with gradient Richardson number Ri instead of ζ. Recalling that $N^2 = -d\overline{b}/dz$, and again noting that the surface layer is thin, so vertical fluxes do not vary significantly with height within it, Ri is related to ζ as follows:

$$\begin{aligned}
\mathrm{Ri} &= (-d\overline{b}/dz) / (d\overline{u}/dz)^2 \\
&= (\overline{w'b'}_0 /K_h)/ (\overline{u'w'}_0/K_m)^2 \\
&= (B_0\phi_h(\zeta) /ku_*z) / (u_*^2\phi_m(\zeta)/ku_*z))^2 \\
&= \zeta\phi_h/\phi_m^2
\end{aligned}$$

Given expressions for $\phi_m(\zeta)$ and $\phi_h(\zeta)$, we can write ζ and hence the similarity functions and eddy diffusivities in terms of Ri. The corresponding formulas for dependence of eddy diffusivity on Ri (stability) are often used by modellers even outside the surface layer, with the neutral K_m and K_m

estimated as the product of an appropriate velocity scale and lengthscale.

Field Experiments

The universal functions must be determined empirically. In the 1950-60s, several field experiments were conducted for this purpose over regions of flat, homogeneous ground with low, homogeneous roughness elements, culminating in the 1968 Kansas experiment. This used a 32 m instrumented tower in the middle of a 1 mi^2 field of wheat stubble. Businger et al. (1971, JAS, **28**, 181-189) documented the relations below, which are still accepted:

$$\phi_m = \begin{cases} (1-\gamma_1\zeta)^{-1/4}, & \text{for } -2 < \zeta < 0 \quad \text{(unstable)} \\ 1+\beta\zeta, & \text{for } 0 \le \zeta < 1 \quad \text{(stable)} \end{cases}$$

$$\phi_h = \begin{cases} \mathrm{Pr}_{tN}(1-\gamma_2\zeta)^{-1/2}, & \text{for } -2 < \zeta < 0 \quad \text{(unstable)} \\ \mathrm{Pr}_{tN}+\beta\zeta, & \text{for } 0 \le \zeta < 1 \quad \text{(stable)} \end{cases}$$

The values of the constants determined by the Kansas experiment were

$$\mathrm{Pr}_{tN} = 0.74,\ \beta = 4.7,\ \gamma_1 = 15,\ \gamma_2 = 9\ .$$

The quality of the fits to observations are shown on the next page. Other experiments have yielded somewhat different values of the constants (Garratt, Appendix 4, Table A5), so we will follow Garratt (p. 52) and Dyer (1974, *Bound-Layer Meteor*., **7**, 363-372*)* and assume:

$$\mathrm{Pr}_{tN} \approx 1,\ \beta \approx 5,\ \gamma_1 \approx\ \gamma_2 \approx 16$$

In neutral or stable stratification, this implies $\phi_m = \phi_h$, i. e. pressure perturbations do not affect the eddy transport of momentum relative to scalars such as heat, and the turbulent Prandtl number is 1. In unstable stratification, the eddy diffusivity for scalars is more than for momentum.

Solving these relations for Ri,

$$\zeta = \begin{cases} \mathrm{Ri}, & \text{for } -2 < \mathrm{Ri} < 0 \quad \text{(unstable)} \\ \dfrac{\mathrm{Ri}}{1-5\mathrm{Ri}}, & \text{for } 0 \le \mathrm{Ri} < 0.2 \quad \text{(stable)} \end{cases}$$

Limiting cases (Garratt, p. 50)

(i) Neutral limit. ϕ_m , $\phi_h \to 1$ as $\zeta \to 0$ as expected, recovering log-layer scaling for $z << |L|$.

(ii) Stable limit. Expect eddy size to depend on L rather than z (z -less scaling), since our scaling analysis of last time suggests that stable buoyancy forces tend to suppress eddies with a scale larger than L. This implies that the eddy diffusivity

$$K_m = ku_*z/\phi_m \propto \text{(velocity)(length)} \propto u_*L \ \Rightarrow\ \phi_m \sim z/L = \zeta$$

and similarly for K_h. The empirical formulas imply $K_m \sim \beta\zeta$ for large ζ, which is consistent with this limit. Hence they are usually assumed to apply for all positive ζ.

Arya 11.2,3

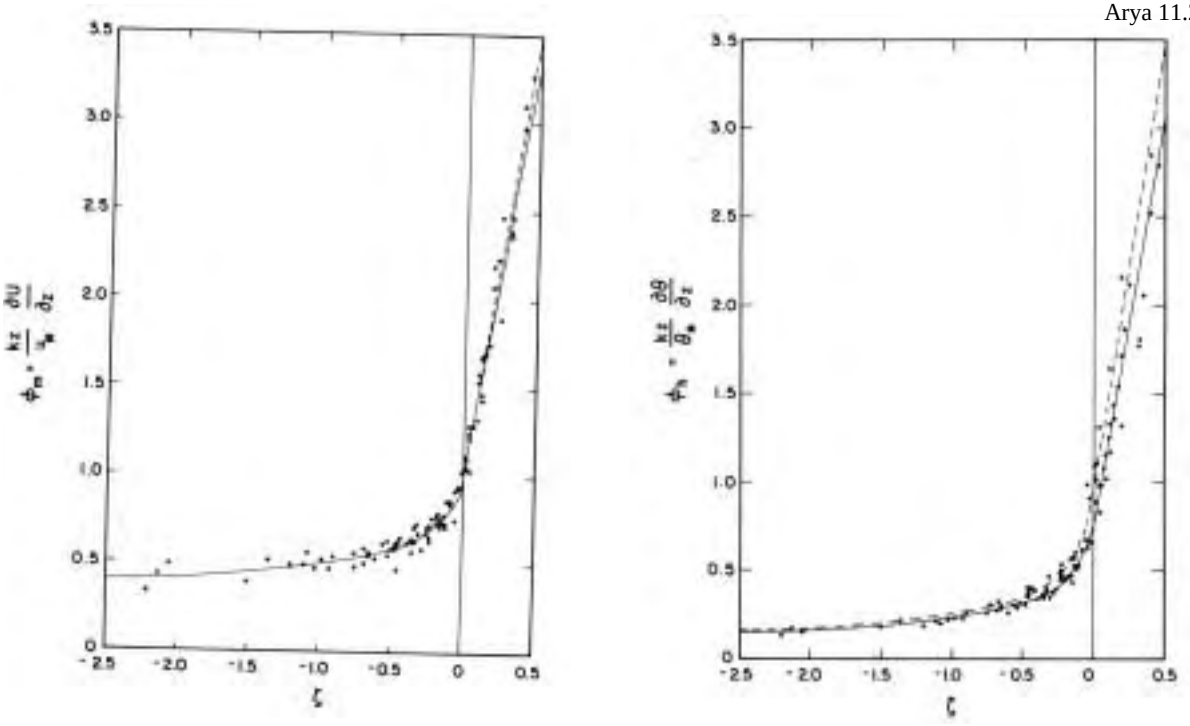

Empirical determination of similarity functions from Kansas experiment

Arya11.5

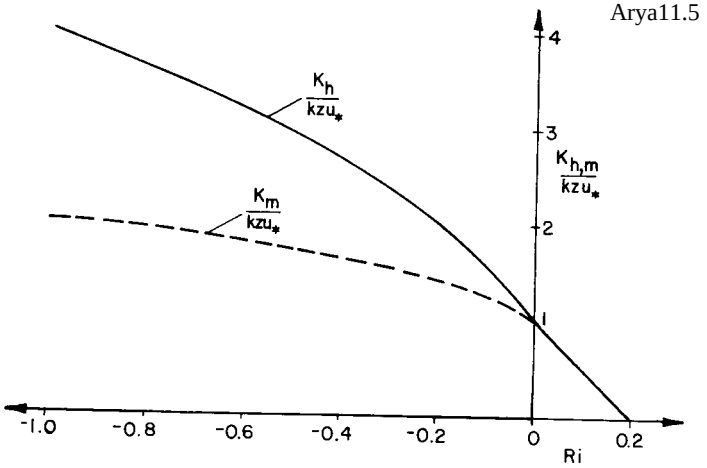

Eddy viscosity and diffusivity as functions of stability, measured by Ri

(iii) Unstable limit. Convection replaces shear as the main source of eddy energy, so we expect the eddy velocity to scale with the buoyancy flux B_0 and not the friction velocity. We still assume that the eddy size is limited by the distance z to the boundary. In this 'free convective scaling', the eddy velocity scale is $u_f = (B_0 z)^{1/3}$ and the eddy viscosity should go as

$$K_m = k u_* z/\phi_m \propto u_f z \quad \Rightarrow \quad \phi_m \propto u_*/u_f \propto (-z/L)^{-1/3} = (-\zeta)^{-1/3}$$

A similar argument applies to eddy diffusivity for scalars K_h. The empirical relations go as $(-\zeta)^{-1/2}$ for scalars and $(-\zeta)^{-1/4}$ for momenta, but reliable measurements only extend out to $\zeta = -2$. Free convective scaling may be physically realized, but only at higher ζ.

Wind and thermodynamic profiles

The similarity relations can be integrated with respect to height to get:

$$\bar{u}/u_* = k^{-1} [\ln(z/z_0) - \psi_m(z/L)]$$

$$(\theta_0 - \bar{\theta})/\theta_* = k^{-1} [\ln(z/z_{T0}) - \psi_h(z/L)] \text{ (and similarly for other scalars)}$$

where if $x = (1 - \gamma_1 \zeta)^{1/4}$,

$$\psi_m(\zeta) = \int_0^\zeta [1 - \phi_m(\zeta')] d\zeta'/\zeta'$$

$$= \begin{cases} \ln\left(\left(\frac{1+x^2}{2}\right)\left(\frac{1+x}{2}\right)^2\right) - 2\tan^{-1}x + \frac{\pi}{2}, & \text{for } -2 < \zeta < 0 \text{ (unstable)} \\ -\beta\zeta, & \text{for } 0 \le \zeta \text{ (stable)} \end{cases}$$

$$\psi_m(\zeta) = \int_0^\zeta [1 - \phi_h(\zeta')] d\zeta'/\zeta'$$

$$= \begin{cases} 2\ln\left(\frac{1+x^2}{2}\right), & \text{for } -2 < \zeta < 0 \text{ (unstable)} \\ -\beta\zeta, & \text{for } 0 \le \zeta \text{ (stable)} \end{cases}$$

Wind profiles in stable, neutral, and unstable conditions are shown in the figure below. Low-level wind and shear are reduced compared to the log profile in unstable conditions, when K_m is larger. From these,we derive bulk aerodynamic coefficients which apply in non-neutral conditions:

$$C_D = \frac{k^2}{[\ln(z/z_0) - \psi_m(z/L)]^2}, \quad C_H = \frac{k^2}{[\ln(z/z_{T0}) - \psi_m(z/L)][\ln(z/z_{T0}) - \psi_h(z/L)]} \qquad (3)$$

These decrease considerably in stable conditions (see figure on next page). In observational analyses and numerical models, (3) and the formula for L are solved simultaneously to find surface heat and momentum fluxes from the values of u and $\theta_0 - \theta$ at the measurement or lowest grid-level z

.

Garratt

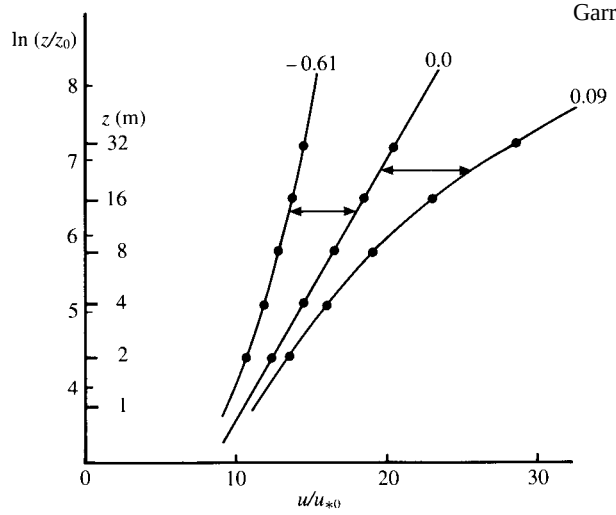

Fig. 3.5 Three wind profiles from the Kansas field data (Izumi, 1971) plotted in normalized form at three values of the gradient Ri ($z = 5.66$ m). Both normalized and absolute heights are shown, whilst the magnitude of the horizontal arrows indicates the effect of buoyancy on the wind relative to the neutral profile (see Eq. 3.34).

Garratt

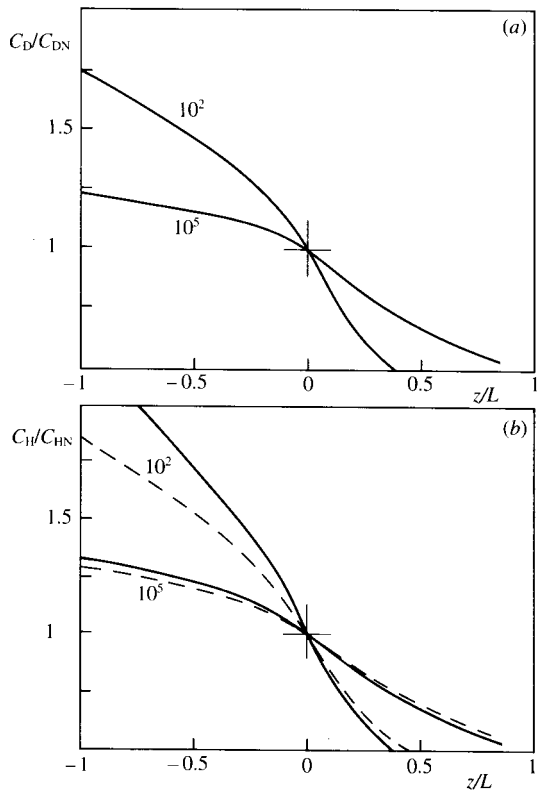

Fig. 3.7 Values of (a) C_D/C_{DN} and (b) C_H/C_{HN} as functions of z/L for two values of z/z_0 as indicated. In (b), the solid curves have $z_0 = z_T$, and the pecked curves have $z_0/z_T = 7.4$ (see Chapter 4).

Scaling for the entire boundary layer (Garratt, 3.2)

In general, the BL depth h and turbulence profile depend on many factors, including history, stability, baroclinicity, clouds, presence of a capping inversion, etc. Hence universal formulas for the velocity and thermodynamic profiles above the surface layer (i. e. where transports are primarily by the large, BL-filling eddies) are rarely applicable.

However, a couple of special cases are illuminating to consider. The first is a **well-mixed** BL (homework), in which the fluxes adjust to ensure that the tendency of θ, q, and velocity remain the same at all levels. Well mixed BLs are usually either strongly convective, or strongly driven stable BLs capped by a strong inversion. Mixed layer models incorporating an **entrainment closure** for determining the rate at which BL turbulence incorporates above-BL air into the mixed layer are widely used.

The other interesting (though rarely observable) case is a steady-state, neutral, barotropic BL. This is the turbulent analogue to a laminar Ekman layer. Here, the fundamental scaling parameters are $G = |\mathbf{u}_g|$, f, and z_0. Out of these one can form one independent nondimensional parameter, the surface Rossby number $\mathrm{Ro}_s = G/fz_0$ (which is typically 10^4 -10^8). The friction velocity (which measures surface stress) must have the form

$$u_* / G = F(\mathrm{Ro}_s)$$

Hence, one can also regard u_* / G as a proxy nondimensional control parameter in place of Ro_s. The steady-state BL momentum equations are

$$f(u - u_g) = -\frac{\partial}{\partial z}\overline{v'w'}$$

$$f(v - v_g) = \frac{\partial}{\partial z}\overline{u'w'}$$

On the next page are velocity and momentum flux profiles from a direct numerical simulation (384×384×85 gridpoints) in which $u_*/G = 0.053$ (Coleman 1999, *J. Atmos. Sci*, **56**, 891-900). The geostrophic wind is oriented in the x direction, and is independent of height (the barotropic assumption). Height is nondimensionalized by $\delta = u_*/f$. In the thin surface layer, extending up to $z = 0.02\delta$, the wind increases logarithmically with height without appreciable turning (this is most clearly seen on the wind hodograph), and is turned at 20° from geostrophic (this angle is an increasing function of u_*/G) The neutral BL depth , defined as the top of the region of significantly ageostrophic mean wind, is

$$h_N = 0.8u_*/f$$

For $u_* = 0.3$ m s^{-1} and $f = 10^{-4}$ s^{-1}, $h_N = 2.4$ km. Real ABLs are rarely this deep because of stratification aloft, but fair approximations to the idealized turbulent Ekman layer can occur in strong-winds over the midlatitude oceans. The wind profile qualitatively resembles an Ekman layer of with an Ekman thickness $(2\nu/f)^{1/2} = 0.12u_*/f$, except much more of the wind shear is compressed into the surface layer.

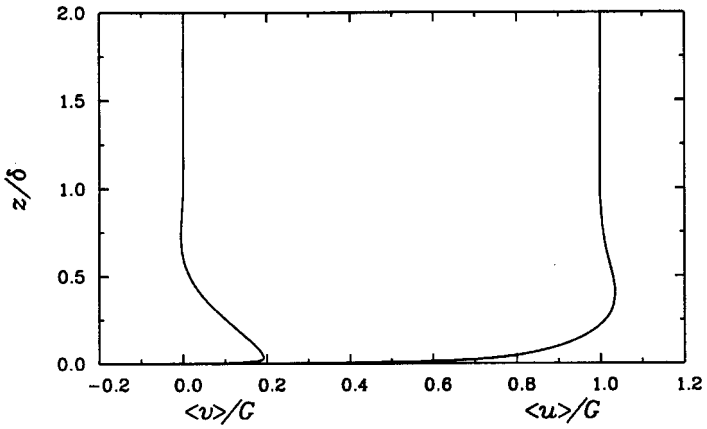

Wind profiles in a neutral barotropic BL with u_*/G = 0.053 (Coleman 1999).

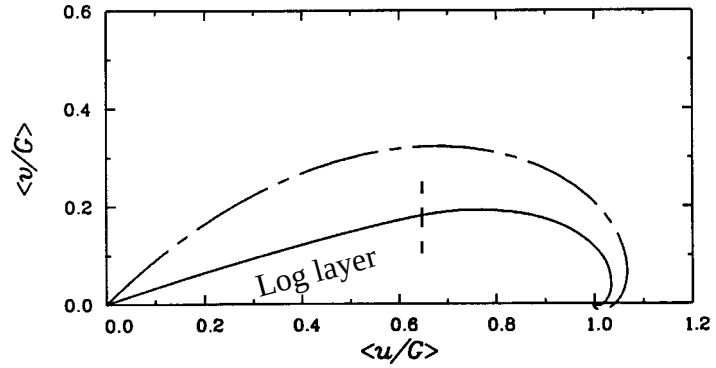

Wind hodograph (dashed = Ekman layer). Log (surface) layer is part of profile to right of dashes.

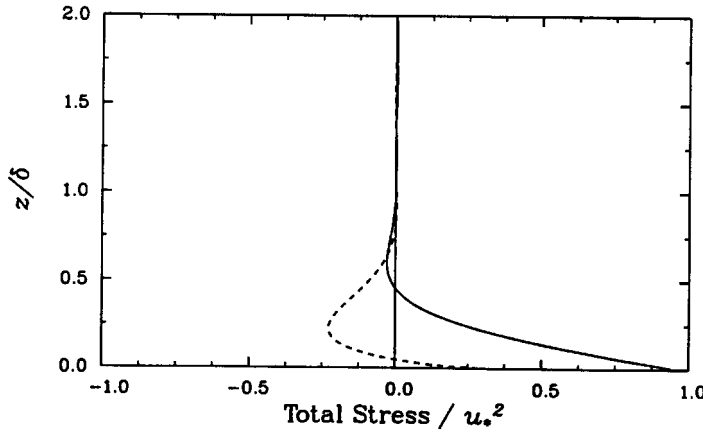

Stress profiles in geostrophic coordinate system. Solid = in direction of $\mathbf{u}_g$, dashed = transverse dir.

The wind and momentum flux profiles depend weakly on Ro_s, but we will describe below a scaling that collapses these into a single universal profile independent of Ro_s above the surface layer As we go up through the boundary layer, the magnitude of the momentum flux will decrease from u_*^2 at the surface to near zero at the BL top, so throughout the BL, the momentum flux will be $O(u_*^2)$(Hence, throughout the BL the turbulent velocity perturbations u', w' should scale with u_* to be consistent with this momentum flux). We assume that the BL depth scales with u_*/f. These scalings suggest a nondimensionalization of the steady state BL momentum equations:

$$\frac{u-u_g}{u_*} = -\frac{\partial(\overline{v'w'}/u_*^2)}{\partial(zf/u_*)}$$

$$\frac{v-v_g}{u_*} = \frac{\partial(\overline{u'w'}/u_*^2)}{\partial(zf/u_*)}$$

If we adopt a coordinate system in which the x axis is in the direction of the surface-layer wind, the boundary conditions on the momentum flux are

$$\overline{u'w'}/u_*^2 = -1,\ \overline{v'w'}/u_*^2 = 0 \quad \text{as } z \to 0 \text{ (at surface layer top)}$$

$$\overline{u'w'}/u_*^2 = 0\ ,\ \overline{v'w'}/u_*^2 = 0 \quad \text{as } z \to \infty$$

This momentum balance and boundary conditions are consistent with a universal **velocity defect law** of the form:

$$(u-u_g)/u_* = F_x(zf/u_*)$$

$$(v-v_g)/u_* = F_y(zf/u_*)$$

where F_x and F_y are universal functions (which must be determined empirically or via LES simulation) that apply for any Ro_s. In the surface layer , these universal functions cease to apply and the logarithmic wind profile $u/ku_* = \ln(z/z_0)$, $v = 0$ matches onto the defect laws. The figure below shows that Coleman's simulations and laboratory experiments with different parameters are consistent with the same F_x and F_y, supporting their universality.

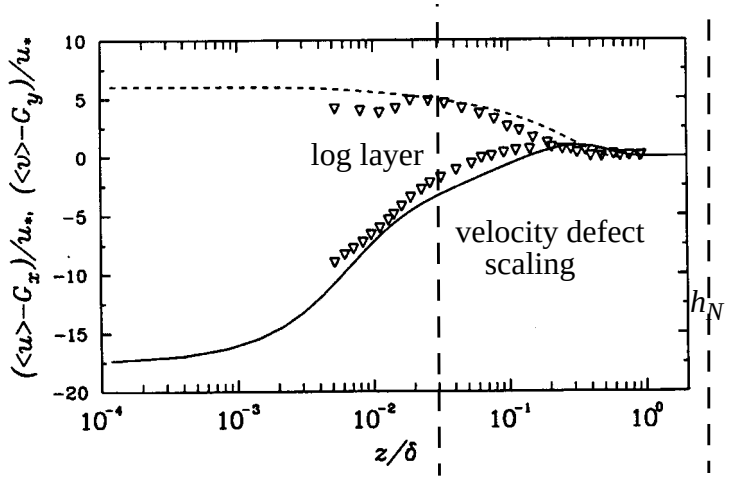

Lecture 7. More on BL wind profiles

Stability

Above the surface layer, the wind profile is also affected by stability. As we mentioned previously, unstable BLs tend to have much more well-mixed wind profiles than stable BLs. The figures below show observations from the Wangara experiment on how the velocity defect laws and temperature profile are altered by BLstability (as measured by *h/L)*. Within stability classes, the velocity profiles collapse when scaled with a velocity scale u_* and the observed BL depth *h*, but there is a large difference between the stability classes.

Baroclinicity

We would expect baroclinicity (vertical shear of geostrophic wind) to also affect the observed wind profile. This is most easily seen for an Ekman layer in a geostrophic wind with constant vertical shear:

$$\mathbf{u}_g(z) = (G + Mz, Nz), \text{ where } M = -(g/fT_0)\partial T/\partial y, \; N = (g/fT_0)\,\partial T/\partial x$$

$$-f(v - Nz) = \nu\, d^2u/dz^2$$

$$f(u - G - Mz) = \nu\, d^2v/dz^2$$

$$u(0) = 0,\ u \to G + Mz \text{ as } z \to \infty$$

$$v(0) = 0,\ v \to Nz \text{ as } z \to \infty$$

Resultant BL velocity profile just has thermal wind added onto it:

$$u(z) = G(1 - e^{-\zeta}\cos\zeta) + Mz$$

$$v(z) = G\, e^{-\zeta}\sin\zeta + Nz \quad (\zeta = z/\delta,\ \delta = (2\nu/f)^{1/2})$$

This can considerably alter the BL wind profile. The largest crossing angle of the surface wind direction across the isobars is seen if $M < 0$, $N > 0$,corresponding to surface cold advection. This effect is clearly seen in the figure below of crossing angle vs. thermal wind orientation in 23000 wind profiles over land (Hoxit 1974). On weather maps, one can see much larger crossing angles behind cold fronts than ahead of them. On the other hand, the wind turns less with height if $N > 0$ (surface cold advection)

Turbulence Profiles (Garratt 3.3)

For applications such as the dispersion of pollutants, it is important to understand the characteristics of turbulence in different types of BL. LES simulations illustrate some of these characteristics. Most of the figures below are from Moeng and Sullivan (1994, *JAS*, **51**, 999-1022).

Neutral BLs

Moeng and Sullivan simulated a neutral BL capped by a strong (8 K) inversion at a height of $z_i = 500$ m. The geostrophic wind is 15 m s^{-1} in the +*x* direction and $u_* = 0.5$ m s^{-1}. The figures on 4.1.4 show *x*-*y* slices of u' at various heights, and the wind hodograph. Because of the capping inversion, the wind shear within the bulk of the BL is fairly small (nearly a mixed layer), with strong wind shear across the inversion.

Garratt

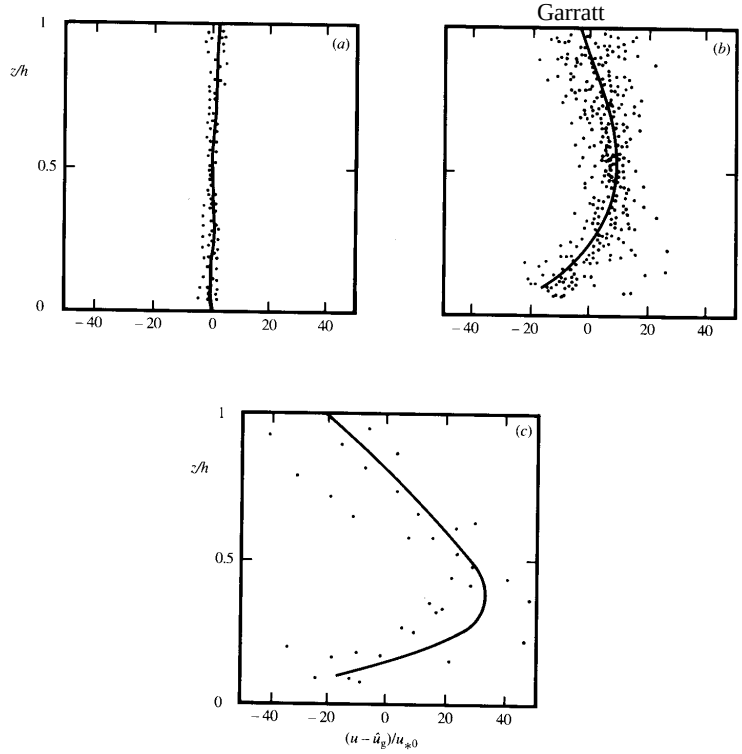

Fig. 3.13 Profiles of the normalized velocity defect for the u-component as a function of normalized height z/h, based on Eq. 3.82 and an analysis of Wangara observations. Three stability regimes are presented: (a) $-150 < h/L < -120$; (b) $0 < h < 30$; (c) $180 < h/L < 210$. Curves are drawn by eye. After Yamada (1976), *Journal of Atmospheric Sciences*, American Meteorological Society.

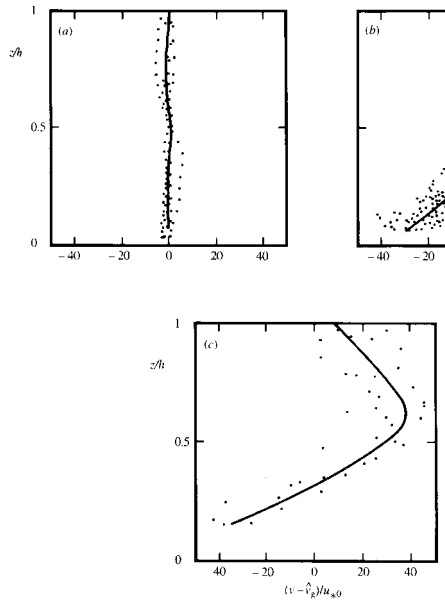

Same for v

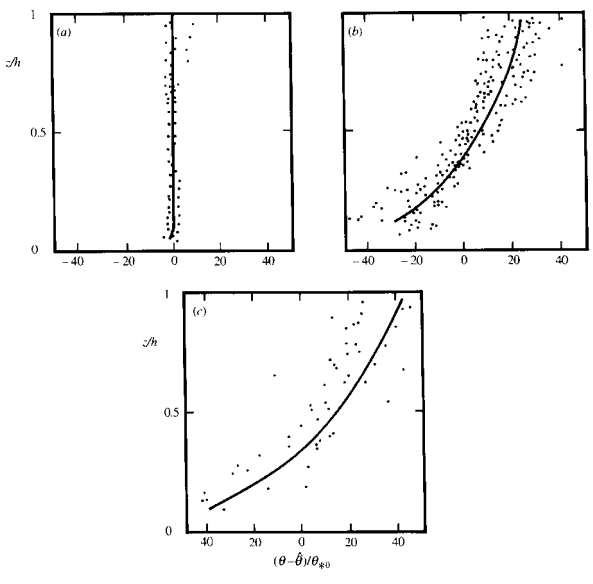

Same for θ

Sorbjan

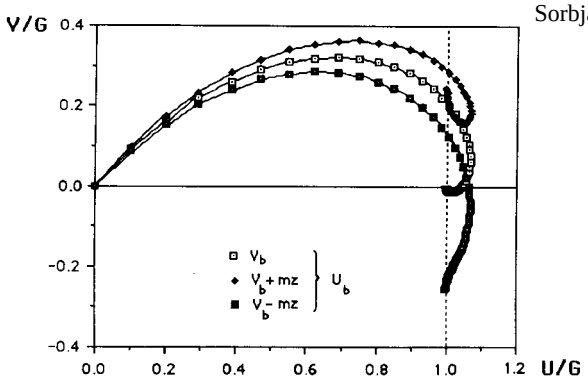

Figure 6.11 Ekman spirals obtained for the baroclinic correction of the V component of the wind velocity, $a = 0.001$, $m = 0.0001$. Points are plotted every 100 m, starting on the surface. U_b, V_b-barotropic components of the wind vector. Dotted line shows directions of the thermal wind vectors.

Ekman spirals for thermal wind with $M = 0$ and $N > 0$, $N = 0$ (no thermal wind), $N < 0$. Near-surface wind is oriented more in $+y$ direction (larger crossing angle) for $N > 0$.

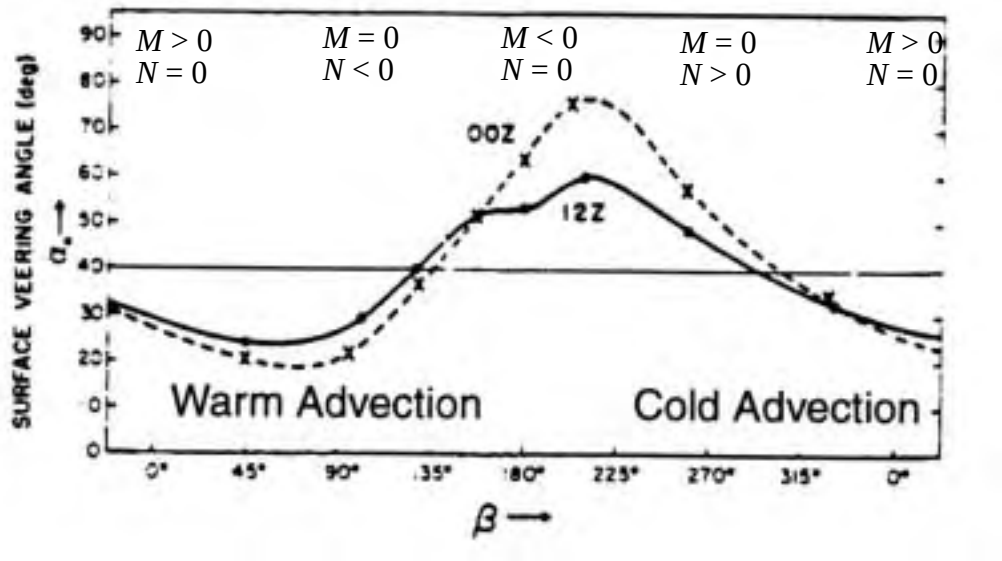

Isobaric crossing angle of surface wind vs. angle of thermal wind. Afternoon (00 Z) soundings show stronger effect due to stronger vertical mixing in a more convective BL (Hoxit 1974)

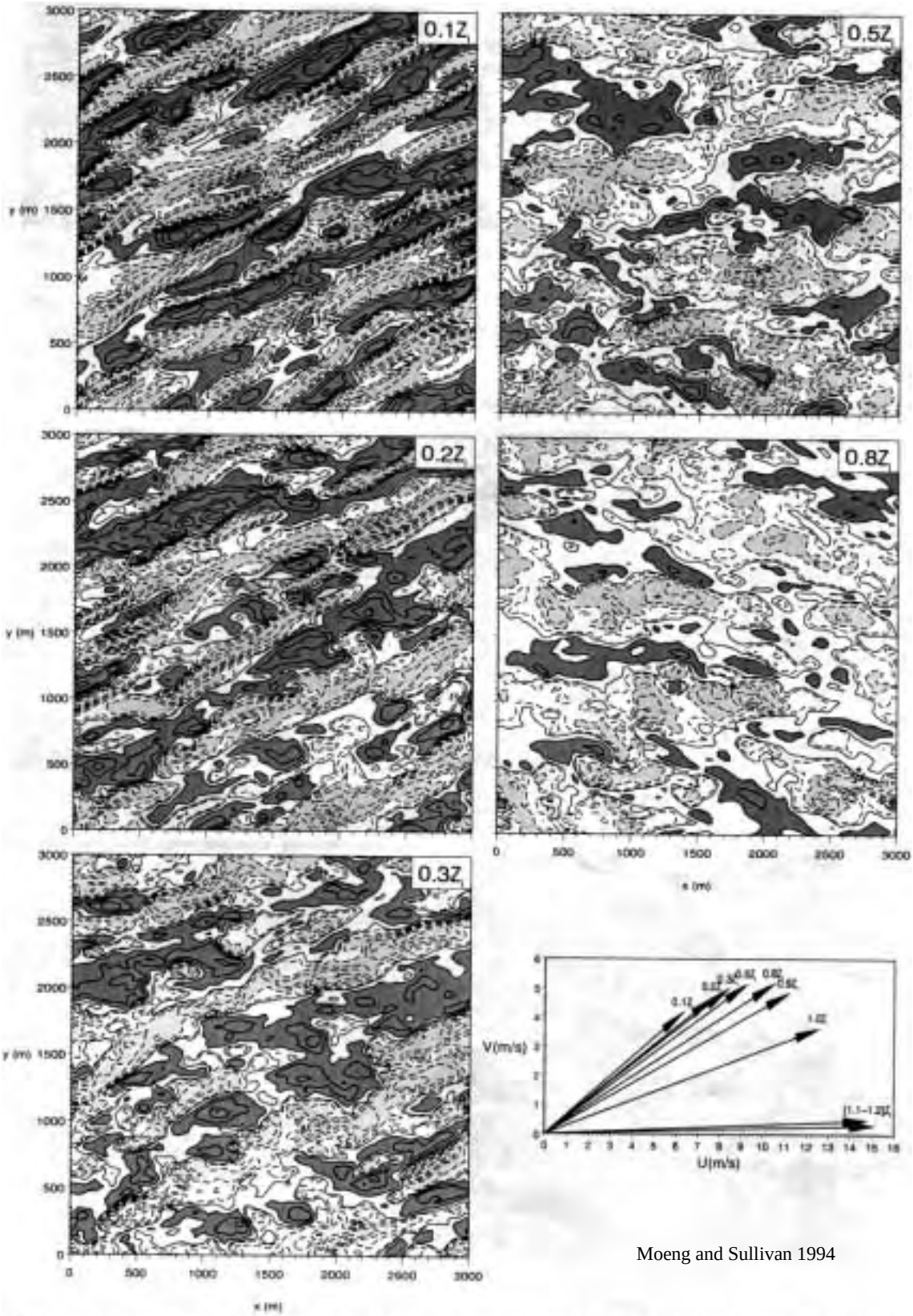

Moeng and Sullivan 1994

FIG. 3. Contours of u in the x–y plane at five height levels for simulation S and its wind hodograph: contours (-3, -2.5, -2, -1.5, -1, -0.5, -0.1, 0.1, 0.5, 1, 1.5, 2, 2.5), dark (light) shading values larger (smaller) than 0.5 (-0.5).

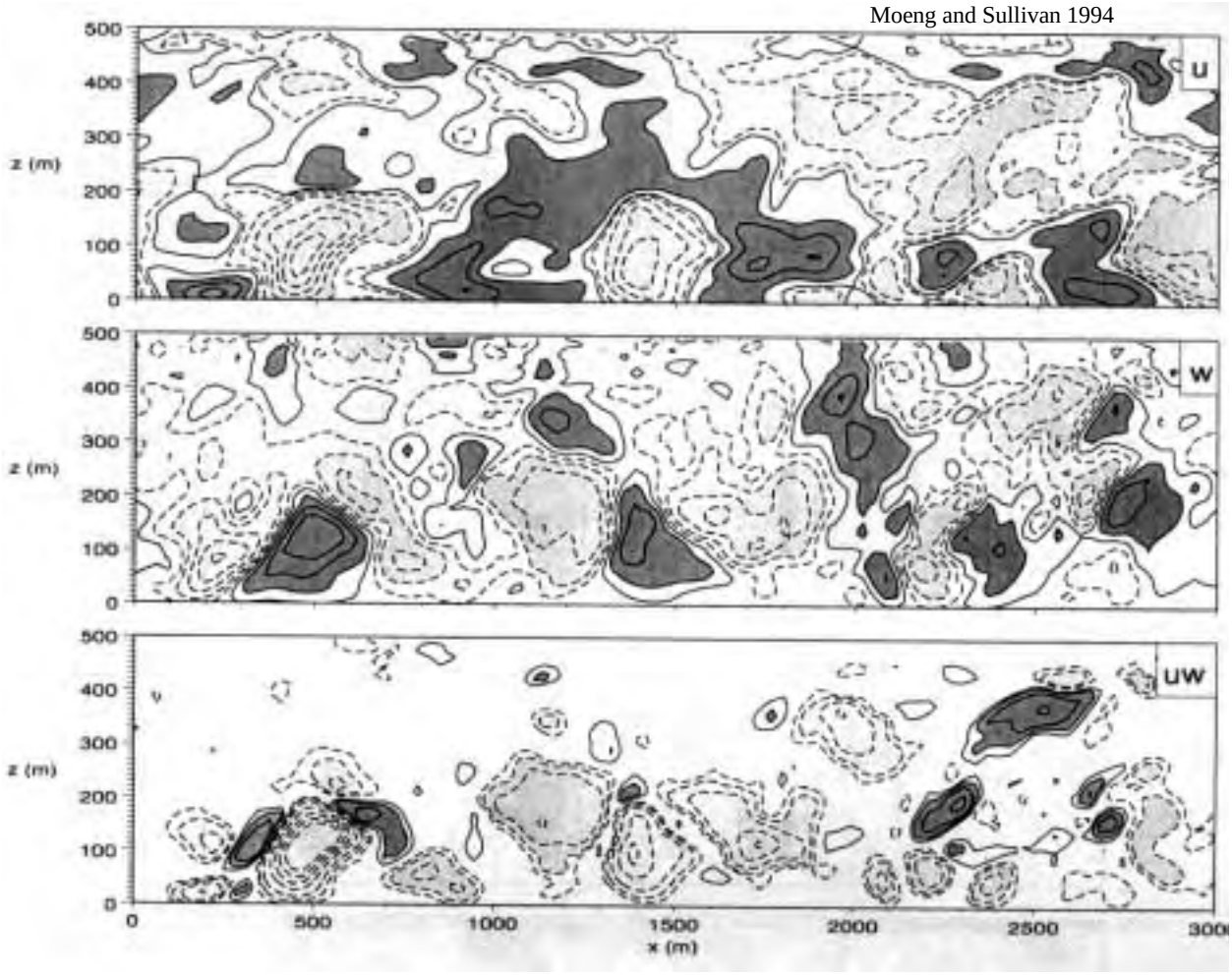

Vertical section through a neutral BL.Note strong anticorrelation between u' and w'.

We can see that at the top of the surface layer ($z/z_i = 0.1$) , u' is organized in streaks, corresponding to long cylindrical eddies or 'rolls' oriented about 20° to the left of the geostrophic wind. The wind perturbations weaken and become less linearly organized with height. The figure below shows an x-z cross section of u', w', and $u'w'$ across the center of the domain in y. Here one can see the strong negative correlation between u' and w' (updrafts have a small u than downdrafts), especially for $z/z_i < 0.5$. In fact, the correlation coefficient between u', w' is -0.4 at below this level.

The variances of the three velocity components are shown on the next page, along with their counterparts for a convective BL. For a neutral BL, they are all strongest near the ground, with the strongest perturbations in u at all levels. Their sum, divided by two, is the TKE profile. As we have discussed already, the TKE budget is essentially a balance between shear production (most of which occurs in the lowest 20% of the BL where shear and momentum fluxes are both largest) and turbulent dissipation, with little contribution from turbulent transport.

Although there is no surface buoyancy flux, the turbulence does erode the capping inversion, creating a small downward entrainment buoyancy flux $\overline{w'b'}_i$. In fact, we find that

$$\overline{w'b'}_i = -u_*^3/z_i$$

If we assume that the whole boundary layer is warmed equally by entrainment of warm air from

Moeng and Sullivan 1994

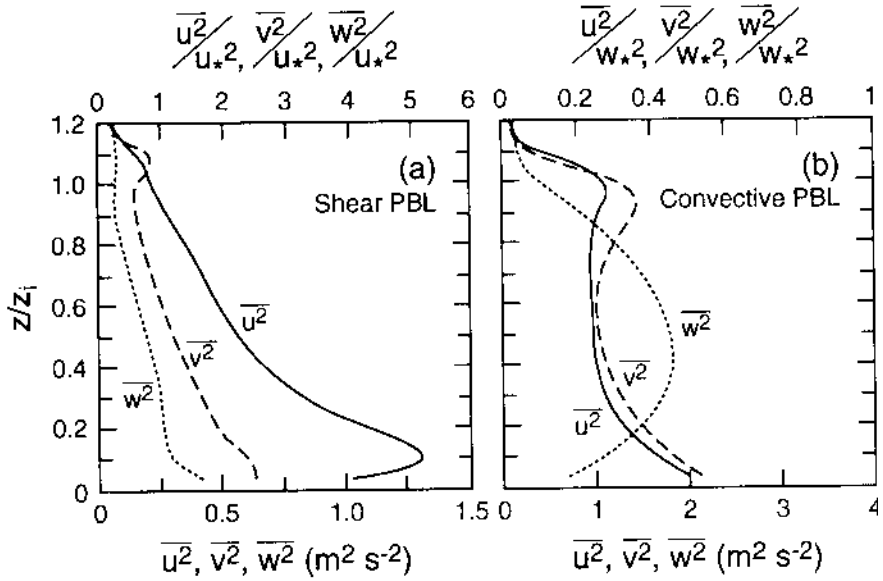

FIG. 9. Vertical distributions of the velocity variances of simulations S and B.

above the inversion, we can associate a buoyancy flux profile with the entrainment which varies linearly from 0 at $z = 0$ to $\overline{w'b'}_i$ at the inversion. The consumption rate of TKE by this buoyancy flux, vertically averaged over the BL, is $\overline{w'b'}_i/2 = -0.5u_*^3/z_i$. If we compare this to the overall dissipation rate of TKE, we find that the TKE dissipation rate is much larger than this at the surface but about $2u_*^3/z_i$ in the upper part of the BL; i. e. entrainment is consuming around 25% of the TKE generated in this region.

Weakly Unstable BLs

Moeng and Sullivan also simulated a weakly unstable boundary layer , also under a capping inversion. This was similar to their neutral case, but with a surface hear flux of 50 W m $^{-2}$, giving an Obuhkov length $L = -300$ m comparable to z_i. In this case (page 4.1.7), the streaky structure is still apparent at the lowest levels, but large convective rolls dominate the turbulence higher in the BL and help keep it well-mixed. The buoyant and shear contributions to TKE are comparable in this case. A velocity scale based on surface buoyancy flux can be derived from the TKE equation.

$$w_* = (B_0 z_i)^{1/3}$$

(Note that $z_i/L = -kw_*^3/u_*^3$); for this case $w_* = 0.9$ m s^{-1}. For the buoyancy and shear driven BL a combined velocity scale $w_m^3 = 5u_*^3 + w_*^3$ seems to work best. In particular, with any combination of surface buoyancy flux and shear, Moeng and Sullivan found that the entrainment buoyancy flux is roughly

$$\overline{w'b'}_i = -0.2\, w_m^3/z_i$$

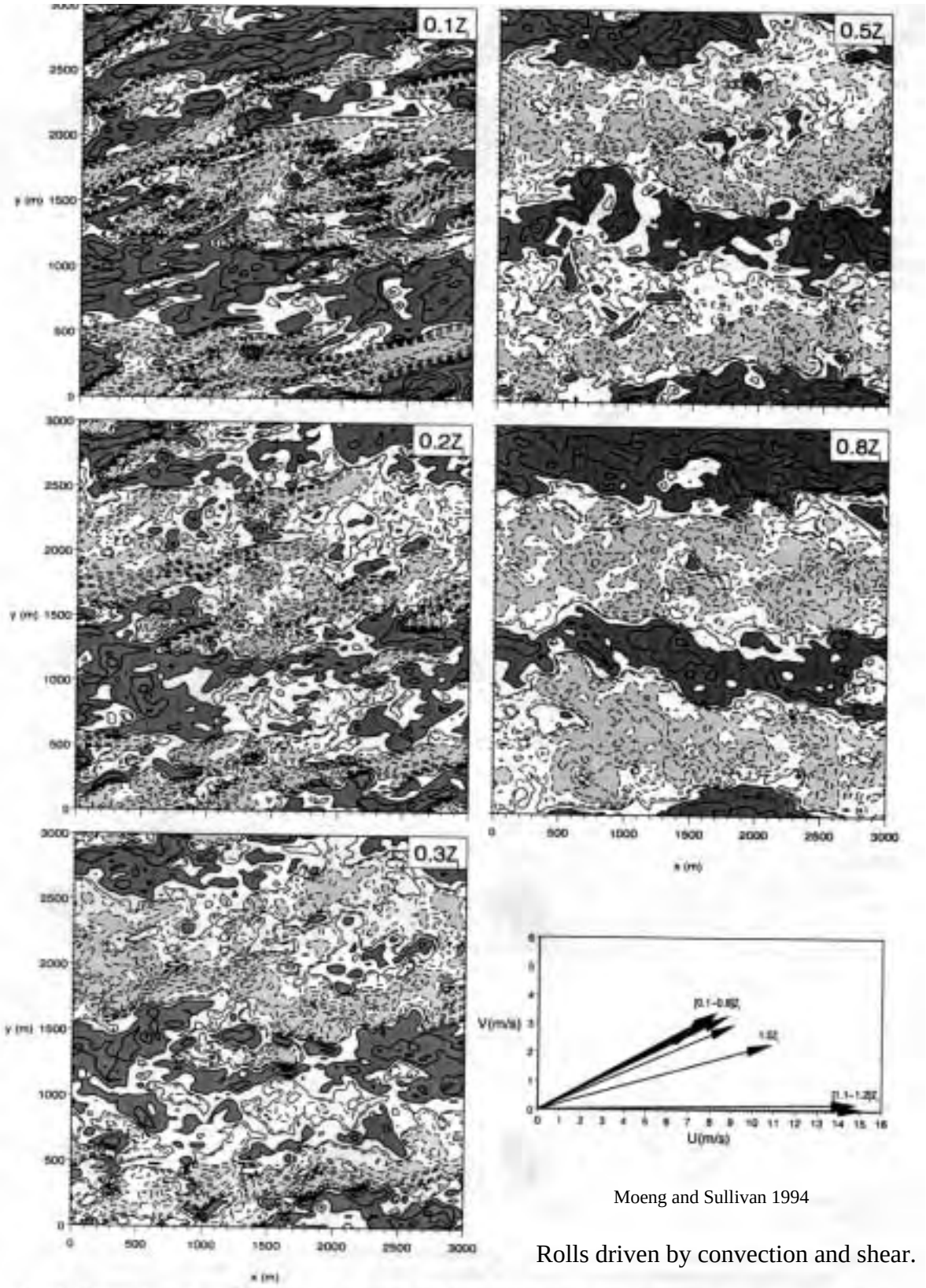

Moeng and Sullivan 1994

Rolls driven by convection and shear.

FIG. 15. Views of x–y for simulation SB1 for a field at five height levels and its wind hodograph: contours (-3, -2.5, -2, -1.5, -1, -0.5, -0.1, 0.1, 0.5, 1, 1.5, 2), dark (light) shading values larger (smaller) than 0.5 (-0.5). Some height labels in the wind hodograph are grouped since winds at those levels are about the same.

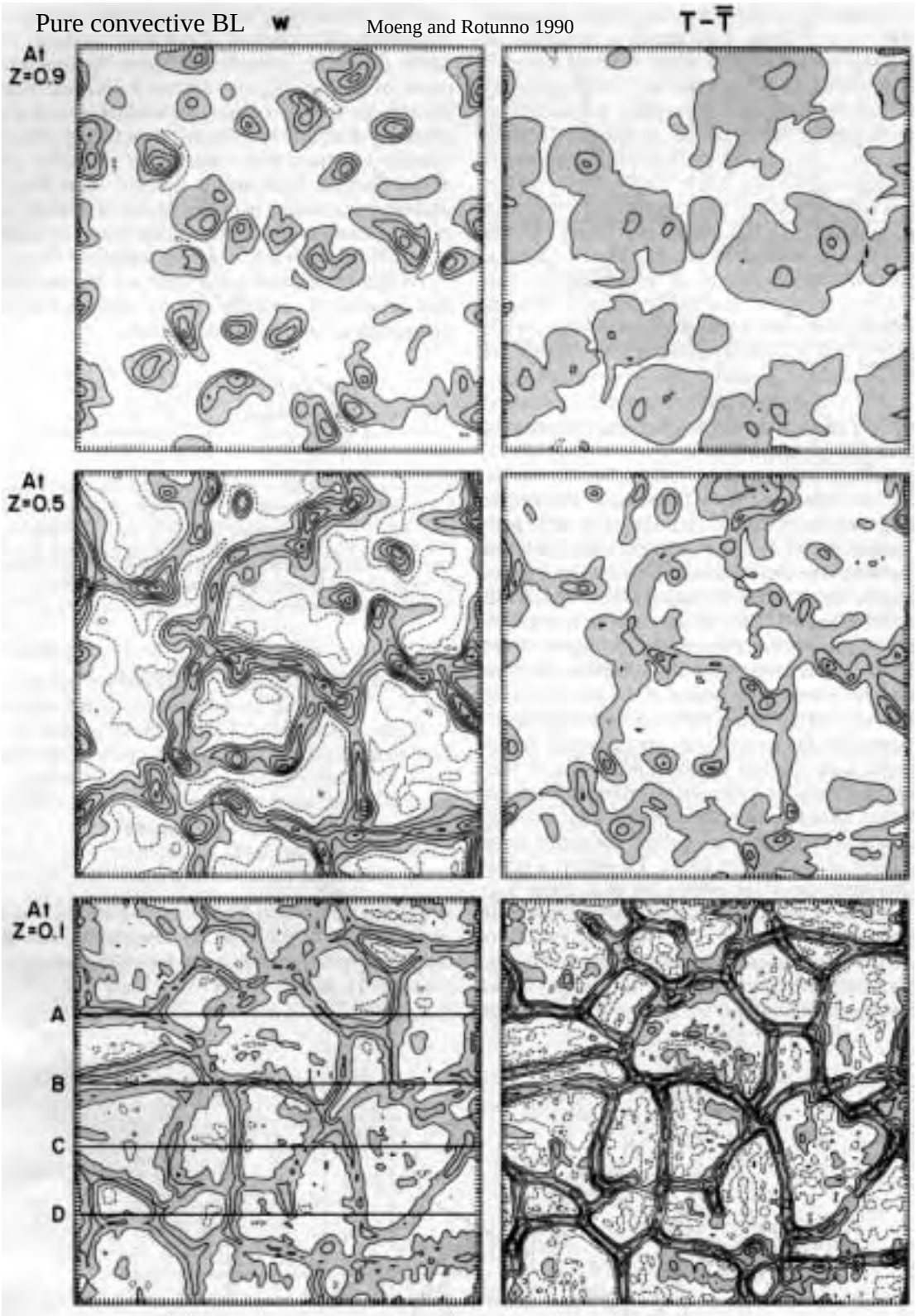

FIG. 8. As in Fig. 3, except for Experiment H. Vertical cross sections through the locations marked A, B, C and D are shown in Fig. 9.

Convective BLs

Lastly, let's look at a purely buoyancy-driven or convective BL. The simulations shown (Moeng and Rotunno 1990, *JAS*) are below a rigid boundary and do not include entrainment, but do show the overall structure well. At the bottom, there is a very good correlation between w' and θ', with polygonal regions of updraft separating circular patches of downdraft. As we move close to the BL top, the updrafts accelerate and combine to become circular, and the temperature fluctuations become much less well correlated with the updrafts. For penetrative convection, in fact the updrafts would be a bit cooler than the surrounding air at the highest level shown.

The velocity variances (previous page) show a very different structure than for a shear-driven BL. They are dominated by the large eddies, which have updrafts in the middle of the BL and predominantly lateral motions at its top and bottom. There is much more velocity variance in the upper part of the BL, so the TKE and TKE dissipation rate are almost uniform with height and equal to $0.4w_*^3/z_i$. As in the upper part of a shear-driven BL , about 25% of the TKE generated is going into consumption by entrainment, which averaged over the BL is $\overline{w'b'}_i/2 = 0.1w_*^3/z_i$. .

Below are shown LES simulations (Sullivan et al. 1998, *JAS*) of the top of a convective BL penetrating a moderate inversion of 4 K (grid resolution at top right of each plot). White indicates $\theta < 304$ K, other shades increasing θ up to 308 K. Arrows indicate velocity in the *x*-*z* plane. Plots show a sequence of times 10 s apart. Note the undulations in the BL top, with downward moving air on the edge of hummocks where updraft air has partly mixed with free-tropospheric air. These motions produce the negative buoyancy flux in the entrainment zone, which for a pure convective BL reaches $-0.2B_0$. Also note in panels e-h the formation of an 'entrainment tongue' at x = 1750 m of partly mixed, buoyant air that is getting sucked into the BL.

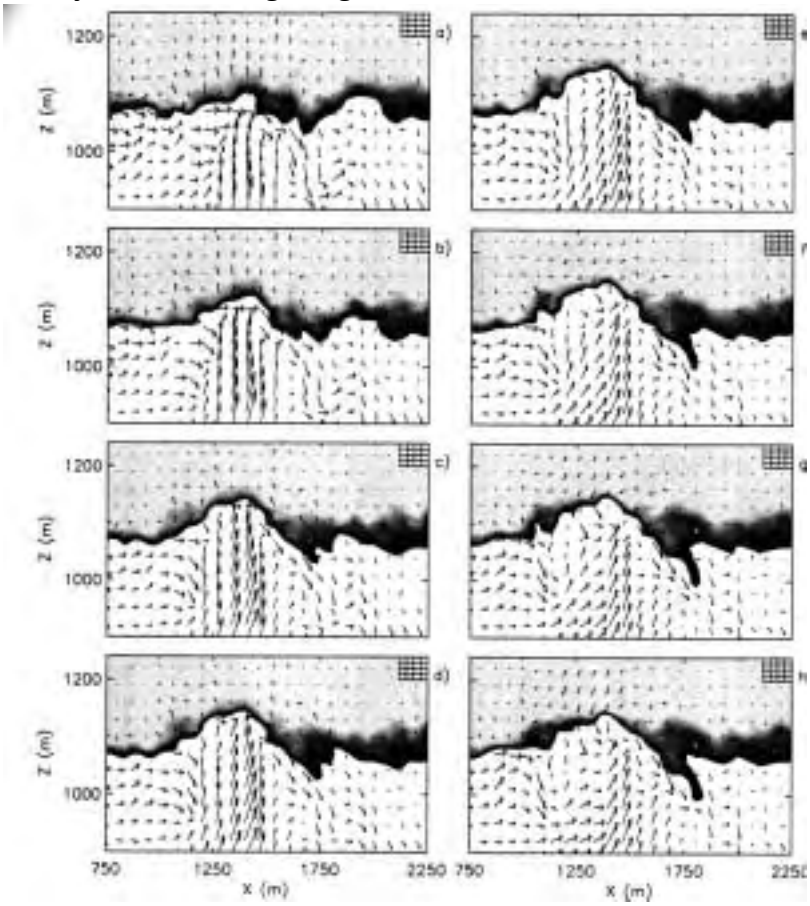

Lecture 8. Parameterization of BL Turbulence I

In the next two lectures we will summarize several approaches to parameterization of BL vertical turbulent transports that are commonly used in large-scale forecast and climate models. In such models, the horizontal grid resolution is insufficient to resolve the most energetic BL turbulent eddies, which might be tens of meters to 1-2 km across. Furthermore, while the lowest one or two model levels are usually taken to be 100 m or less from the ground to resolve stable BLs, the vertical grid spacing at a height of 1 km is typically 100-500 m, so the vertical structure of the BL can be at best coarsely resolved. Table 1 shows the distribution of thermodynamic gridpoints in the lowest 20% of the atmosphere for three representative models- the NCAR Community Climate Model version 3 (CCM3, 18 levels overall), the ECMWF operational forecast model (60 levels overall), and the MM5 mesoscale model as used for real-time forecasting in the Pacific Northwest (37 levels overall).

Three parameterization approaches are popular. In order of simplicity, they are:

1. Mixed layer models
2. 'Local' closures based on eddy diffusivity
3. 'Nonlocal' closures

Horizontal turbulent fluxes are invariably neglected as they are very small compared to advection by the mean wind. We will reserve discussion of parameterization of cloudy boundary layers for later.

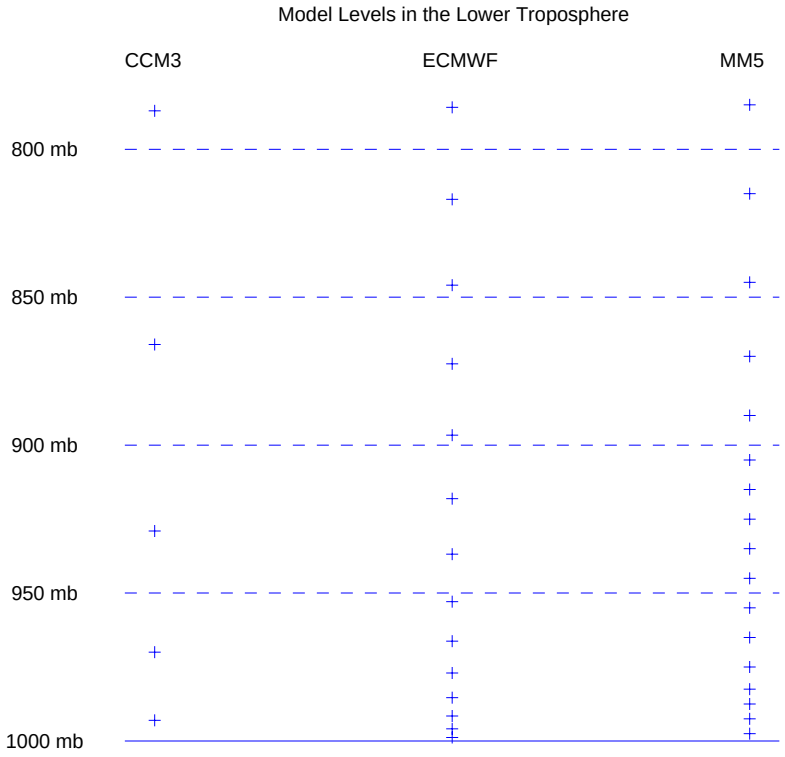

Mixed Layer Models

Mixed layer models (MLMs) assume that $\bar{u}$, $\bar{v}$, and $\bar{\theta}$ in the BL are uniform ('well-mixed'). They are most applicable to convective BLs and represent stable BLs rather poorly. However, they are relatively simple to add moist physics too, and do not require a fine vertical grid to work. They are. mainly used by researchers and teachers as a conceptual tool for understanding the impacts of different physical processes on BL turbulence. However, at least one GCM (the CSU/UCLA GCM) uses a mixed layer model to describe the properties and depth of its lowest grid layer. For simplicity, we will consider a case with no horizontal advection or mean vertical motion, no thermal wind, and no diabatic effects above the surface. We will assume that the surface momentum and buoyancy fluxes are given (in general, these will depend upon the mixed layer variables, but we needn't explicitly worry about this now). We let h be the mixed layer top, at which there may be jumps in the winds and potential temperature, denoted by Δ. Turbulence in the mixed layer entrains free-tropospheric air from just above the mixed layer, causing h to rise at the **entrainment rate** w_e.

$$\frac{\partial \bar{u}}{\partial t} - f(\bar{v} - v_g) = -\frac{\partial}{\partial z}\overline{u'w'} \tag{1}$$

$$\frac{\partial \bar{v}}{\partial t} + f(\bar{u} - u_g) = -\frac{\partial}{\partial z}\overline{v'w'} \tag{2}$$

$$\frac{\partial \bar{\theta}}{\partial t} = -\frac{\partial}{\partial z}\overline{w'\theta'} \tag{3}$$

$$\frac{\partial h}{\partial t} = w_e \tag{4}$$

Since the left hand sides of (1-3) are height-independent, the right hand sides must be, too, so the fluxes of u, v, and θ are linear with z (note that this would no longer be the case for a baroclinic BL in which $\mathbf{u}_g$ varied with height, or in the presence of internal sources or sinks of θ) .The fluxes are given at the surface. The entrainment deepening of the BL, in which free-tropospheric air with value $\bar{a} + \Delta a$ of some property a (= u, v, θ) is replaced by BL air with $a = \bar{a}$ at the rate w_e, requires a flux

$$\overline{w'a'}(h) = -w_e \Delta a$$

Thus the right hand side of the mixed layer equation for $\bar{a}$ is just.

$$-\frac{\partial}{\partial z}\overline{w'a'} = -\frac{-w_e \Delta a - \overline{w'a'}(0)}{h}$$

This closes the set of equations (1-4) except for a specification of w_e, called the **entrainment closure**. This is the big assumption in any MLM. For cloud-free unstable to nearly neutral mixed layers, formulas such as that from last time (Moeng and Sullivan 1994) are commonly used:

$$\overline{w'b'}(h) = -w_e \Delta b = -(0.2 w_*^3 + u_*^3)/h, \quad \text{where} \quad \Delta b = g \Delta\theta_v / \theta_{v0}$$

Recall that w_* and u_* are determined by the surface buoyancy and momentum fluxes, respectively, so this closure determines w_e in terms of known variables, enabling (1-4) to be integrated forward

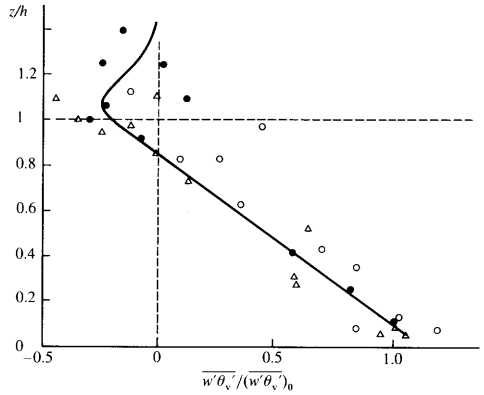

Fig. 6.2 Experimental data on the vertical variation of the virtual heat flux, normalized by its surface value; h is the depth of the mixed layer. Data are for three days from the 1983 ABL experiment; see Stull (1988, Figs. 3.1, 3.2 and 3.3). See also Fig. 6.23 of this volume.

In a convective BL, entrainment buoyancy flux is $-0{,}2B_0$

in time. This type of entrainment closure is well-supported by observational evidence and LES simulations, especially in the purely convective BL, in which the above relation reduces to

$$\overline{w'b'}(h) = -(0.2w_*^3 + u_*^3)/h = -0.2B_0$$

An observational verification of this from data taken in a daytime convective BL over land is shown above. In fact, a classic application of a MLM is to the deepening of a convective boundary layer due to surface heating; we'll look at this when we discuss the diurnal cycle of BLs over land.

Local (*Eddy diffusivity*) *parameterizations* (Garratt 8.7)

In eddy-diffusivity (often called ***K*-theory**) models, the turbulent flux of an adiabatically conserved quantity a (such as θ in the absence of saturation, but not temperature T, which decreases when an air parcel is adiabatically lifted) is related to its gradient:

$$\overline{w'a'} = -K_a \frac{d\bar{a}}{dz} \tag{5}$$

The key question is how to specify K_a in terms of known quantities. Three approaches are commonly used in mesoscale and global models:

i) **First-order closure**, in which K_a is specified from the vertical shear and static stability, or by prescribing a
ii) **1.5-order closure** or **TKE closure**, in which TKE is predicted with a prognostic energy equation, and K_a is specified using the TKE and some lengthscale.
iii) ***K*-profiles**, in which a specified profile of K_a is applied over a diagnosed turbulent layer depth.

From here on we will drop overbars except on fluxes, so $a(z)$ will refer to an ensemble or horizontal average at level z. The following discussion of theseapproaches is necessarily oversimplified; a lot of work was done in the 1970's on optimal ways to use them. An excellent review of first, 1.5, and second-order closure is in Mellor and Yamada (1982, *Rev. Geophys. Space Phys.*, **20**, 851-875)

<u>First-order closure</u>

We postulate that K_a depends on the vertical shear $s = |d\mathbf{u}/dz|$, the buoyancy frequency N^2, and an eddy mixing lengthscale l. In most models, saturation or cloud fraction is accounted for in the

computation of N^2. From the shear and stability one defines a Richardson number $\mathrm{Ri} = N^2/s^2$. Dimensionally,

$$K_a = \text{length}^2/\text{time} = l^2 s F_a(\mathrm{Ri}) \tag{6}$$

One could take the stability dependence in $F(\mathrm{Ri})$ the same as found for the surface layer in Monin-Obhukov theory, e. g. $F(\mathrm{Ri}) = [\phi_a(\zeta)\phi_m(\zeta)]^{-1}$, where ζ depends on Ri as in the surface layer, and $\phi_a = \phi_m$ (if a is momentum) or ϕ_h (if a is a scalar). This is fine in the stable BL. In the convective BL it gives (see notes p. 6.2) $F_m(\mathrm{Ri}) = (1 - 16\mathrm{Ri})^{1/2}$ and $F_m(\mathrm{Ri}) = (1 - 16\mathrm{Ri})^{3/4}$. However, in nearly unsheared convective flows, one would like to obtain a finite K_a independent of s in the limit of small s. This requires $F_a \propto (-\mathrm{Ri})^{1/2}$ so $K_a \propto l^2 s(-\mathrm{Ri})^{1/2} = l^2(-N^2)^{1/2}$. This is consistent with the M-O form for K_m but not for K_h. Thus, we just choose $K_h = K_m$ to obtain:

$$F_{h,m}(\mathrm{Ri}) = \begin{cases} (1 - 16\mathrm{Ri})^{1/2}, & \text{(unstable)} \\ (1 - 5\mathrm{Ri})^2 & \text{(stable)} \end{cases}$$

No turbulent mixing is diagnosed unless $\mathrm{Ri} < 0.2$. Every model has its own form of $F(\mathrm{Ri})$, but most are qualitatively similar to this. Usually, if this form is used within the stable BL, the F's are enhanced near the surface (no Ri = 0.2 cutoff) to account for unresolved flows and waves driven, for instance, by land-sea or hill-valley circulations that can result in spatially and temporally intermittent turbulent mixing.

Many prescriptions for l exist. The only definite constraint is that $l \to kz$ near the surface to match (6) to the eddy diffusivity in neutral conditions to that observed in a log layer, $K_a = ku_* z$. One commonly used form for l (suggested by Blackadar, 1962) is

$$l = \frac{\lambda}{1 + \lambda/kz}$$

where the 'asymptotic lengthscale' λ is chosen by the user. A typical choice is λ = 50-100 m, or roughly 10% of the boundary layer depth. The exact form of l is less important than it might appear, since typically there will be (i) layers with large K_a, and small gradients (i. e. fairly well mixed layers) in which those small gradients will just double (but still be small) if K_a, is halved, to maintain the same fluxes, (ii) layers with small K_a where physical processes other than turbulence will tend to dictate the vertical profiles of velocity and temperature, and (iii) a surface layer, in which the form of K_a is always chosen to match Monin-Obuhkov theory, and so is on solid observational ground.

<u>1.5-order closure</u>

Now we prognose the TKE $e = q^2/2$ based on the shear and stability profiles.
Using the same eddy mixing lengthscale as above, dimensionally

$$K_a = (\text{length})(\text{velocity}) = lq\, S_a(G_M, G_H), \qquad a = M \text{ (momentum) or } H \text{ (heat)}$$

$$G_M = l^2 S^2/q^2,\ G_H = -l^2 N^2/q^2$$

Closure assumptions and measurements discussed in Mellor and Yamada dictate the form of S_M and S_H in terms of the nondimensional shear and stratification G_M and G_H. These are complicated algebraic expressions, but are shown in the figure on the next page. As in first order closure, the

stability functions are larger in unstable stratification ($G_H > 0$) than in stable stratification ($G_H < 0$).

To determine the evolution of q, we use the TKE equation

$$\frac{\partial}{\partial t}\left(\frac{q^2}{2}\right) = S + B + T - \varepsilon. \tag{7}$$

We model the shear and buoyancy production terms using eddy diffusion to find the fluxes:

$$S = -\overline{u'w'}\frac{\partial \bar{u}}{\partial z} - \overline{v'w'}\frac{\partial \bar{v}}{\partial z} = lq\, S_m |d\mathbf{u}/dz|^2$$

Mellor and Yamada, 1982

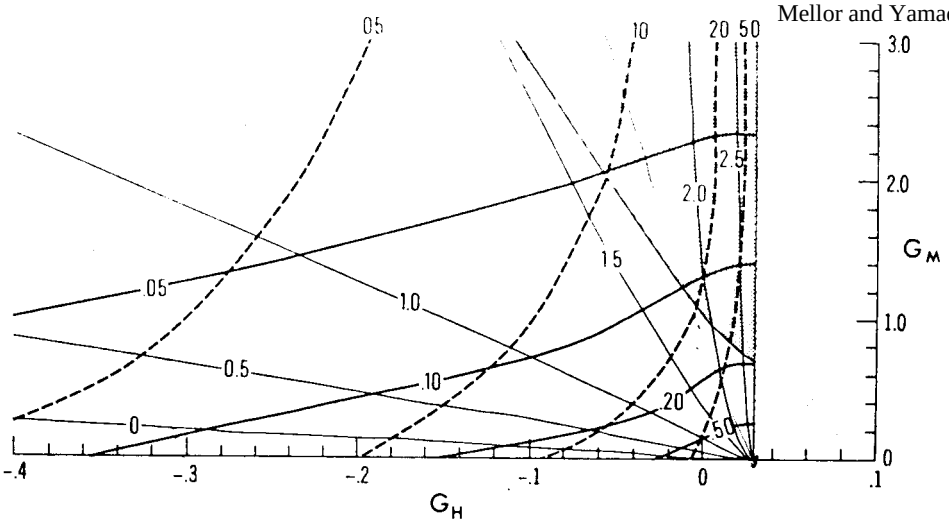

Fig. 3. The stability functions $S_M(G_H, G_M)$ and $S_H(G_H, G_M)$. The heavy solid lines are contours of S_M, whereas the dashed lines are contours of S_H. The lighter solid lines are contours of $(P_s + P_b)/\varepsilon$. One could also draw lines of constant $R_i = G_H/G_M$, which are radial lines on this diagram. The shaded portion is where $\langle w^2\rangle/q^2 \lesssim 0.12$.

Stability functions for TKE closure.

$$B = \overline{w'b'} = -lq\, S_h N^2$$

We model the transport term by neglecting pressure correlations and using eddy diffusion to model the flux of TKE:

$$\overline{w'p'} \approx 0$$

$$\overline{w'e'} = -K_q \frac{\partial}{\partial z}\left(\frac{q^2}{2}\right) = -lqS_q \frac{\partial}{\partial z}\left(\frac{q^2}{2}\right) \quad (S_q \text{ is often taken to be } 0.2)$$

$$T = -\frac{\partial}{\partial z}\left(\overline{w'e'} + \frac{1}{\rho_0}\overline{w'p'}\right) = \frac{\partial}{\partial z}\left(lqS_q \frac{\partial}{\partial z}\left(\frac{q^2}{2}\right)\right)$$

Lastly, the dissipation term is modelled in terms of characteristic turbulent velocity and length-scales. While the lengthscale in ε is related to the master lengthscale, it is necessary to intoduce a scaling factor to get the TKE to have the right magnitude:

$$\varepsilon = q^3/(lB_1),, \; B_1 \approx 15.$$

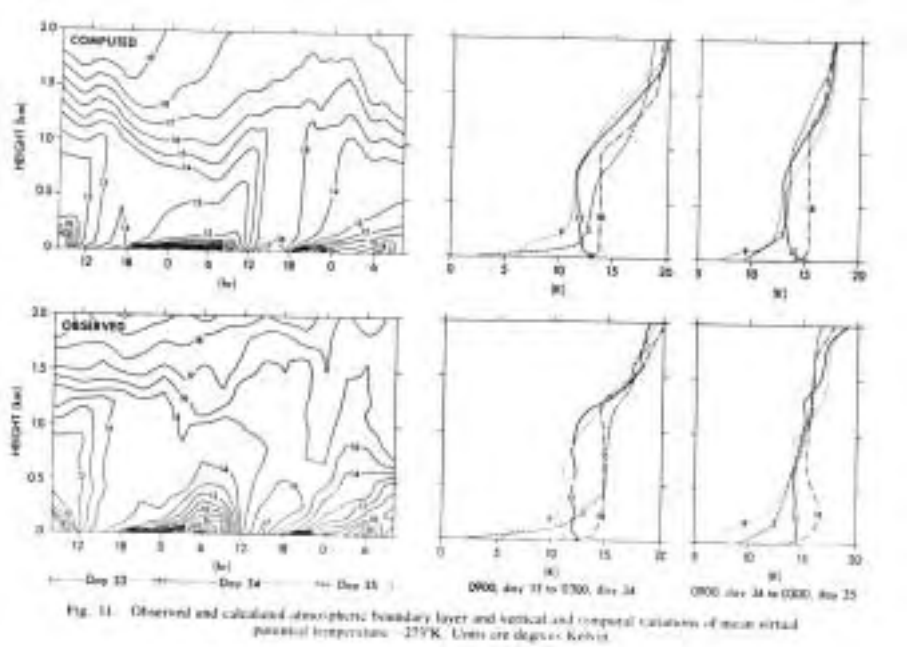

Fig. 11. Observed and calculated atmospheric boundary layer and vertical and temporal variations of mean virtual potential temperature −275°K. Units are degrees Kelvin.

Virtual temperature evolution observed during two days of the Wangara expt. (top) and modelled with a TKE closure (bottom)

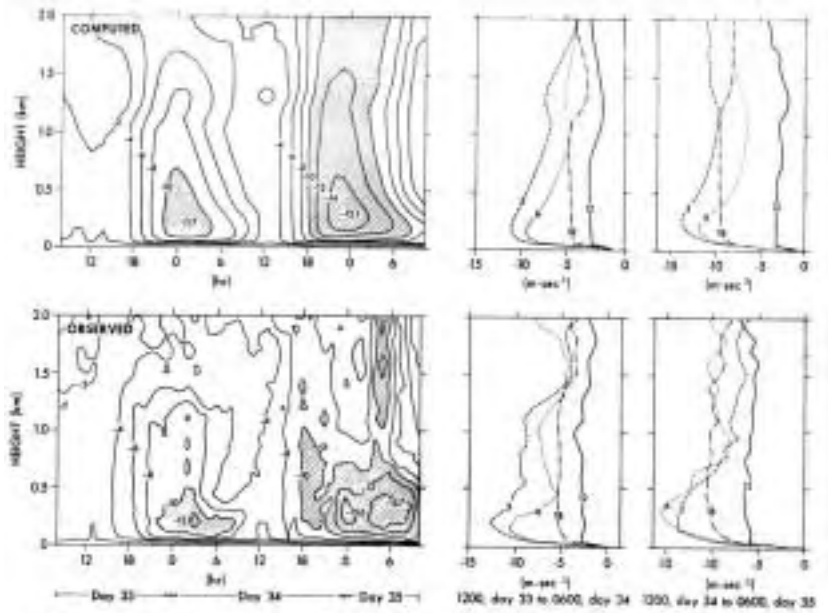

Fig. 12. Observed and calculated atmospheric boundary layer and vertical and temporal variations of the eastward mean wind component. Units are meters per second.

Same for *u* velocity.

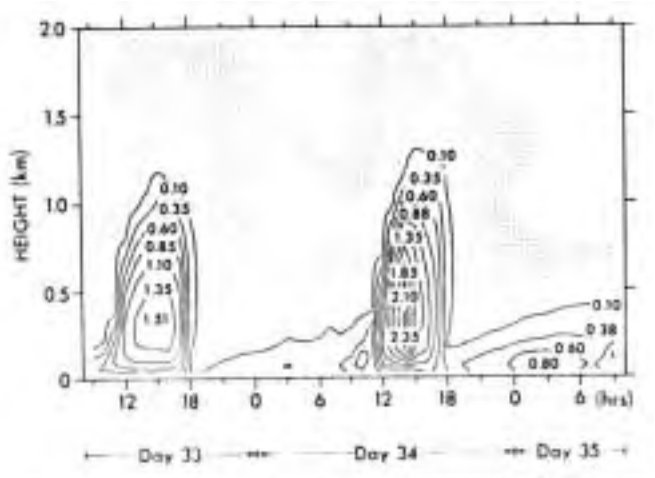

Fig. 14. Time and space variation of computed q^2 (twice the turbulent kinetic energy); units are square meters per second. The stippled areas indicate regions where $10^{-1} < q^2 < 10^{-2}$ m^2 s^{-1}

Modelled TKE profile for simulation on previous page

With these forms for all the terms in the TKE equation, it can now be integrated forward in time. The basic improvement in using TKE vs. 1st order closure is that there is TKE 'transport' (through eddy diffusion) and storage. In the surface layer, where storage and transport are negligible compared to local shear and buoyancy production of TKE, the latter must balance dissipation, and, one finds that $\varepsilon = S + B$, so

$$q^3/(lB_1) = lq\, S_m|d\mathbf{u}/dz|^2 - lq\, S_h N^2$$

$$q^2 = B_1 l^2\{S_m|d\mathbf{u}/dz|^2 - S_h N^2\}$$

Hence, q can be eliminated in place of the local shear and stratification, and we recover the first order closure method. In the S_H-S_M figure, the thin line $(P_S+P_B)/\varepsilon = 1$ corresponds to this case.

<u>*K*-profile methods</u>

For specific types of boundary layer, one can use measurements and numerical experiments to specify a profile of eddy diffusivity which matches the observed fluxes and gradients. This can be particularly useful in situations such as stable nocturnal BLs which can be difficult for other methods. Such methods require a diagnosis of BL height h, then specify a profile of K. For instance , Brost and Wyngaard (1978) combined theoretical ideas and observational analysis to proposed the following profile for stable BLs:

$$K_m = ku_* hP(z)/(1 + 5z/L),\ \ P(z) = (z/h)(1 - z/h)^{3/2}$$

This method is designed to approach the correct form $ku_* z/\phi_m(z/L)$ in the surface layer, where $z/h << 1$. Similar approaches are have been used for convective BLs. Advantages of the *K*-profile method are that it is computationally simple and works well even with a coarsely resolved BL, as long as the BL height h can be diagnosed fairly well. On the other hand, it is tuned to specific types of BL,and may work poorly if applied more generally than the situations for which it was tuned.

Comments on local closure schemes

First-order closure is most appropriate for neutral to weakly stable BLs in which little transport of TKE is occuring and the size of the most energetic eddies is a small fraction of the BL depth. In this case, it is reasonable to hope that the local TKE will be dependent on the local shear and stability, and that since the eddies are small, they can be well repressented as a form of diffusion. However, it works tolerably well in convective boundary layers as well, except near the entrainment zone. In an entrainment zone, Transport of TKE into the entrainment zone is required to sustain any turbulence there. Since this is ignored in 1st order closure, there is no way for such a model to deepen by entrainment through an overlying stable layer, as is observed. BL layer growth must instead be by encroachment, i. e. the incorporation of air above the BL which has a buoyancy lower than that within the BL. This does allow a surface-heated convective boundary layer to deepen in a not too unreasonable manner, but creates severe problems for cloud-topped boundary layer modeling. Almost all large-scale models (e. g. CCM3, ECMWF, and MM5) include a first-order closure scheme to handle turbulence that develops above the BL (due to Kelvin-Helmholtz instability or elevated convection, for instance).

1.5-order closure is also widely used, especially in mesoscale models where the timestep is short enough not to present numerical stability issues for the prognostic TKE equation. The Mellor-Yamada and Gayno-Seaman PBL schemes for MM5 are 1.5 order schemes that include the effect of saturation on N^2. The Burk-Thompson scheme for MM5 is a 1.5 order scheme with additional prognostic variables for scalar variances ('Mellor-Yamada Level 3'). The TKE equation in 1.5-order closure allows for some diffusive transport of TKE. This creates a more uniform diffusivity throughout the convective layer, and does permit some entrainment to occur.Quite realistic simulations of the observed diurnal variation of boundary layer temperature and winds have been obtained using this method (see figures on next page). However, getting realistic entrainment rates for clear and cloud-topped convective BLs with this approach requires considerable witchcraft. The BL top tends to get locked to a fixed grid level if there is a significant capping inversion and vertical grid spacing of more than 100 m or so. TKE closure has also proved successful for cloud-topped boundary layers, but again only with grid spacings smaller than is currently feasible for GCMs. Grenier and Bretherton (2001, *MWR*, **129**, 357-377) showed that this method works well for convective BLs even at coarse resolution when combined with an explicit entrainment parameterization at the BL top, implemented as an effective diffusivity.

K-profile methods are widely used in GCM BL parameterizations (e.g. CCM3). For convective boundary layers, a nonlocal contribution is usually also added to the fluxes (see below).

Nonlocal closure schemes

Any eddy diffusivity approach will not be entirely accurate if most of the turbulent fluxes are carried by organized eddies filling the entire boundary layer (such as boundary layer rolls or convection). Consequently, a variety of 'nonlocal' schemes which explicitly model the effects of these boundary layer filling eddies in some way have been proposed. A difficulty with this approach is that the structure of the turbulence depends on the BL stability, baroclinicity, history, moist processes, etc., and no nonlocal parameterization proposed to date has comprehensively addressed the effects of all these processes on the large-eddy structure. Nonlocal schemes are most attractive when the vertical structure and turbulent transports in a specific type of boundary layer (i. e. neutral or convective) must be known to high accuracy. For instance, successful applications include the detailed thermal structure (i. e. deviation from neutral static stability) within a convective boundary layer, or the velocity structure and relation of near-surface wind to geostrophic wind within a

near-neutral boundary layer (this is the motivation for the PBL model developed here at UW by Bob Brown's group).

Lecture 5.1 Nonlocal Parameterizations for Unsaturated BLs

In this lecture, we describe three nonlocal parameterizations for unsaturated BLs:

1. Holtslag-Boville scheme (used in CCM3)
2. Blackadar scheme (MM5)
3. UW PBL scheme (used by Bob Brown's group for using satellite microwave scatterometer measurements of surface wind to determine geostrophic wind.)

We describe 1 and 2 in the notes; 3 will be discussed by guest-lecturer Dr. Ralph Foster.

Holtslag-Boville Scheme

References:

Troen,, I., and L. Mahrt, 1986: A simple model of the atmospheric boundary layer: Sensitivity to surface evaporation. *Bound.-Layer Meteor.*, **37**, 129-148.

Holtslag, A. A. M., and C.-H. Moeng, 1991: Eddy diffusivity and countergradient transport in the convective atmospheric boundary layer . *J. Atmos. Sci.*, **48**, 1690-1698.

Holtslag, A. A. M., and B. A. Boville, 1993: Local versus nonlocal boundary layer diffusion in a global climate model. *J. Climate*, **6**, 1825-1842.

Holtslag and Moeng (1991, *JAS*) examined the prognostic equation for an advected scalar a in a surface-heated convective BL. By modeling the individual terms, they concluded that

$$\overline{w'a'} = -K_a\left(\frac{\partial a}{\partial z} - \gamma_a\right) \quad 0 < z < h$$

The second term on the right, which can be interpreted as a nonlocal flux of a, is due to boundary-layer filling convective eddies which transport the surface flux of a upward regardless of the local gradient of a. Assuming the surface flux of a is positive, the result of the nonlocal term is to produce a BL with in which a decreases less with height than if pure first-order closure were used.

$K_a = kw_t z(1 - z/h)^2$, $k = 0.4$ is von Karman constant

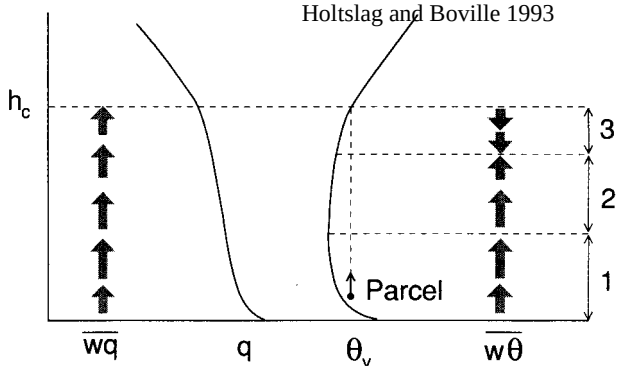

FIG. 2. Typical vertical profiles for (virtual) potential temperature Θ_v and specific humidity q for a dry convective boundary layer [modified after Stull (1991)]. The arrows to the left illustrate the specific humidity flux $\overline{wq}$, and the arrows to the right, the heat flux $w\theta$. Also, an uprising parcel is indicated up to its intersection height h_c. The three regions are discussed in the text.

$$\gamma_a = A\frac{w_*(\overline{w'a'})_0}{w_t^2 h}, \quad A = 7.2$$

$$w_t = \Pr\{u_*^3 + c_1 w_*^3\}, \; c_1 = 0.6, \Pr = 1 \text{ (momenta)}, 0.6\text{ -}1 \text{ (scalars)}$$

$$h = \frac{Ri_{cr}[u(h)^2 + v(h)^2]}{\frac{g}{\theta_s}(\theta_v(h) - \theta_s)}, \; \mathrm{Ri}_{cr} = 0.5 \text{ (optimal value depends on model } \Delta z)$$

The nonlocal flux is largest near the center of the boundary layer, with a maximum value

$$\overline{w'a'}_{\text{nonlocal, max}} = K_{a,\max}\gamma_a = 0.43(w_*/w_t)\overline{w'a'}_0 \text{ at } z = h/3$$

Since the nonlocal flux is proportional to w_*/w_t, it is only active in unstable boundary layers where the convective velocity w_* is significant. In stable or neutral BLs, the parameterization reduces to a *K*-profile eddy diffusivity.

The surface fluxes are computed using an approximation to Monin-Obuhkov theory. In a coarsely resolved model, the actual gradient of a as a function of z is not explicitly computed, so bulk aerodynamic formulas due to Louis (1979, *Bound.-Layer Meteor.*), which are based only on the difference between the surface value a_0 and its value a_0 at the lowest gridpoint at height z_1, are used. The transfer coefficient for a scalar a, given roughness length z_0, is of the standard form

$$C_a = C_N F(\mathrm{Ri}_0), \quad \text{where } C_N = k^2/\ln^2(z_1/z_0)^2 \text{ is standard neutral transfer coeff.}$$

$$\mathrm{Ri}_0 = z_1(b_1 - b_0)/|\mathbf{u}_1|^2, \quad \text{where } b_i = g(\theta_{vi} - \theta_R)/\theta_R \text{ is mean buoyancy at level } i.$$

$$F(\mathrm{Ri}_0) = \begin{cases} 1 - \dfrac{15\mathrm{Ri}_0}{75C_N(\mathrm{Ri}_0 z_1/z_0)^{1/2}}, & \text{unstable } (\mathrm{Ri}_0 < 0) \\ \dfrac{1}{1 + 10\mathrm{Ri}_0(1 + 8\mathrm{Ri}_0)}, & \text{stable } (\mathrm{Ri}_0 > 0) \end{cases}$$

Note that $F(\mathrm{Ri}_0)$ is always positive regardless of how large Ri_0 is. This is because even if Ri_0 is too large to support steady turbulence at height z_1, there will be turbulence and turbulent fluxes closer to the ground which should modify the lowest model layer.

The nonlocal closure tends to produce a warmer, deeper convective BL than first-order closure. This is often a step in the right direction, but can be misleading for cloud-topped boundary layers where the estimated BL depth can be too deep.

Holtslag and Boville 1993

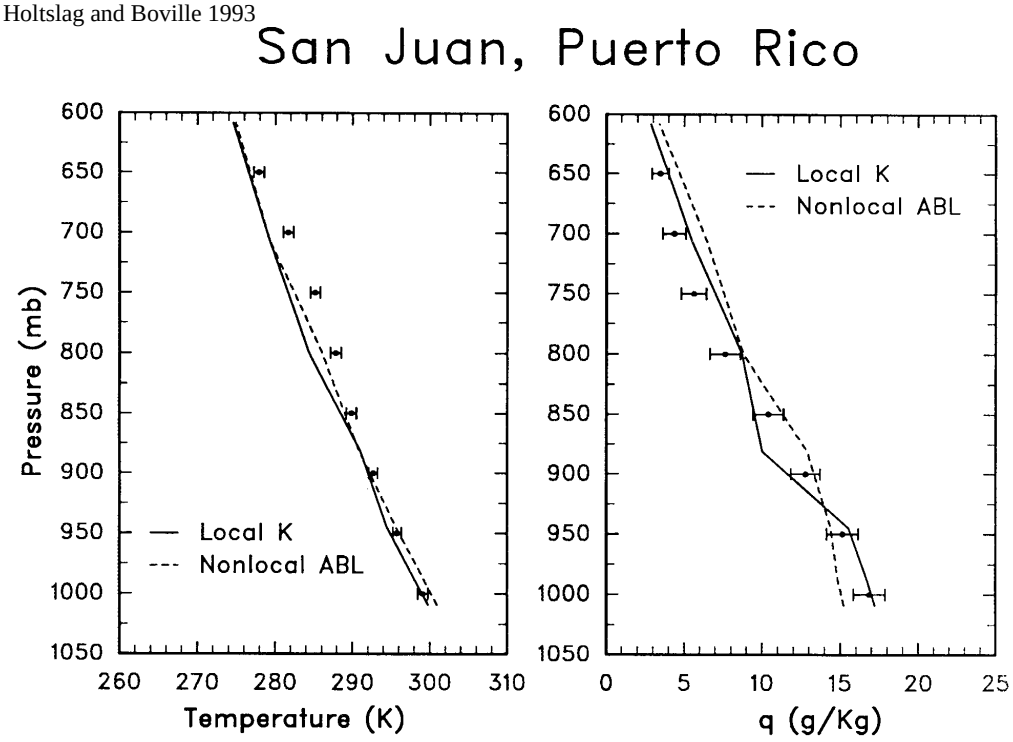

FIG. 3. As Fig. 1 but for San Juan, Puerto Rico (18.3°N, 66°W).

Comparison of CCM3 with local (solid) and nonlocal (dashed) closures with July climatology for San Juan, Puerto Rico (a trade-cumulus regime)

Blackadar convective BL (from Grell et al. 1994)

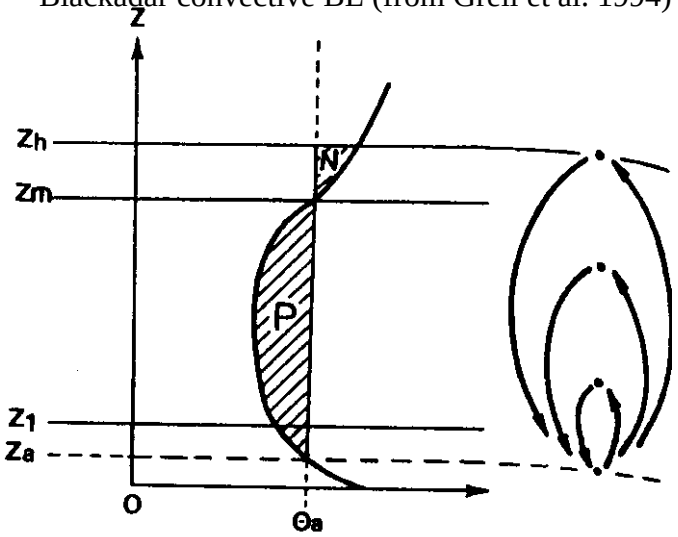

FIG. 2. Schematic diagram illustrating free convective module. Plumes originating at level z_a rise and mix at various levels, exchanging heat, moisture and momentum with air at these levels. Some thermals overshoot the level z_m of zero buoyancy. The ratio of negative area N on the thermodynamic diagram to the positive area P is the entrainment rate (see text).

Blackadar high-resolution PBL scheme

References

Blackadar, A. K., 1979:*Advances in Environmental Science and Engineering*, **1**, No. 1, Pfafflin and Ziegler, Eds., Gordon and Breach Publishers, 50-85.

Zhang, D.-L., and R. A. Anthes, 1982: A high-resolution motdel of the planetary boundary layer- sensitivity tests and comparisons with SESAME-79 data. *J. Appl. Meteor,* **21**, 1594-1609.

Grell, G. A., J. Dudhia, and D. R. Stauffer, 1994: *A Description of the Fifth-Generation Penn State/NCAR Mesoscale Model (MM5)*. NCAR Tech. Note NCAR/TN-398, pp. 91-97.

Like the Holtslag-Boville scheme, the Blackadar scheme distinguishes between stable and unstable BLs. For stable BLs, conventional first-order closure is used. Turbulence is reduced to weak 'background' values if $Ri_0 > 0.2$. Numerically efficient approximations to the M-O relations are used in the stable to neutral regime in which $h/L > -1.5$, where h is a diagnosed BL height.

For unstable BLs, a nonlocal scheme is used. It is based on conceptual models and observations of BL convection. The lowest model thermodynamic level is assumed to represent the surface layer and is labeled by subscript a. Vertical exchange is visualized as the result of plumes originating in the surface layer mixing with air at each level below h. The BL depth h is taken to be the maximum penetration height of undilute plumes. They are assumed to accelerate due to their buoyancy until they reach their level of neutral buoyancy z_{nb}. At this point their upward kinetic energy $w_p^2/2 \propto P$, where P is their vertically integrated buoyancy perturbation. Due to their inertia, the plumes overshoot, topping out at a level h at which their vertically integrated buoyancy deficit $N = -0.2P$ (see figure above). This defines the BL top:

$$\frac{N}{P} = \frac{-\int_{z_{nb}}^{h} b_p(z)dz}{\int_0^{z_{nb}} b_p(z)dz} = 0.2 \quad \text{at } z = h, \quad \text{where } b_p(z) = g(\theta_{va} - \theta_v(z))/\theta_R$$

The (unstable) stratification of the lowest model layer above the surface layer is assumed to be related to the sensible heat flux through this layer, following observations of Priestley (1956):

$$\overline{w'\theta_v'}_1 = B(\theta_{va} - \theta_{v,3/2})^{3/2}$$

where B is a coefficient that depends only on the heights of the first two model levels. In the surface layer,

$$\frac{\partial \theta_a}{\partial t} = -\frac{(\overline{w'\theta_v'}_1 - \overline{w'\theta_v'}_0)}{z_1}$$

These equations will reach an equilibrium in which θ_{va} is larger than $\theta_{v,3/2}$ by an amount sufficient to carry the surface heat flux out of the surface layer into the rest of the BL.

The scheme now postulates a mass exchange $\overline{m}$ between the surface layer and each other layer below $z = h$:

$$\bar{m} = \overline{w'b'}_1 / 0.64P, \text{ where the buoyancy flux } \overline{w'b'}_1 = \frac{g}{\theta_R}\overline{w'\theta_v'}_1$$

The value of a scalar such as θ in the BL is now assumed to change due to turbulent exchange with the surface layer according to

$$\frac{\partial \theta}{\partial t} = \bar{m}(\theta_a - \theta)$$

For momenta, $\bar{m}$ is multiplied by a factor 1 - *z/h* to account for the fact the momentum mixing is somewhat less efficient than mixing of scalars in a convective BL.

Comparisons of this parameterization with LES results have not been presented, and two case studies presented by Zhang and Anthes (1982) show fair, but not excellent agreement with observed BL evolution over land. Thus, the convective, nonlocal part of this scheme should probably be regarded as being on a shakier footing than the Holtslag-Boville scheme. It is not entirely clear that either of these schemes is superior to first order closure in practice.

Lecture 10. Surface Energy Balance (Garratt 5.1-5.2)

The balance of energy at the earth's surface is inextricably linked to the overlying atmospheric boundary layer. In this lecture, we consider the energy budget of different kinds of surfaces. Consider first an ideal surface, which is a very thin interface between the air and an underlying solid or liquid medium that is opaque to radiation. Because it is thin, this surface has negligible heat capacity, and conservation of energy at the surface requires that

$$R_N = H_S + H_L + H_G.$$

where (note sign conventions)

H_S (often just called H) is the upward surface sensible heat flux

$H_L = LE$ is the upward surface latent heat flux due to evaporation at rate E

H_G is the downward ground heat flux into the subsurface medium.

R_N is the net downward radiative flux (longwave + shortwave).

The ratio $B = H_L/H_S$ is called the **Bowen ratio**. $L = 2.5\times10^6$ J kg^{-1} is the latent heat of vaporization. Over land, there is a large diurnal variation in the surface energy budget (see schematic below). Over large bodies of water, the large heat capacity of the medium and the absorption of solar radiation over a large depth combine to reduce the near-surface diurnal temperature variability, so H_S and H_L vary much less. However, the surface 'skin temperature' of a tropical ocean can vary diurnally by up to 3 K in sunny, light-wind conditions.

An ideal surface is not usually encountered. Real surfaces may include a plant canopy or other features such as buildings not opaque to radiation and with a significant heat capacity. In this case, it is more appropriate to define an interfacial layer which includes such features. We let $W(t)$ be the energy stored within this layer per unit horizontal area. The revised layer energy budget is:

$$R_N = H_S + H_L + H_G + dW/dt.$$

We could also consider the energy budget of control volumes with finite horizontal extent (e. g. a parking lot, city, or larger geographic region). In this case horizontal transfer of energy may also be important; we won't consider this complication here.

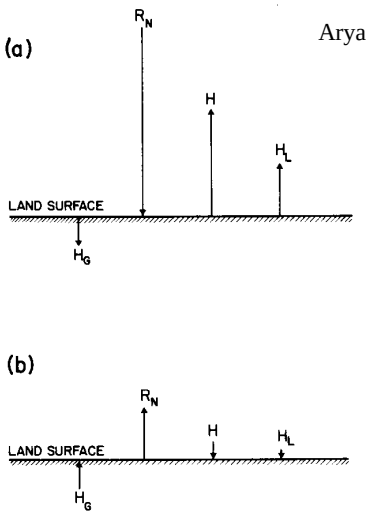

Fig. 2.1 Schematic representation of typical surface energy budgets during (a) daytime and (b) nighttime.

Arya

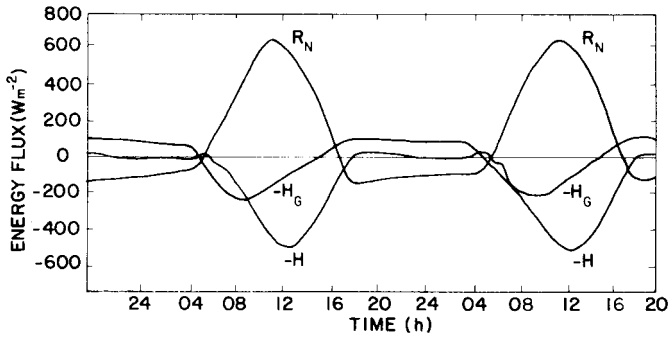

Fig. 2.3 Observed diurnal energy balance over a dry lake bed at El Mirage, California, on June 10 and 11, 1950. [After Vehrencamp (1953).]

Examples

The energy budget measured over a dry desert lake bed is shown above. In this case, latent heat fluxes are negligible. During the day, copious solar radiation is absorbed at the surface, and the ground heats up rapidly. Initially, most of the heat is conducted down into the soil, but as the layer of warmed soil thickens, H_S dominates; the heat is primarily transferred to the air. This is promoted by extreme differences (up to 28 K) between the ground temperature and the 2 m air temperature. At night, surface radiative cooling is balanced by an upward ground heat flux. Since the nocturnal boundary layer is very stable, the turbulent heat flux H_S is negligible.

The energy budget of a barley field is shown below. During the daytime, radiative heating of the surface is balanced mainly by latent heat flux due to **evapotranspiration**, i. e. evaporation from the soil surface and transpiration by the plant leaves. In the lingo, the Bowen ratio is small, -0.3 to 0.3. H_L can be so large that the surface gets cooler than the air during early morning and late afternoon and the heat flux is downward. For a field, heat storage is usually negligible. At night, all terms become much smaller; as before, radiative cooling is mainly balanced by ground heat flux..

Arya

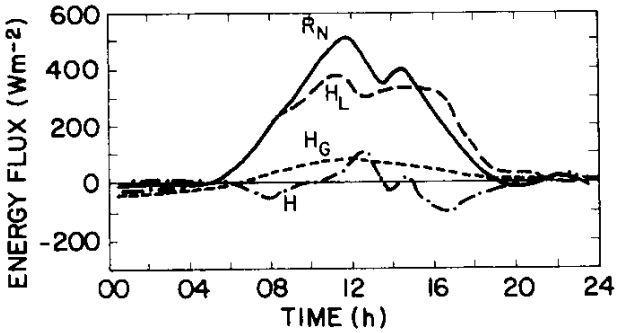

Fig. 2.4 Observed diurnal energy budget of a barley field at Rothamsted, England, on July 23, 1963. [From Oke (1987); after Long *et al.* (1964).]

The last example is a Douglas fir forest (next page). Here latent and sensible heat fluxes are comparable during the day. The storage and ground heat flux are lumped in the curves, but for deep forest, the storage term dominates. At night, release of heat from the tree canopy and condensation (dew) balance radiative energy loss.

Arya

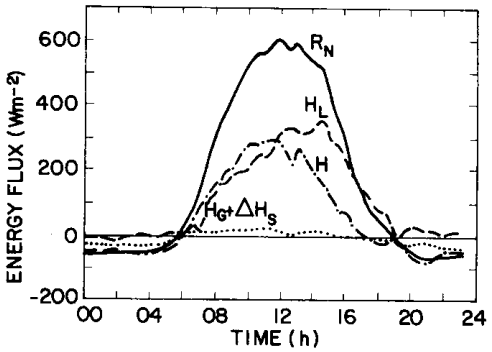

Fig. 2.5 Observed energy budget of a Douglas fir canopy at Haney, British Columbia, on July 23, 1970. [From Oke (1987); after McNaughton and Black (1973).]

Net radiation at the surface

The net radiation R_N is due to the difference between downwelling and upwelling shortwave plus longwave radiative fluxes. The net shortwave flux depends on the incident solar radiation $R_{s\downarrow}$ and on surface albedo a_s. The net longwave flux depends upon the downwelling longwave radiation $R_{L\downarrow}$, the surface emissivity ε_s, and the radiating temperature T_s:

$$R_N = R_{s\downarrow} - R_{s\uparrow} + R_{L\downarrow} - R_{L\uparrow} = (1 - a_s)R_{s\downarrow} + R_{L\downarrow} - \{(1-\varepsilon_s)R_{L\downarrow} + \varepsilon_s\sigma T_s^4\}$$

Thus, the surface characteristics critically influence R_N. A table of typical surface radiative characteristics is given below. Albedos are quite diverse, while emissivities are usually near, but not equal, to 1.

Arya

Table 3.1
Radiative Properties of Natural Surfaces[a]

Surface type	Other specifications	Albedo (a)	Emissivity (ε)
Water	Small zenith angle	0.03–0.10	0.92–0.97
	Large zenith angle	0.10–0.50	0.92–0.97
Snow	Old	0.40–0.70	0.82–0.89
	Fresh	0.45–0.95	0.90–0.99
Ice	Sea	0.30–0.40	0.92–0.97
	Glacier	0.20–0.40	
Bare sand	Dry	0.35–0.45	0.84–0.90
	Wet	0.20–0.30	0.91–0.95
Bare soil	Dry clay	0.20–0.35	0.95
	Moist clay	0.10–0.20	0.97
	Wet fallow field	0.05–0.07	
Paved	Concrete	0.17–0.27	0.71–0.88
	Black gravel road	0.05–0.10	0.88–0.95
Grass	Long (1 m)	0.16–0.26	0.90–0.95
	Short (0.02 m)		
Agricultural	Wheat, rice, etc.	0.10–0.25	0.90–0.99
	Orchards	0.15–0.20	0.90–0.95
Forests	Deciduous	0.10–0.20	0.97–0.98
	Coniferous	0.05–0.15	0.97–0.99

[a] Compiled from Sellers (1965), Kondratyev (1969), and Oke (1978).

Arya

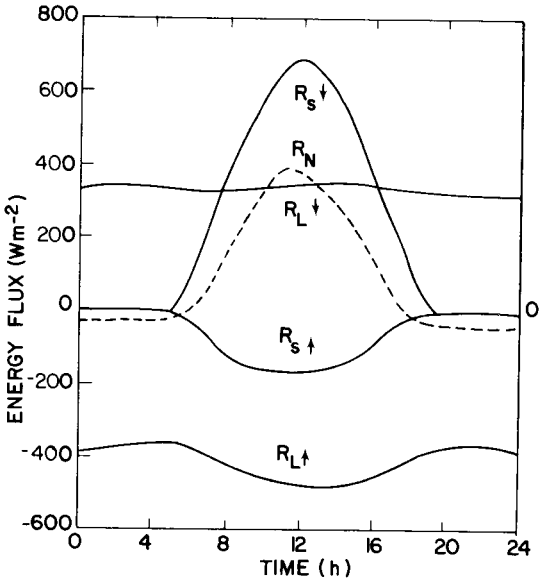

Fig. 3.4 Observed radiation budget over a 0.2-m-tall stand of native grass at Matador Saskatchewan, on July 30, 1971. [From Oke (1987); after Ripley and Redmann (1976).]

An example of the surface radiation components is shown above.

Soil temperatures and heat flux

The surface or skin temperature is important for the radiative balance of the surface and for predicting frost and dew. It can be quite different than the 'surface' air temperature, which is conventionally measured at 1.5-2 m. In fact, it can be difficult to even measure *in situ* because it is difficult to shield and ventilate a sensor placed at the surface. Furthermore, if there is a plant canopy or surface inhomogeneity, there is no single uniquely definable surface temperature. Radiatively, an apparent surface temperature can be determined from the upward longwave energy flux if the emissivity is known. Large diurnal variations in skin temperature are achieved for bare, dry surfaces in clear calm conditions. Under such conditions, midday skin temperature may reach 50-60 C, while early morning skin temperatures can drop to 10-20 C.

The surface temperature is related to the profile of temperature in the subsurface medium, as illustrated in the figures on the next page. In a solid medium, the subsurface temperature profile is governed by heat conduction. Deeper in the soil, the diurnal temperature cycle decreases and lags the cycle of skin temperature. Over an annual cycle, similar waves penetrate further into the soil.

If z is depth into the soil and $T(z, t)$ is soil temperature, Fourier's law of heat conduction states:

$$H_G = -k\partial T/\partial z, \quad (k = \text{thermal conductivity})$$

Thermal energy conservation implies that

$$\rho c \frac{\partial T}{\partial t} = -\frac{\partial H_G}{\partial z} \quad (\rho = \text{density}, c = \text{heat capacity})$$

Combining these two equations and assuming that the subsurface medium is homogeneous, so that material constants do not depend on z, we obtain the diffusion equation

Observed diurnal subsurface soil temperature variability (Arya)

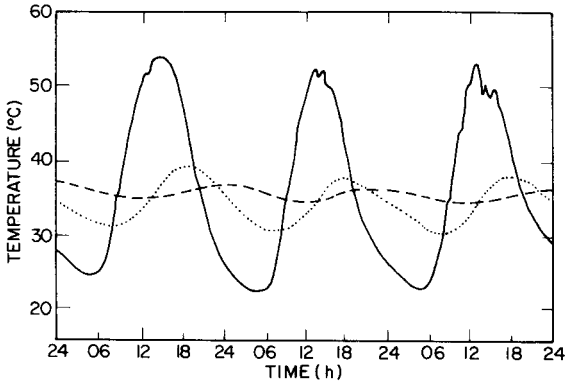

Fig. 4.1 Observed diurnal course of subsurface soil temperatures at various depths in a sandy loam with bare surface. ——, 2.5 cm; ·····, 15 cm; ---, 30 cm. [From Deacon (1969); after West (1952).]

Observed annual subsurface soil temperature variability (Arya)

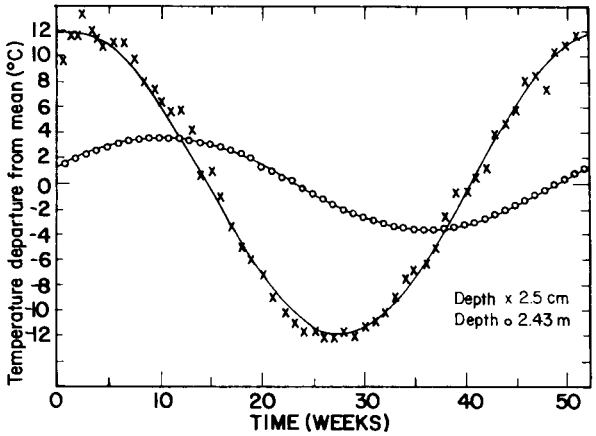

Fig. 4.2 Annual temperature waves in the weekly averaged subsurface soil temperatures at two depths in a sandy loam soil. ×, 2.5 cm; ○, 2.43 m. Fitted solid curves are sine waves. [From Deacon (1969); after West (1952).]

Table A7. *Representative values of the thermal conductivity k_s, specific heat c_s, density ρ_s and thermal diffusivity κ_s for various types of surface based mainly on Table* 11-3 *in Pielke* (1984) Garratt

Data for clay and sand are approximately consistent with Eq. A24, in which C_{si} is equal to 2.7×10^6 and 2.2×10^6 J m^{-3} K^{-1} for clay and sand respectively; C_w is equal to $\rho_w c_l$, with $\rho_w = 1000$ kg m^{-3} and $c_l = 4186$ J kg^{-1} K^{-1}; and η_s is taken from Table A9. The reader should also consult e.g. Geiger (1965, Table 10), Hillel (1982, Table 9.3) and Oke (1987, Table 2.1).

Surface	k_s (W m^{-1} K^{-1})	c_s (J kg^{-1} K^{-1})	ρ_s (kg m^{-3})	κ_s (10^{-6} m^2 s^{-1})
Sand soil				
dry	0.3	800	1600	0.23
$\eta = 0.2$	1.9	1260	1800	0.84
$\eta = 0.4$	2.2	1480	2000	0.74
Clay soil				
dry	0.25	890	1600	0.18
$\eta = 0.2$	1.1	1170	1800	0.52
$\eta = 0.4$	1.6	1550	2000	0.52
rock	2.9	750	2700	1.4
ice	2.5	2100	910	1.3
snow				
old	1.0	2090	640	0.7
new	0.1	2090	150	0.3
water	0.6	4186	1000	0.14

$$\frac{\partial T}{\partial t} = \kappa \frac{\partial^2 T}{\partial z^2} \quad (\kappa = k/\rho c = \text{thermal diffusivity}) \tag{1}$$

A table of material properties is given below; the thermal conductivity varies over almost two orders of magnitude from new snow (low) to rock (high). Wet soils have conductivities about five times as large as dry soils. The thermal diffusivity shows similar trends, but less variation. Surprisingly, κ is smallest for water due to its large heat capacity.

It is illuminating to look at a soil temperature wave forced by a sinusoidal variation in surface temperature. We assume a deep soil temperature $T(z \to \infty) = \overline{T}$ and take $T(0) = \overline{T} + A \cos \omega t$. We look for a solution to (1) that is also sinusoidal in time with the same frequency ω:

$$T(z, t) = \overline{T} + \mathrm{Re}\{a(z)\exp(i\omega t)\}$$

Here $a(z)$ is a complex-valued function of z. To satisfy (1):

$$i\omega a = -\kappa \, d^2a/dz^2 \tag{2}$$

To satisfy the boundary conditions,

$$a(0) = A, \; a(z \to \infty) = 0$$

The solution of (2) that satisfies the BCs is

$$a(z) = A \exp(-[1 + i]z/D), \; D = (2\kappa/\omega)^{1/2}$$

Garratt

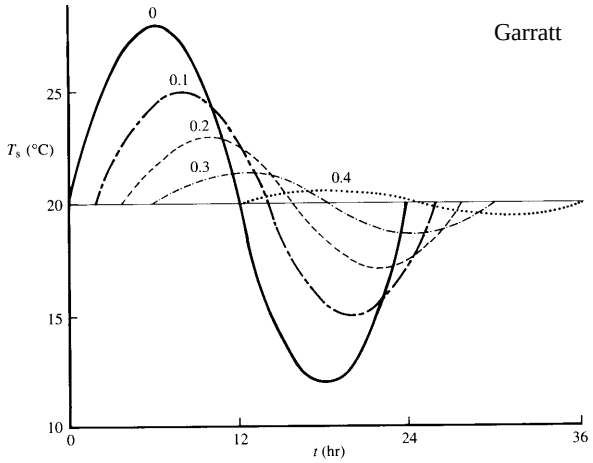

Fig. 5.1 Idealized variation of soil temperature through a diurnal cycle for several depths in the soil (indicated in metres). The curves represent the solutions to Eq. 5.7 for sinusoidal forcing; these are given by Eq. 5.8. A uniform soil is assumed with $\kappa_s = 0.8 \times 10^{-6}\ \mathrm{m^2\,s^{-1}}$ and $k_s = 1.68\ \mathrm{W\,m^{-1}\,K^{-1}}$.

$$T(z, t) = \overline{T} + \exp(-z/D)\cos(\omega t - z/D) \qquad (3)$$

This solution is shown above. The temperature wave damps exponentially with depth z, and lags the surface temperature wave by a phase z/D, which increases with depth (see observations at bottom of page). The **damping depth** D to which the temperature wave penetrates increases as the oscillation frequency slows and is larger if the thermal diffusivity is larger. For moist soil ($\kappa = 0.8\times10^{-6}\ \mathrm{m^2 s^{-1}}$), $D = 0.14$ m for the diurnal cycle and 2.8 m for the annual cycle.

The ground heat flux at the surface is

$$H_G = -k\,\partial T/\partial z(0) = -kA/D\ \mathrm{Re}\{[1 + i]\exp(i\omega t)\} = \rho c(\kappa\omega)^{1/2}\cos(\omega t + \pi/4)$$

It leads the surface temperature wave by 1/8 cycle. Hence, the ground heat flux is largest three hours ahead of the surface temperature for a diurnally varying surface temperature cycle.

In practice, the diurnal cycle of surface temperature is not sinusoidal. Furthermore, the surface temperature interacts with the sensible and latent heat fluxes so that the surface boundary condition is really the energy balance of the surface, which is coupled to the atmosphere. Lastly, testing of these formulas is complicated by the fact the temperature within 1 cm of the ground can be non-uniform, so the surface temperature and ground heat flux must be inferred from measurements

Arya

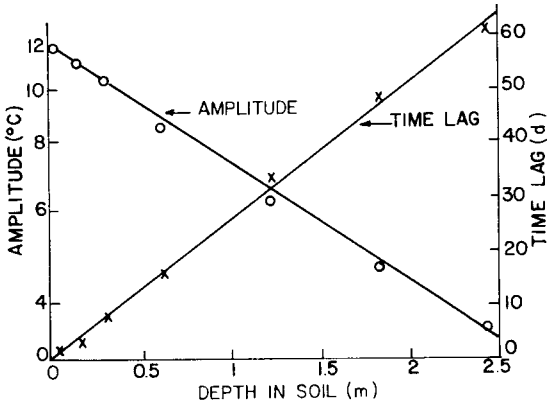

Fig. 4.4 Variations of amplitude and time lag of the annual soil temperature waves with depth in the soil. [From Deacon (1969).]

across a buried ‘flux plate’, a thin plate buried within the soil that measures heat flux based on the temperature difference across it, typically at a depth of 1-2 cm.

Lecture 11. Surface Evaporation (Garratt 5.3)

The partitioning of the surface turbulent energy flux into sensible vs. latent heat flux is very important to the boundary layer development. Over ocean, SST varies relatively slowly and bulk formulas are useful, but over land, the surface temperature and humidity depend on interactions of the BL and the surface. How, then, can the partitioning be predicted?

For saturated ideal surfaces (such as saturated soil or wet vegetation), this is relatively straightforward. Suppose that the surface temperature is T_0. Then the surface mixing ratio is its saturation value $q^*(T_0)$. Let z_1 denote a measurement height within the surface layer (e. g. 2 m or 10 m), at which the temperature and humidity are T_1 and q_1. The stability is characterized by an Obhukov length L. The roughness length and thermal roughness lengths are z_0 and z_T. Then Monin-Obuhkov theory implies that the sensible and latent heat fluxes are

$$H_S = \rho c_p C_H V_1 (T_0 - T_1),$$

$$H_L = \rho L C_H V_1 (q_0 - q_1), \quad \text{where } C_H = \text{fn}(V_1, z_1, z_0, z_T, L)$$

We can eliminate T_0 using a linearized version of the Clausius-Clapeyron equations:

$$q_0 - q^*(T_1) = (dq^*/dT)_R (T_0 - T_1), \quad R \text{ indicates a value at a reference temperature,}$$

that ideally should be close to $(T_0 + T_1)/2$

$$H_L = s^* H_S + \rho L C_H V_1 (q^*(T_1) - q_1), \quad s^* = (L/c_p)(dq^*/dT)_R \text{ (= 0.7 at 273 K, 3.3 at 300 K)} \quad (1)$$

This equation expresses latent heat flux in terms of sensible heat flux and the saturation deficit at the measurement level. It is immediately apparent that the Bowen ratio H_S/H_L must be at most s^{*-1} over a saturated surface, and that it drops as the relative humidity of the overlying air decreases. At higher temperatures, latent heat fluxes tend to become more dominant. For an ideal surface, (1), together with energy balance

$$R_N - H_G = H_S + H_L$$

can be solved for H_L:

$$H_L = LE_P = \Gamma(R_N - H_G) + (1 - \Gamma)\rho L C_H V_1 (q^*(T_1) - q_1) \quad (2)$$

$$\Gamma = s^*/(s^* + 1) \text{ (= 0.4 at 273 K, 0.77 at 300 K)}$$

The corresponding evaporation rate E_P is called the **potential evaporation**, and is the maximum possible evaporation rate given the surface characteristics and the atmospheric state at the measurement height. If the surface is not saturated, the evaporation rate will be less than E_P. The figure on the next page shows H_L vs. the net surface energy influx $R_N - H_G$ for T_1 = 293 K and RH_1 = 57%, at a height of z_1 = 10 m, with a geostrophic wind speed of 10 m s^{-1}, assuming a range of surface roughness. Especially over rough surfaces (forest), H_L often exceeds $R_N - H_G$, so the sensible heat flux must be negative by up to 100 W m^{-2}. The Bowen ratio is quite small (0.2 or less) for all the saturated surfaces shown in this figure.

Garratt

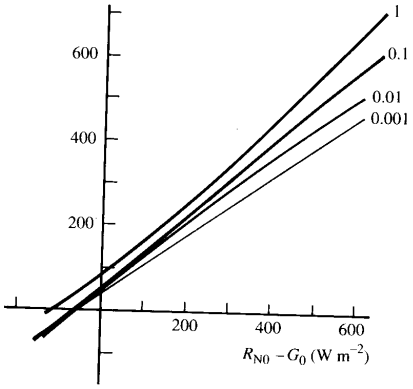

Fig. 5.6 Potential evaporation for different wet surfaces calculated from Eq. 5.26. In (*a*) neutral conditions have been assumed, and in (*b*) the full stability correction in r_{aV} is included (see Eqs. 3.47 and 3.57). Note how the effects of thermal stability tend to reduce the direct influence of aerodynamic roughness. Values of z_0 are as follows: 0.001 m, lake; 0.01 m, grass; 0.1 m, scrub; 1 m, forest. Further details of the calculations can be found in Webb (1975).

Evaporation from dry vegetation

We consider a fully vegetated surface with a single effective surface temperature and humidity (a 'single-layer canopy'). The sensible heat flux is originates at the leaf surfaces, whose temperature is T_0. The latent heat flux is driven by evaporation of liquid water out of the intercellular spaces within the leaves through the stomata, which are channels from the leaf interior to its surface. The evaporation is proportional to the humidity difference between the saturated inside of the stomata and the ambient air next to the leaves. The constant of proportionality is called the **stomatal resistance** (units of inverse velocity)

$$r_{st} = \rho(q^*(T_0) - q_0)/E \tag{3}$$

Plants regulates transport of water vapor and other gasses through the stomata to maintain an optimal internal environment, largely shutting down the stomata when moisture-stressed. Hence r_{st} depends not only on the vegetation type, but also soil moisture, temperature, etc. Table 5.1 of Garratt shows measured r_{st}, which varies form 30 -300 s m^{-1}.

By analogy, we can define an **aerodynamic resistance**

$$r_a = (C_H V_1)^{-1} = \rho(q_0 - q_1)/E \tag{4}$$

Typical values of r_a are 100 s m^{-1}, decreasing in high wind or highly convective conditions. This is comparable to the stomatal resistance. Working in terms of aerodynamic resistance in place of C_H is convenient in this context, as we shall see next, because these resistances add:

$$r_{st} + r_a = \rho(q^*(T_0) - q_0)/E + \rho(q_0 - q_1)/E = \rho(q^*(T_0) - q_1)/E, \tag{5}$$

i. e. E is identical to the evaporation rate over an equivalent saturated surface with aerodynamic resistance $r_{st} + r_a$. The same manipulations that led to (1) and (2) now lead to:

$$H_S = \rho c_p(T_0 - T_1)/r_a$$

$$H_L = LE = \rho(q^*(T_0) - q_1)/(r_{st} + r_a) = \{s^* H_S + \rho L(q^*(T_1) - q_1)\}\{r_a/(r_{st} + r_a)\}$$

$$H_L = \Gamma^*(R_N - H_G) + (1 - \Gamma^*)\rho L(q^*(T_1) - q_1)/(r_{st} + r_a) \quad , \tag{6}$$

where $\Gamma^* = s^*/(s^* + 1 + r_{st}/r_a)$

This is the **Penman-Monteith** relationship. Comparing (6) to (2), we find that $\Gamma^* < \Gamma$, so the heat flux will be partitioned more into sensible heating, especially if stomatal resistance is high, winds are high, or the BL is unstable. The effect is magnified at cold temperatures where s^* is small. The ratio of H_L to the saturated latent heat flux (2) given the same energy influx R_N - H_G is

$$H_L/H_{L,\,\mathrm{sat}} = \frac{1}{1 + (1-\Gamma)(r_{st}/r_a)}$$

Calculations of this ratio for neutral conditions, a 10 m s^{-1} geostrophic wind speed, and various surface roughnesses are shown in the figure below. For short grass, the surface transfer coefficient is low, so the aerodynamic resistance is high and stomatal resistance does not play a crucial role at high temperatures (though at low temperatures it cuts off a larger fraction of the latent heat flux). For forests, stomatal resistance is very important due to the high surface roughness (low aerodynamic resistance).

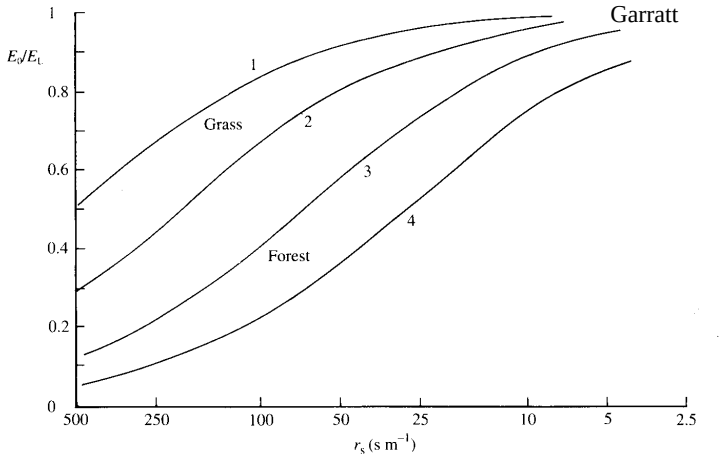

Fig. 5.8 Variations of E_0/E_L (Eq. 5.37) with surface resistance. Values of r_{aV} have been calculated for neutral conditions, with $z_q = z_0/7.4$. For short grass ($z_0 = 0.0025$ m): curve 1, $T = 303$ K; curve 2, $T = 278$ K. For forest ($z_0 = 0.75$ m): curve 3, $T = 303$ K; curve 4, $T = 278$ K.

Soil moisture

If the surface is partly or wholly unvegetated, the evaporation rate depends on the available soil moisture. Soil moisture is also important because it modulates the thermal conductivity and hence the ground heat flux, and affects the surface albedo as well as transpiration by surface vegetation. For instance, Idso et al. (1975) found that for a given soil, albedo varied from 0.14 when the soil was moist to 0.31 when it was completely dry at the surface.

If the soil-surface relative humidity RH_0 is known, then the evaporation is

$$E = \rho(RH_0 q^*(T_0) - q_1)/r_a \,.$$

Note that net evaporation ceases when the mixing ratio at the surface drops below the mixing ratio at the measurement height, which does not require the soil to be completely dry. Soil moisture can be expressed as a volumetric moisture content η (unitless), which does not exceed a saturated value η_s, usually around 0.4. When the soil is saturated, moisture can easily flow through it, but not all pore spaces are water-filled. As the soil becomes less saturated, water is increasingly bound to the

soil by adsorption (chemicals) and surface tension.

The movement of water through the soil is down the gradient of a combined gravitational potential gz (here we take z as depth below the surface) plus a moisture potential $g\psi(\eta)$. The moisture potential is always negative, and becomes much more so as the soil dries out and its remaining water is tightly bound. Note ψ has units of height. The downward flux of water is

$$F_w = -\rho_w K(\eta)\partial(\psi + z)/\partial z, \quad \text{(Darcy's law)}$$

where $K(\eta)$ is a hydraulic conductivity (units of m s^{-1}), which is a very rapidly increasing function of soil moisture. Conservation of soil moisture requires

$$\rho_w \partial\eta/\partial t = -\partial F_w/\partial z$$

The surface relative humidity is

$$RH_0 = \exp(-g\psi|_{z=0}/R_v T_0)$$

i. e. the more tightly bound the surface moisture is to the soil, the less it is free to evaporate. Empirical forms for ψ and K as functions of η have been fitted to field data for various soils:

$$\psi = \psi_s(\eta/\eta_s)^{-b}$$

$$K = K_s(\eta/\eta_s)^{2b+3}$$

where ψ_s and K_s are saturation values, depending on the soil, and the exponent b is 4-12. For b = 5, halving the soil moisture increases the moisture potential by a factor of 32 and decreases the hydraulic conductivity by a factor of 4000! Because these quantities are so strongly dependent on η, one can define a critical surface soil moisture, the wilting point η_w, above which the surface relative humidity RH_0 is larger than 99%, and below which it rapidly drops. The wilting point can be calculated as the η below which the hydraulic suction $-\psi$ exceeds 150 m.

Garratt

Table A9. *Soil moisture quantities for a range of soil types, based on Clapp and Hornberger* (1978)

Quantities shown are as follows: η_s is the saturation moisture content (volume per volume), η_w is the wilting value of the moisture constant which assumes 150 m suction (i.e. the value of η when $\psi = -150$ m), ψ_s is the saturation moisture potential and $K_{\eta s}$ is the saturation hydraulic conductivity; b is an index parameter (see Eqs. 5.46–5.48).

Soil type	η_s ($m^3\ m^{-3}$)	ψ_s (m)	$K_{\eta s}$ (10^{-6} m s^{-1})	b	η_w ($m^3\ m^{-3}$)
1. sand	0.395	− 0.121	176	4.05	0.0677
2. loamy sand	0.410	− 0.090	156.3	4.38	0.075
3. sandy loam	0.435	− 0.218	34.1	4.90	0.1142
4. silt loam	0.485	− 0.786	7.2	5.30	0.1794
5. loam	0.451	− 0.478	7.0	5.39	0.1547
6. sandy clay loam	0.420	− 0.299	6.3	7.12	0.1749
7. silty clay loam	0.477	− 0.356	1.7	7.75	0.2181
8. clay loam	0.476	− 0.630	2.5	8.52	0.2498
9. sandy clay	0.426	− 0.153	2.2	10.40	0.2193
10. silty clay	0.492	− 0.490	1.0	10.40	0.2832
11. clay	0.482	− 0.405	1.3	11.40	0.2864

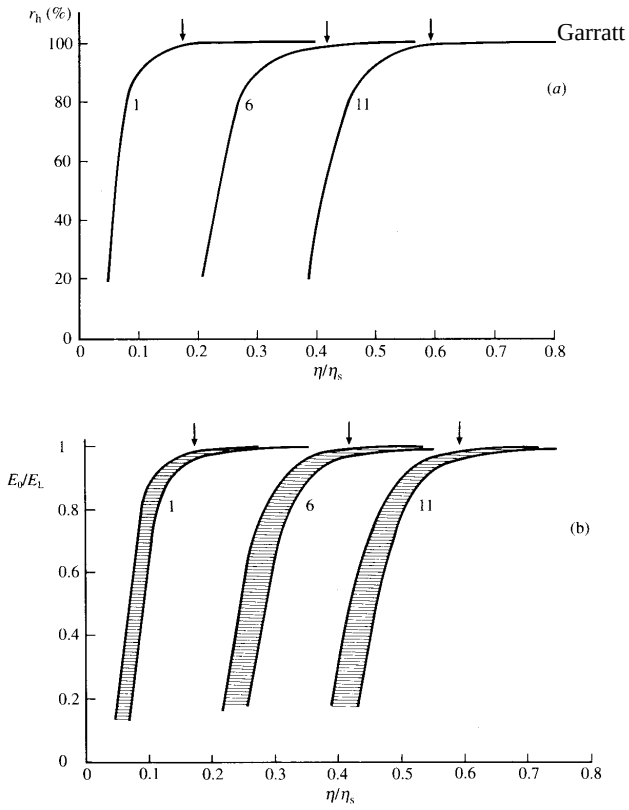

Fig. 5.9 (*a*) Relative humidity r_h as a function of relative soil moisture content η/η_s, based on Eq. 5.49 and data in Table A9 for soil types 1 (sand), 6 (loam) and 11 (clay). Calculations are for a temperature T_0 of 303 K. The vertical arrows indicate the wilting points. Note that combining Eqs. 5.46 and 5.49 allows r_h to be calculated from $\ln r_h = -(g/R_v T_0)\psi_s(\eta/\eta_s)^{-b}$. (*b*) E_0/E_L as a function of the relative soil moisture content, based on numerical simulations in an atmospheric model for a range of climate conditions (mid-latitude summer) represented by the shaded regions (the temperature range is 283–303 K and $q = 0.005$).

Landuse Integer Identification	Landuse Description	Albedo (%)		Moisture Avail. (%)		Emissivity (% at 9 μm)		Roughness Length (cm)		Thermal Inertia (cal cm^{-2} K^{-1} s$^{-1/2}$)	
		Sum	Win	Sum	Win	Sum	Win	Sum	Win	Sum	Win
1	Urban land	18	18	5	10	88	88	50	50	0.03	0.03
2	Agriculture	17	23	30	60	92	92	15	5	0.04	0.04
3	Range-grassland	19	23	15	30	92	92	12	10	0.03	0.04
4	Deciduous forest	16	17	30	60	93	93	50	50	0.04	0.05
5	Coniferous forest	12	12	30	60	95	95	50	50	0.04	0.05
6	Mixed forest and wet land	14	14	35	70	95	95	40	40	0.05	0.06
7	Water	8	8	100	100	98	98	.0001	.0001	0.06	0.06
8	Marsh or wet land	14	14	50	75	95	95	20	20	0.06	0.06
9	Desert	25	25	2	5	85	85	10	10	0.02	0.02
10	Tundra	15	70	50	90	92	92	10	10	0.05	0.05
11	Permanent ice	55	70	95	95	95	95	5	5	0.05	0.05
12	Tropical or sub-tropical forest	12	12	50	50	95	95	50	50	0.05	0.05
13	Savannah	20	20	15	15	92	92	15	15	0.03	0.03

MM5 surface types and their characteristics (Appendix 4 of MM5 manual)

Parameterization of surface evaporation in large-scale models

In practice, simplified formulations of soil moisture and transpiration are used in most models. We will defer most of these until later. However, the MM5 formulation of surface evaporation is particularly simplified. It is

$$E = \rho L C_H V_1 M (q^*(T_0) - q_1),$$

i. e. the standard formula for evaporation off a *saturated* surface at the ground temperature T_0 (calculated by the model) multiplied by a moisture availability factor M between 0 and 1 that is assumed to depend only on the surface type. This formulation avoids the need to initialize soil moisture, but is tantamount to assuming a surface resistance that is proportional to the aerodynamic resistance, with

$$r_s/r_a = (1 - M)/M$$

While this type of formulation can be tuned to give reasonable results on an annually averaged basis, it is likely to be in error by a factor of two or more in individual situations, because r_s and r_a are both subject to large and independent fluctuations. More sophisticated schemes explicitly prognose soil moisture (often using relaxation to specified values deep within the soil to control fluctuations) and vegetation characteristics and determine the evaporation from these.

Lecture 12. The diurnal cycle and the nocturnal BL

Over flat land, under clear skies and with weak thermal advection, the atmospheric boundary layer undergoes a pronounced diurnal cycle. A schematic and an example from the Wangara experiment are shown on the next page. This 'archetypical' diurnal cycle is muted by clouds and can be entirely obscured by rapid changes in the free atmospheric conditions due for instance to the passage of a midlatitude cyclone or front. It is also highly modified by terrain or nearby land-sea contrasts. Despite these caveats, it is illuminating to study the archetypical case in more depth

During the night, the BL is stable due to surface longwave cooling, and a shallow temperature inversion of typically 100-500 m builds up. After dawn, surface heating builds up a shallow convective mixed layer, which deepens slowly and rapidly warms until it fully erodes the nocturnal stable layer. At this point, the top of the new mixed layer starts to penetrate into the **residual layer**, the remnants of the previous day's afternoon mixed layer. This layer is very weakly stratified, so the new mixed layer rapidly deepens into it, until it encounters the top of the previous day's mixed layer, which tends to be marked by a weak inversion. At this point, further BL warming occurs much more slowly, as a much deeper layer must be warmed than in the early morning. In the late afternoon, the solar heating is no longer sufficient to maintain upward surface buoyancy fluxes. Within an hour (a few eddy turnover times), turbulence collapses through most of the boundary layer and becomes restricted to a shallow layer, typically 100 m deep, driven by surface drag. During the night, clear-air radiative cooling is most intense near the cold surface, enhancing the static stability of the lowest couple of hundred meters of air. Much of the nocturnal inversion can be attributed to this cooling, rather than downward turbulent heat fluxes. However, downward heat fluxes of up to 50 W m^{-2} can occur near the surface at night under moderately strong geostrophic winds.

Morning growth of the boundary layer (Garratt 6.1)

The rate of growth of the convective mixed layer is dictated primarily by energy balance, though entrainment dynamics also play a significant role. As a simple example, consider the growth of a mixed layer driven by a surface buoyancy flux B_0 into an atmosphere of constant buoyancy frequency N^2. The mean buoyancy profile in the free troposphere is

$b^+(z) = N^2 z$ (= $g(\theta_v^+(z) - \theta_{vR})/\theta_{vR}$, where we have chosen θ_{vR} as the initial θ_v^+ at $z = 0$.)

We assume (i) that the buoyancy flux is turned on at time $t = 0$, and (ii) that it leads to a convective mixed layer of depth $h(t)$ governed by the entrainment closure

$$\overline{w'b'}(h) = -w_e \Delta b = -\beta B_0 \quad (\beta = 0.2, \text{ empirically}) \tag{1}$$

It is interesting to compare the solution with a realistic β to the case $\beta = 0$. In the latter limit, called **encroachment**, convection is assumed not to be penetrative, and the mixed layer entrains air only when its buoyancy is no larger than that of the mixed layer air. Lastly, (iii) we neglect any mean vertical motion within the atmosphere, so

$$w_e = dh/dt$$

The buoyancy $b(z, t)$ obeys

$$\partial b/\partial t = -\partial/\partial z(\overline{w'b'})$$

Garratt

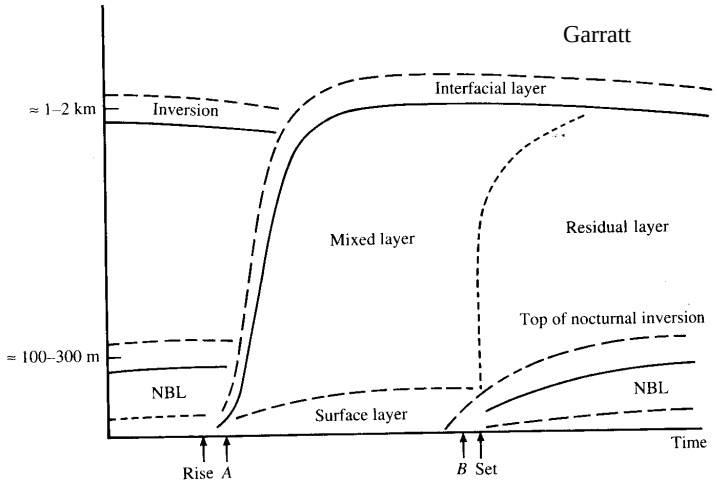

Fig. 6.1 Schematic representation of ABL evolution throughout the diurnal period over land under clear skies.

Arya

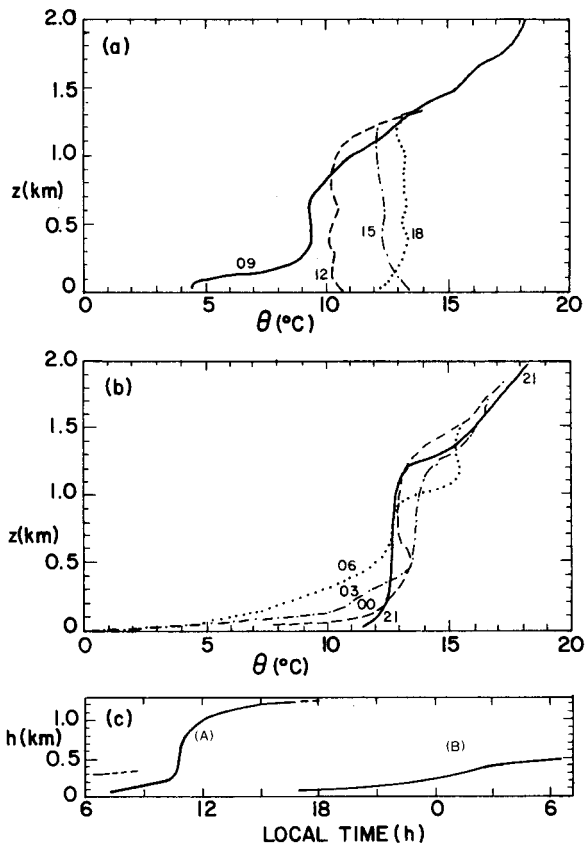

Fig. 5.2 Diurnal variation of potential temperature profiles and the PBL height during (a) day 33 and (b) days 33–34 of the Wangara Experiment. (c) Curve A, convective; Curve B, stable. [After Deardorff (1978).]

Integrating from the surface up to a fixed height H above the mixed layer top, we see that

$$\frac{\partial}{\partial t}\int_0^H b\,dz \;=\; -\overline{w'b'}\Big|_0^H \;=\; B_0$$

Graphically, let A be the net area added to the buoyancy profile by the heating of the BL. Then

$$A = B_0 t \tag{2}$$

We can now compare the cases of encroachment and an entraining boundary layer. The encroaching BL has depth given by

$$h(N^2 h)/2 = A = B_0 t \quad \Rightarrow \quad h_{encr} = (2B_0 t/N^2)^{1/2}$$

As expected, h deepens more slowly as it gets larger, since more heat must be imparted to a deeper boundary layer to raise its buoyancy by a given amount.

For the entraining BL, there is a 'similarity' solution in which the buoyancy profile retains the same shape as it grows, so that

$$\Delta b(t) = cN^2 h(t) \quad (c \text{ is an as yet unknown constant}).$$

Consistency of (1) and (2) determines c. From (1),

$$\beta B_0 \;= w_e \Delta b \;= (dh/dt) cN^2 h.$$

Integrating this equation from time 0 to t, starting with $h(0) = 0$, we get

$$\beta B_0 t = cN^2 h^2/2 \tag{3}$$

Turning now to (2), we write A as the difference of the 'positive area' A_P where the mixed layer buoyancy $b_m(t)$ exceeds the original environmental buoyancy and the negative area A_N where pen-

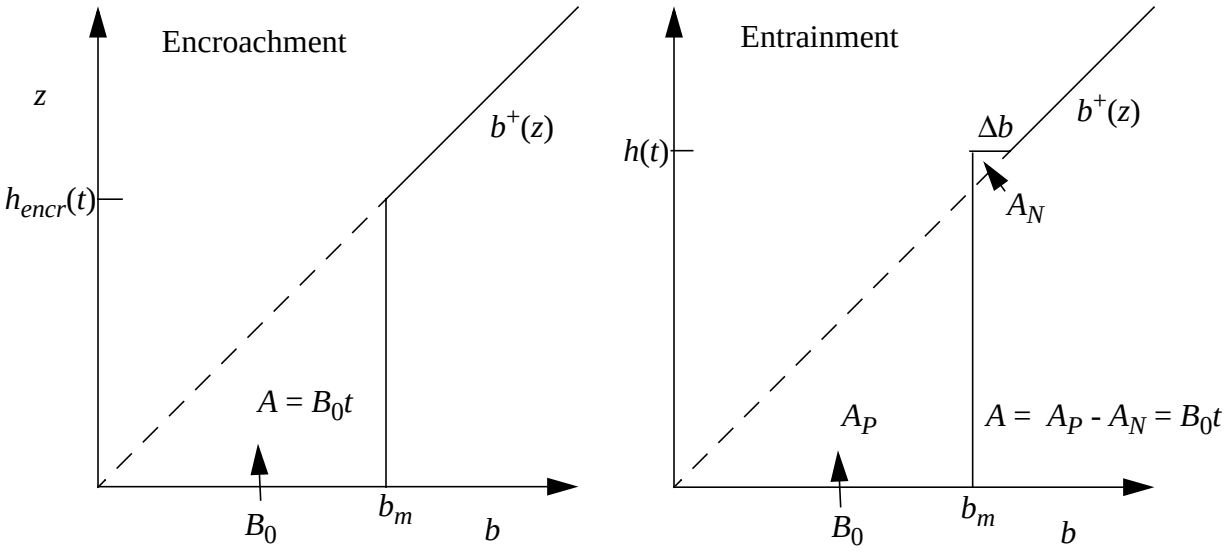

Convective mixed layer evolution illustrating more rapid deepening if entrainment is assumed to be penetrative ($\beta = 0.2$), compared to encroachment ($\beta = 0$).

etrative convection has reduced the buoyancy. From the figure above, we see that $b_m + \Delta b = b^+(t) = N^2 h$, so $b_m = (1\text{-}c)N^2 h$. The heights of the triangles making up A_P and A_N are N^{-2} times as long as their bases, so the area of A_P is $b_m(b_m/N^2)/2$ and similarly for A_N. Hence (2) can be written:

$$B_0 t = A = A_P - A_N = b_m{}^2/2N^2 - \Delta b^2/2N^2 = [(1\text{-}c)^2 - c^2]N^2 h^2/2 = (1 - 2c)N^2 h^2/2. \qquad (4)$$

Dividing (3) by (4), we see that $\beta = c/(1 - 2c)$, or that $c = \beta/(1 + 2\beta)$. It follows from (4) that

$$h_{entr} = (2B_0 t/N^2(1 - 2c))^{1/2} = (2B_0 t(1 + 2\beta)/N^2)^{1/2} \approx (1 + \beta)h_{encr}$$

We conclude that entrainment contributes about $\beta = 20\%$ to the boundary layer deepening. For a 1 km deep BL and $N^2 = 10^{-4}$ s^{-1}, the inversion strength would be $\Delta b = .14N^2 h \leftrightarrow \Delta\theta_v \approx 0.4$ K, regardless of the surface buoyancy flux. Entrainment hardly changes the boundary layer temperature.

The nocturnal jet

As turbulence dies down in the residual layer in late afternoon, it decouples from the BL. The momentum flux convergence that was helping to reduce and turn the wind during the day suddenly disappears, leaving a wind profile in which there is an imbalance between the two main horizontal

forces, Coriolis force and pressure gradient force. The figure below shows the resulting evolution of the wind during one night of the Wangara experiment (which took place over flat ground). During the night a strong jet develops above the nocturnal BL. In the bottom panel is another example in which the geostrophic wind is also plotted. During the daytime, the wind component along the geostrophic wind direction is subgeostrophic, but at night it is supergeostrophic.

This is one of the cleanest atmospheric examples of an inertial oscillation. The pressure gradient is horizontally uniform, so the ageostrophic wind $\mathbf{u}_a = \mathbf{u} - \mathbf{u}_g$ rotates clockwise with the Coriolis period $2\pi/f$, which at mid-latitudes is somewhat less than a day. Supergeostrophic winds ensue dur-

Garratt

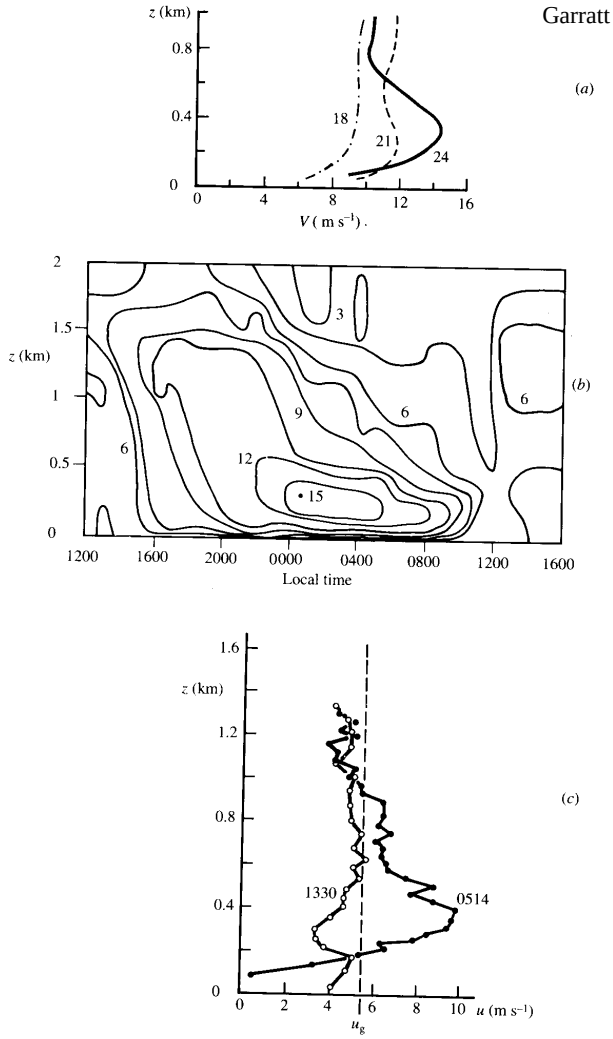

Fig. 6.18 Observations illustrating the formation of the nocturnal jet. (*a*) Wind-speed profiles on day 13 of WANGARA, local times indicated. (*b*) Height–time cross-section of wind speed (in $\mathrm{m\,s^{-1}}$) on days 13/14 at WANGARA. Isopleths of wind speed are drawn at $1.5\,\mathrm{m\,s^{-1}}$ intervals. (*c*) Profiles of the u-component of the wind velocity, with the x-axis along the geostrophic wind direction, for mid-afternoon (1330 UT, 6 August, 1974) and early morning (0514, 7 August, 1974) near Ascot, England. After Thorpe and Guymer (1977), *Quarterly Journal of the Royal Meteorological Society*.

Garratt

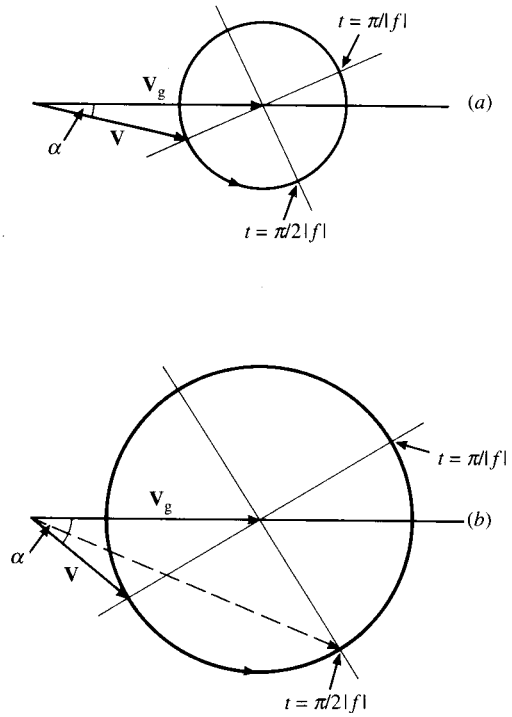

Fig. 6.19 Illustrated solutions of the unbalanced momentum equation (Eq. 6.77) for (*a*) a low-roughness surface and (*b*) a high-roughness surface; undamped inertial oscillations are shown for the southern hemisphere in the form of anticlockwise rotation of the wind vector (**V**) about the geostrophic wind vector ($\mathbf{V}_g$).

ing the night , as shown in the figure above. In the morning, the convective mixed layer deepens into the residual layer, so the wind profile becomes frictionally coupled again. The Great Plains nocturnal southerly jet, prominent during the springtime when it can achieve speeds of 30 m s^{-1} less than 1 km above the surface, partially owes its origin to this mechanism. In this region, climatological southerly geostrophic flow occurs due to a thermal low over the elevated terrain to the west (i. e. the Rockies). The strong enhancement of low-level southerlies during the night help pump humid air northward, where it can help fuel severe thunderstorms and mesoscale convective systems through the night.

Lecture13. The stable BL (Garratt 6.2)

The stable nocturnal BL (NBL) has proved one of the more difficult types of BL to understand and model. The boundary layer tends to be only 50-300 m deep. Turbulence tends to be intermittent and gravity-wave like motions are often intermingled with turbulence, especially in the upper part of the boundary layer. Radiative cooling in the air often has a comparable effect on the stratification to the turbulence itself, reaching 1 K hour^{-1} or more in the lowest 50-100 m (by comparison, a downward heat flux of H_0 = -10 W m^{-2} out of a NBL h = 100 m would cool it at a rate $dq/dt)_{turb}$ = $H_0/\rho c_p h$ = 10^{-4} K s^{-1} = 0.3 K hr^{-1}. Even the largest turbulent eddies do not span the entire BL so there is a tendency to layering of chemicals and aerosols within the BL, especially in the upper part of the BL where turbulence is weakest. Wind profiles are much less well-mixed at night than during the daytime convective BL.

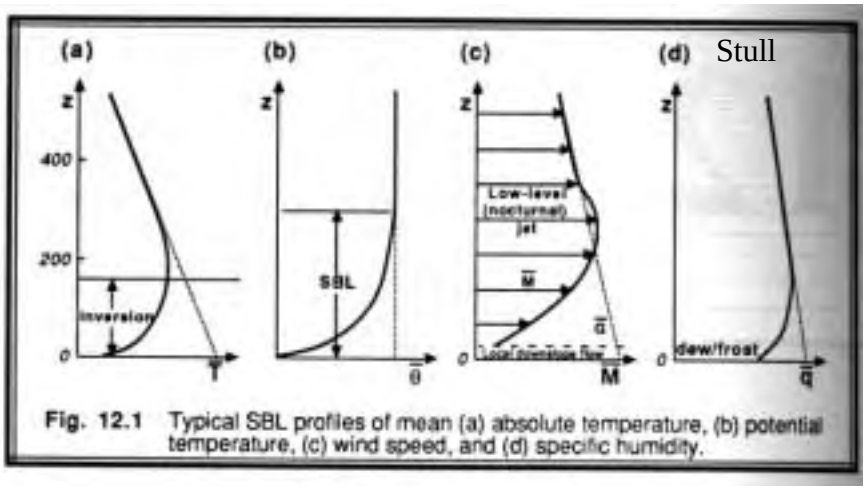

Fig. 12.1 Typical SBL profiles of mean (a) absolute temperature, (b) potential temperature, (c) wind speed, and (d) specific humidity.

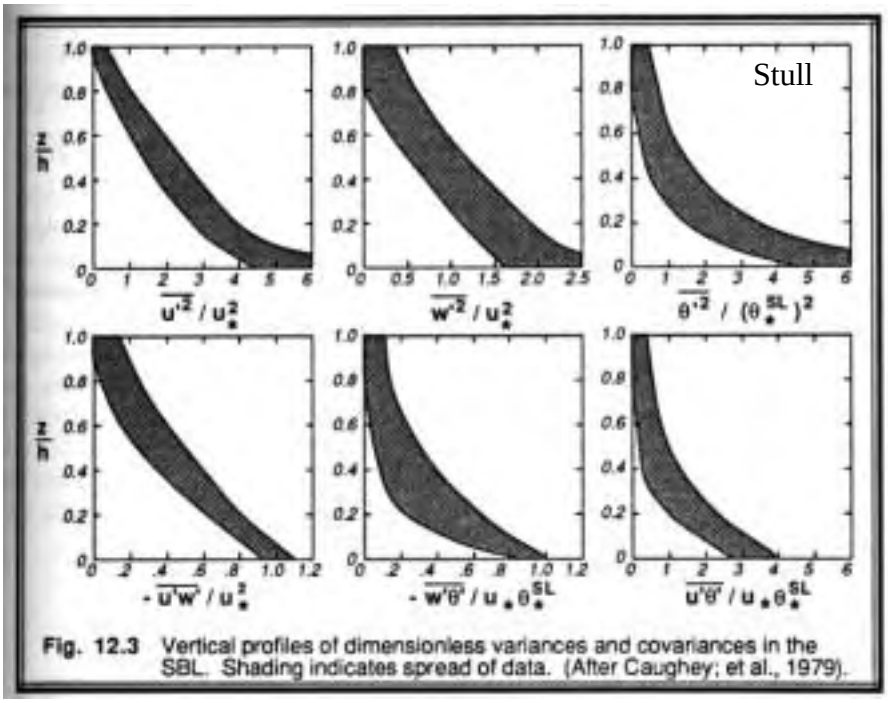

Fig. 12.3 Vertical profiles of dimensionless variances and covariances in the SBL. Shading indicates spread of data. (After Caughey; et al., 1979).

In an NBL, turbulence decreases sharply with height.

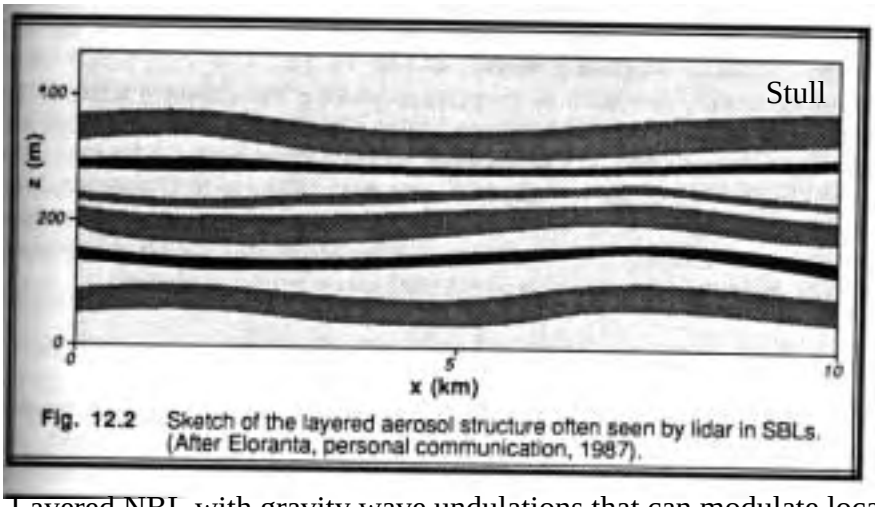

Fig. 12.2 Sketch of the layered aerosol structure often seen by lidar in SBLs. (After Eloranta, personal communication, 1987).

Layered NBL with gravity wave undulations that can modulate local shear, stratification, and hence turbulence.

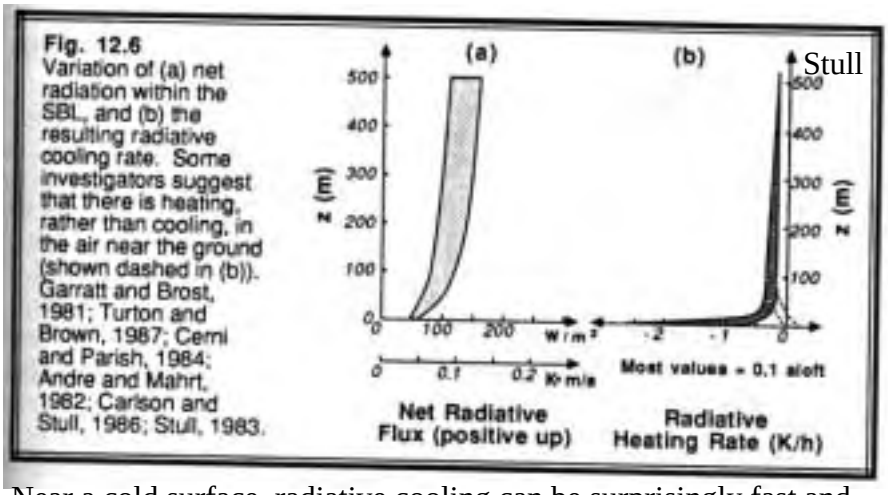

Near a cold surface, radiative cooling can be surprisingly fast and helps maintain a stable stratification.

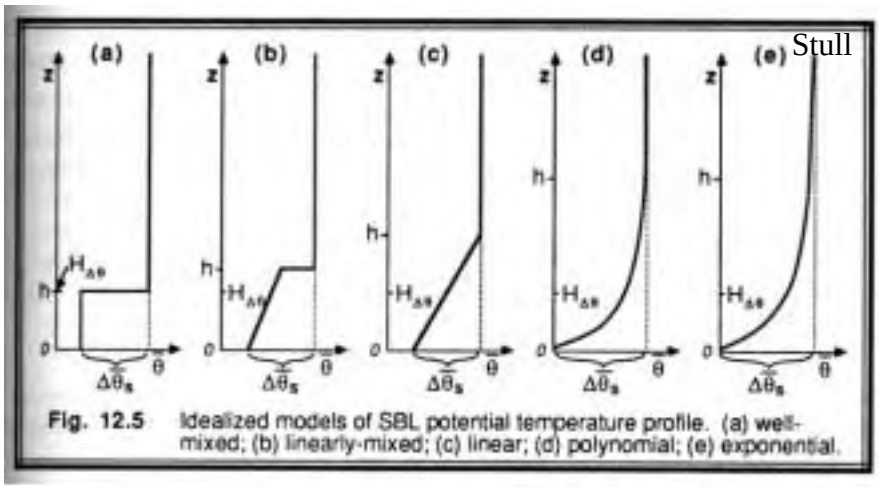

Fig. 12.5 Idealized models of SBL potential temperature profile. (a) well-mixed; (b) linearly-mixed; (c) linear; (d) polynomial; (e) exponential.

(b) typifies strong-wind NBL, (d) a weak-wind NBL under clear sky.

An idealized NBL model

One illuminating theoretical idealization is a NBL of constant depth driven by surface cooling only (Nieuwstadt 1984, *J. Atmos. Sci.*, **41**, 2202-2216). In practice, this is most realistic when winds are strong, producing sufficient turbulence to make substantial downward buoyancy fluxes that are much larger than the radiative flux divergence across the NBL (which is typically less than 10 W m^{-2}). We take the friction velocity u_*, the geostrophic wind U_g (taken to be in the $+x$ direction), and the Coriolis parameter f as given. (In a practical application we would likely know the surface roughness length z_0, not u_*, but we could use the solution below to relate these two parameters). We assume:

(i) The entire BL, extending up to a fixed but unknown height h, is cooling at the same rate, and maintains fixed vertical profiles of stratification and wind.

(ii) No turbulence at the top of the BL

(iii) Within the bulk of the BL (above the surface layer), the sink of TKE due to buoyancy fluxes is assumed to be a fixed fraction Rf ≈ 0.2 of the shear production of TKE. The remaining fraction (0.8) of the shear-produced TKE goes to turbulent dissipation, as transport is observed to be negligible. This is the same as saying that the flux Richardson number Rf = 0.2.

(iv) No radiative cooling within the BL

(v) The (unknown) Obuhkov length L is assumed much smaller than the boundary layer depth. Hence, the largest eddies have a depth which is order of L, since deeper eddies do not have enough TKE to overcome the stratification by the scaling arguments we made in discussing the z-less scaling at $z>>L$ when we discussed Monin-Obhukov theory.

(vi) The eddies act as an unknown, height-dependent eddy viscosity and diffusivity $K_m = K_h$ as suggested by Monin-Obuhkov theory. Hence the gradient Richardson number Ri = Rf, so is also 0.2 throughout the BL.

(vii) The BL is barotropic.

Scaling

Note that one could also use first-order closure on this problem instead of invoking assumptions (iii), (v) and (vi) about the eddies and their transports. This would give a largely similar answer as long as the lengthscale in the first-order closure was on the order of L through most of the boundary layer depth, and could also be used to relax the assumptions of steadiness, uniform cooling rate, no radiative cooling, and no thermal wind. However, the equations would not permit a closed-form solution which displays the parametric dependences clearly. We first scale the steady-state momentum equations, then use a clever approach to solve them.

Assumptions (i) and (ii) imply that if the (unknown) surface buoyancy flux is $B_0 < 0$, then

$$B(z) = \overline{w'b'} = B_0(1 - z/h) \tag{1}$$

The steady-state BL momentum equations are

$$-f(v - v_g) = -\partial/\partial z(\overline{u'w'}) \tag{2}$$

$$f(u - u_g) = -\partial/\partial z(\overline{v'w'}) \tag{3}$$

If {} indicates 'scale of', the above assumptions imply:

$$\{u'\} = \{v'\} = \{w'\} = u_*$$

$$\{K_m\} = \{\text{eddy velocity scale}\}\{\text{eddy lengthscale}\} = u_*L$$

$$\Rightarrow \{\partial u/\partial z\} = \{\overline{u'w'}\}/\{K_m\} = u_*^2/u_*L = u_*/L \text{ (similarly for } v)$$

$$\{\partial/\partial z\} = h^{-1}$$

To apply this scaling to (2)-(3), we differentiate them with respect to z, noting that the geostrophic wind is constant with respect to height by assumption (vii):

$$-f\partial v/\partial z = -\partial^2/\partial z^2(\overline{u'w'}) \tag{4}$$

$$f\,\partial u/\partial z = -\,\partial^2/\partial z^2(\overline{v'w'}) \tag{5}$$

Scaling the two sides of (4), we find

$$\{f\partial v/\partial z\} = fu_*/L = \{\partial^2/\partial z^2(\overline{u'w'})\} = u_*^2/h^2.$$

The same scaling holds for (5). This implies a scaling for BL depth h:

$$h = \gamma_c(u_*L/f)^{1/2} \tag{6}$$

where γ_c is an as yet unknown proportionality constant.

Solution

Now we have understood the scaling of the equations, we solve them in nondimensional form. This is a bit technical, so feel free to skip to the results. It is mathematically advantageous to combine (4) and (5) into one nondimensional complex-valued equation. Let the nondimensional height, shear, momentum flux and eddy viscosity be:

$$\xi = z/h, \quad s_v = (L/u_*)\,\partial(u + iv)/\partial z \text{ and } \sigma = (\overline{u'w'} + i\,\overline{v'w'})/u_*^2, \quad \kappa_m(\xi) = K_m/u_*L$$

Then (4) and (5) can be written:

$$s_v = i\gamma_c^{-2}\,\partial^2\sigma/\partial\xi^2 \tag{7}$$

The boundary conditions come from the definition of friction velocity, and assumption (ii) that stress vanish at the BL top. The surface momentum flux u_*^2 is in the direction opposite the wind. If the (unknown) surface cross-isobaric wind turning angle is α, then the two BCs are:

$$\sigma(0) = -e^{i\alpha}(1 + 0i)$$

$$\sigma(1) = 0 + 0i$$

The eddy viscosity assumption (vi) implies that $\sigma = -\kappa_m(\xi)s_v$. Since the nondimensional eddy viscosity is real, this is equivalent to requiring that the complex numbers σ and s_v. have opposite phase at all nondimensional heights s_v.

The last condition we must enforce is (iii), that buoyant consumption of TKE is 0.2 of shear production:

$$0.2 = \mathrm{Rf} = -B(z)/S(z) = -B_0(1 - z/h)/(\overline{u'w'}\partial u/\partial z + \overline{v'w'}\partial v/\partial z)$$

$$= -B_0(1 - \xi) / (u_*^3/L)\mathrm{Re}(\sigma^* s_v) \quad (* \text{ denotes complex conjugate})$$

Substituting (7) in for s_v, noting that by definition of Obuhkov length, $-B_0 = u_*^3/kL$, and that the eddy viscosity assumption implies that $\sigma^* s_v$ is guaranteed to be real, we obtain the nonlinear ODE

$$\sigma^* \partial^2\sigma/\partial\xi^2 = i\lambda(1 - \xi), \text{ where } \lambda = \gamma_c^2/k\mathrm{Rf} \text{ is unknown} \quad (8)$$

This equation can be solved systematically by substituting $\sigma = re^{i\theta}$ and obtaining a pair of ODEs for $r(\xi)$ and $\theta(\xi)$. However, an easier approach is to look for a trial solution in the form

$$\sigma(\xi) = -e^{i\alpha}(1 - \xi)^a$$

This solution automatically obeys the boundary conditions and has the right form to match the RHS of (10). Substituting into (10), we find that this trial solution works if

$$a^* + a - 2 = 1$$

$$a(a - 1) = i\lambda$$

Setting $a = a_r + ia_i$, the first of these equations implies that $a_r = 3/2$. From the second, we deduce that

$$0 = \mathrm{Re}[a(a - 1)] = \mathrm{Re}[(3/2 + ia_i)(1/2 + ia_i)] = 3/4 - a_i^2 \Rightarrow a_i = 3^{1/2}/2$$

$$\Rightarrow \sigma(\xi) = -e^{i\alpha}(1 - \xi)^{(3 + \sqrt{3})/2},$$

$$\lambda = \mathrm{Im}[a(a - 1)] = \mathrm{Im}[(3/2 + ia_i)(1/2 + ia_i)] = 2a_i = 3^{1/2} = \gamma_c^2/k\mathrm{Rf}$$

$$\Rightarrow \gamma_c = [3^{1/2}k\mathrm{Rf}]^{1/2} = 0.37 \quad \text{so} \quad h = 0.37(u_* L/f)^{1/2},$$

$$\Rightarrow s_v = i\gamma_c^{-2}\partial^2\sigma/\partial\xi^2 = -ia(a-1)\gamma_c^{-2}e^{i\alpha}(1 - \xi)^{(-1 + i\sqrt{3})/2}$$

$$= \lambda\gamma_c^{-2}e^{i\alpha}(1 - \xi)^{(-1 + i\sqrt{3})/2} \text{ is non-dim shear.}$$

$$\Rightarrow \kappa_m(\xi) = -\sigma/s_v = (1 - \xi)^2\gamma_c^2/\lambda = 0.08(1 - \xi)^2 \text{ is non-dim eddy viscosity}$$

Hence, remarkably we have been able to deduce the BL depth. There is one shortcoming, which is that L must still be deduced. The deduced eddy viscosity decreases with height to zero at the BL top, as we'd expect since turbulence is concentrated at the surface. The shear profile can be integrated from $\xi = 1$ ($z = h$) and the resulting velocity profile redimensionalized to obtain:

$$u + iv\Big|_h^z = -[u_* h/L][2\lambda\gamma_c^{-2}/(1 + i\sqrt{3})]\, e^{i\alpha}(1 - \xi)^{(1 + i\sqrt{3})/2}$$

At the BL top, the velocity is U_g. At the surface, the velocity is zero. Hence, setting $\xi = 0$ on the RHS, and noting that $(1 + i\sqrt{3})/2 = \exp(i\pi/3)$ and that we have:

$$u + iv\Big|_h^0 = -U_g = -[u_* h/L][\lambda\gamma_c^{-2}]\exp(i\alpha - i\pi/3) \quad (9)$$

For consistency the RHS must be real, and have the same magnitude as the LHS. Thus

$$\alpha = \pi/3 \quad \text{(surface isobaric wind turning angle of 60 degrees)} \quad (10)$$

$$U_g = [u_* h/L][\lambda\gamma_c^{-2}] = [u_* h/L][1/k\ \mathrm{Rf}] \quad (11)$$

Summary of Results and Comparison to Observations

PBL depth $h = \gamma_c(u_* L/f)^{1/2}$, where $\gamma_c = (3^{1/2}k\mathrm{Rf})^{1/2} = 0.37$

$$\underline{\text{Wind profile}}\ (u + iv)/U_g = 1 - (1 - z/h)^{(1 + i\sqrt{3})/2}$$

Note that h can be expressed in terms of the given parameters as:

$$h = 0.37(u_* L/f)^{1/2} = 0.37(-u_*^4/kB_0 f)^{1/2} = 0.37(-u_*^4/0.12kf^2U_g^2)^{1/2} = 1.7u_*^2/fU_g$$

A larger friction velocity, smaller geostrophic wind, or lower latitude will increase h. Also note that the wind profile is independent of the surface roughness (except in the surface layer $z << L$, where the assumed eddy scale of L is no longer applicable and (12) is invalid). The surface isobaric turning angle is 60 degrees, and the wind turns to geostrophic at the PBL top. We can solve (11) for the

$$\underline{\text{Obhukov length}}\ L = h\,(u_*/U_g)(1/k\ \text{Rf}) = 12.5h(u_*/U_g)$$

Substituting for h, this can also be written as

$$L = \gamma_c(u_* L/f)^{1/2}\,(u_*/U_g)(1/k\ \text{Rf})$$

or

$$L = (u_*^3/fU_g^2)(\gamma_c/k\ \text{Rf})^2$$

This can be used to deduce the surface buoyancy flux, which by definition of L is:

$$\underline{\text{Surface buoyancy flux}}\ B_0 = -u_*^3/kL = -0.12fU_g^2 \quad (\text{The constant is Rf}/3^{1/2})$$

Remarkably, the downward surface buoyancy flux is depends only on the geostrophic wind, and is independent of surface roughness.

The NBL structure obtained from this approach is fairly realistic. For reasonable values of u_* (0.3 m s^{-1}), U_g (10 m s^{-1}), and $f = 10^{-4}$ s^{-1}, we find that $h = 0.37(u_* L/f)^{1/2} = 150$ m, close to observed NBL depths of O(100 m). The Obhukov length $L = 56$ m, and $L/h \approx 0.38 << 1$, consistent with our original assumption that the vertical eddy mixing scale is much less than the PBL depth. The the downward surface buoyancy flux $B_0 = 1.2\times10^{-3}$ m^{2}s^{-3} (i. e. a virtual heat flux $(\rho c_p \theta_R/g)B_0 \approx -40$ W m^{-2}.) For $U_g = 5$ ms^{-1}, the downward buoyancy flux would be only 25% as large as this. These are not a large heat flux; atmospheric turbulence cannot keep the ground from cooling rapidly at night under clear skies unless the geostrophic wind is large. Instead, ground heat flux is the major counterbalance to nocturnal radiative cooling. The surface energy budgets (e. g. over a dry lake bed) nicely showed the fairly small role of surface heat fluxes in the nocturnal boundary layer.

The NBL stratification can also be deduced.

$$db/dz = N^2 = \text{Ri}|d\mathbf{u}/dz|^2 = \text{Ri}[u_*/L]^2|s_v|^2 = (\text{Ri}/k^2\text{Rf}^2)(u_*/L)^2(1 - z/h)^{-1}$$

Since Ri = Rf = 0.2, the constant is $1/k^2\text{Rf} = 31$. Integrating with respect to z, we obtain

$$b(z) - b(0) = -31h(u_*/L)^2 \ln(1 - \xi)$$

This has a singularity at the BL top, which is a bit disturbing, but relates to the assumption that there must be uniform cooling all the way to the BL top, even though there is very little turbulence near the BL top. The small turbulent diffusivity then requires a large gradient there. For our example values, $N^2 = 9\times10^{-4}$ s^{-2} (2.6 K per 100 m) at the surface, rising with height. To get a more stable BL than this, we must have diabatic (e. g. radiative) cooling within the BL.

A comparison of this theory to observations is shown in the figure on the next page. It should

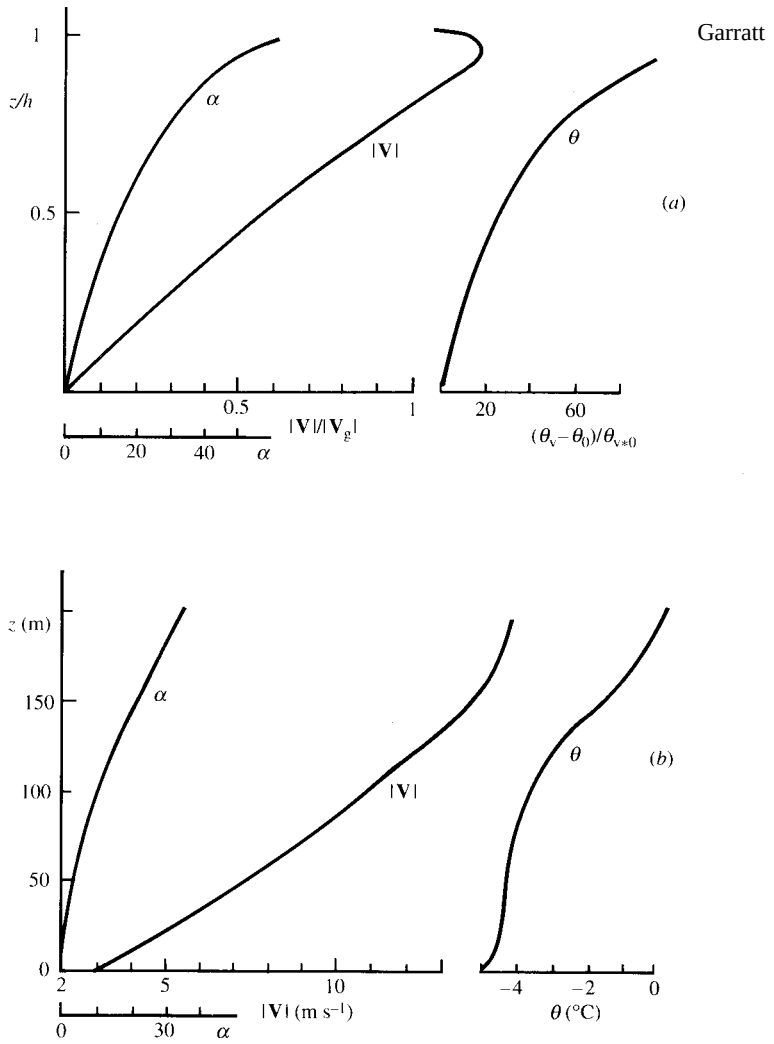

Fig. 6.15 (*a*) Predicted values of cross-isobar flow and normalized wind speed (Eq. 6.68) and of normalized temperature difference (Eq. 6.69) as functions of normalized height. (*b*) Observations from Cabaow of cross-isobar flow angle, wind speed and temperature as functions of height in the NBL. From Nieuwstadt (1985), by permission of the Oxford University Press.

Comparison of steady NBL theory (top) with tower observations (bottom) in a case of strong geostrophic wind.

be noted that this case has a high geostrophic wind speed, so that the surface buoyancy flux is large and the relative importance of radiative cooling in the NBL dynamics is smaller than usual. The comparison is quite good under these conditions. The predicted linear increase of wind with height in the BL and the concentration of the wind turning at the BL top are both observed. The observed wind turning of 30 is less than predicted, however. As predicted the strongest stratification is near the BL top. Normally, however, the NBL is most strongly stratified near the ground where clear-air radiative cooling is strongest, as seen in other soundings in these notes.

The one step in applying this approach that we have not discussed is how to relate u_* to U_g and the surface roughness z_0. The velocity profile deduced above linearly approaches zero at the surface, rather than the log-linear behavior of M-O theory. Empirical formulas, given on pp. 63-64

of Garratt, can be used to relate u_* to U_g. They are given in terms of two functions $A_2(\mu)$ and $B_2(\mu)$ of $\mu = h/L$, and are typically expressed in coordinates parallel to the surface wind. Translating these formulas into our notation, we find

$$C_g = (u_*/ U_g)^2 = k^2/[(\ln(h/z_0) - A_2)^2 + B_2^2] \quad (12)$$

where for moderately stable conditions ($0 < \mu < 35$), Garratt's eqn (3.89) implies that

$$A_2 = 1 - 0.38\mu, \quad B_2 = 4.5 + 0.3\mu.$$

For our example, $C_g = (u_*/ U_g)^2 = 0.0009$, and $\mu = 2.7$, so $A_2 = -0.0$, $B_2 = 5.3$. The surface roughness that could give this NBL is found by solving (13):

$$(\ln(h/z_0) - A_2)^2 + B_2^2 = k^2/C_g$$

$$\Rightarrow \ln(h/z_0) = -A_2 + [k^2/C_g - B_2^2]^{1/2} = 12.2 \quad , \; z_0 \approx 0.001 \text{ m}$$

(typical of flow over a smooth land surface such as sand). A change in z_0 of several orders of magnitude is necessary to move u_* up or down by 50% for a given geostrophic wind speed.

KatabaticFlows

Sloping terrain has a large influence on stable boundary layers. The cold dense air near the surface is now accelerated by the downslope component $b \sin\alpha$ of its buoyant acceleration (α is the slope angle and $b < 0$ is the buoyancy of air within the BL relative to above-BL air at the same height). Viewed in terrain-parallel coordinates, $b \sin\alpha$ is like an effective pressure gradient force, which is strongly height-dependent since b depends on z. In this sense, the slope acts similar to a thermal wind (which would also be associated with a height dependent PGF) . Slopes of as little as 2 in 1000 can have an impact on the BL scaling.

As the slope increases, or BL stability increases, the velocity profile is increasingly determined by drag created by turbulent mixing with air above rather than surface drag. As for the NBL, the BL is typically 10s to 100s of m thick. Over glaciers, katabatic winds often occur during the day as well as during the night, since the net radiation balance of a high-albedo surface is negative even during much of the day, and evaporative cooling due to surface snowmelt can also stabilize the air near the surface. On the coast of Antarctica, persistent katabatic flows down from the interior ice-caps can produce surface winds in excess of 50 m s^{-1}.

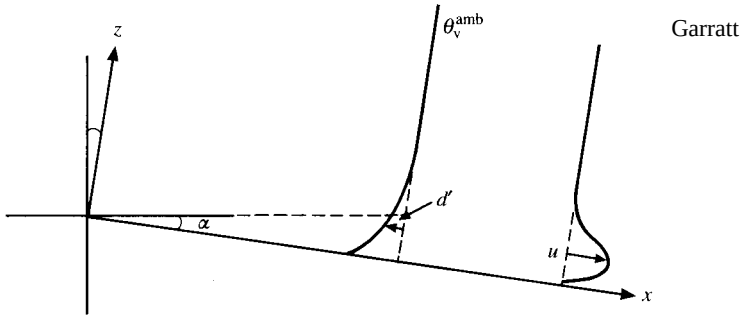

Fig. 6.22 Schematic representation of the downslope flow typical of night-time flow under light wind, clear sky conditions. Here, α is the slope angle and d' is the θ deficit of the flow relative to the ambient field.

Lecture 14. Marine and cloud-topped boundary layers

Marine Boundary Layers (Garratt 6.3)

Marine boundary layers typically differ from BLs over land surfaces in the following ways:

(a) Near surface air is moist, with a typical RH of 75-100%

(b) The diurnal cycle tends to be weak (though not negligible), since surface energy fluxes get distributed over a considerable depth (10-100+) of water, which has a heat capacity as much as hundreds of times as large as the atmospheric BL.

(c) Air-sea temperature differences tend to be small, except near coasts. The air tends to be 0-2 K cooler than the water. This is because the BL air is usually radiatively cooling, and some of this heat is supplied by sensible heat fluxes off the ocean surface. However, if the air temperature is much lower than the SST, vigorous convection will reduce the temperature difference, and except where there are large horizontal gradients in SST, horizontal advection cannot maintain the imbalance. Hence the surface layer is nearly neutral over almost all of the oceans.

(d) Due to the small air-sea temperature difference, the Bowen ratio tends to be small (typically 0.1 in the tropical oceans, and more variable in midlatitudes); latent heat fluxes are 50-200 W $m^{-2,}$, while (except in cold air outbreaks off cold landmasses) sensible heat fluxes are 0-30 W m^{-2}.

(e) Over 95% of marine boundary layers contain cloud. The only exceptions are near coasts, where warm, dry continental air is advected over a colder ocean, and in some regions (such as the eastern equatorial Pacific cold tongue and some western parts of the major subtropical oceans) in which air is advecting from warmer to colder SST, tending to produce a more stable shear-driven BL which does not deepen to the LCL of surface air. Cloud profoundly affects the BL dynamics, as we discuss below.

Many large field experiments have studied marine BLs. Particular focus areas, and particularly seminal field experiments, have included:

(i) Tropical BLs associated with deep convection (GATE 1973, tropical E Atlantic; TOGA-COARE 1992, tropical W Pacific)

(ii) Trade cumulus boundary layers (BOMEX 1969, Caribbean; ATEX 1973, tropical E Atlantic)

(iii) Subtropical stratocumulus-capped BLs (FIRE-MSC 1987, California; ASTEX 1992, NE Atlantic; DYCOMS-II 2001, NE Pacific; EPIC-2001, SE Pacific)

(iv) Midlatitude summertime BLs (JASIN 1978, NE Atlantic)

(v) Midlatitude wintertime BLs (AMTEX 1974, S China Sea; MASEX 1983, Atlantic Coast)

(vi) Arctic stratus (Arctic Stratus Experiment 1980, BASE 1994, SHEBA/FIRE.ACE 1997-8)

While there are interesting issues associated with the formation of stable cloudless marine boundary layers due to advection of air off a continent (see Garratt 6.4), the study of marine boundary layers largely comprises an important subset of the study of cloud-topped boundary layers, to which we turn now.

Cloud-topped boundary layers (Garratt, Ch. 7)

Regimes and geographical distribution

Over much of the globe, and in particular over most of the oceans, low-lying cloud plays a key role in BL dynamics. Cloud affects boundary layer dynamics through latent heating, evaporation of precipitation into layers beneath the cloud, and through large changes in the radiative balance of both the BL itself and the underlying surface

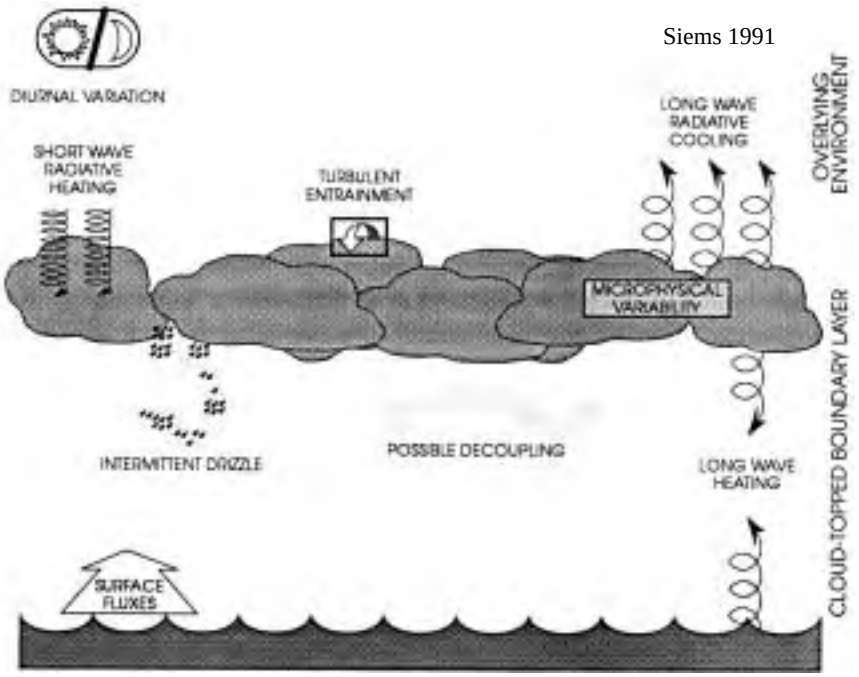

Processes affecting convective cloud-topped BLs

The most commonly seen cloudy BL types include:

(i) Shallow cumulus (Cu) boundary layers, ubiquitous over oceanic trade-wind regimes, but often seen over land and midlatitude oceans as the later phase of cold air outbreaks. These are driven primarily by clear-air radiative cooling

(ii) Stratocumulus (Sc)-capped BLs, typically found in anticyclonic flow over the subtropical and midlatitude oceans, and often seen during the cool season over moister landmasses. These BLs may include Cu below or rising into the Sc, and are driven in large part by radiative cooling at the tops of the clouds, and secondarily by surface cold advection.

(iii) The progression in a wintertime cold air outbreak from shallow cloud streets to broader patches and lines of Sc and finally polygonal arrays of Cu. The BL is driven by strong surface heat fluxes of up to several hundred W m^{-2}.

(iv) Shear-driven shallow stratus layers, often seen in midlatitudes in warm advection. Here the dynamical and radiative effects of the cloud are probably secondary, since there are often overlying clouds that reduce the radiative impact of the low cloud, and the BL is not deep enough for the latent heating in the clouds to be important. There may be low cloud and rain that does not have a clear associating with BL processes associated with synoptic-scale lifting.

(v) Summertime arctic stratus under a weak anticyclone, in which there may be multiple cloud layers driven by surface chilling of and cloud top radiative cooling of moist, warm air advected over cold pack ice.

The global distribution of low cloud (at heights of 2 km or less above the surface) is best documented in routine synoptic observations of cloud type and cover by untrained surface observers using a simple classification scheme from WMO. These have been archived over the past 50 years, and were compiled by Warren et al. (1988). Below are shown the annually averaged cloud cover (frequency of occurrence multiplied by fractional sky cover when cloud type is present) for low lying 'stratus' (stratus+stratocumulus+fog), which encompasses the most radiatively important cloud types, and for cumulus cloud. These cloud layers are typically 100-500 m thick, with a cloud base anywhere from the surface to 1500 m, and tend to be nonprecipitating. Over much of the midlatitude oceans and parts of the eastern subtropical oceans, stratus cloud cover exceeds 50%.

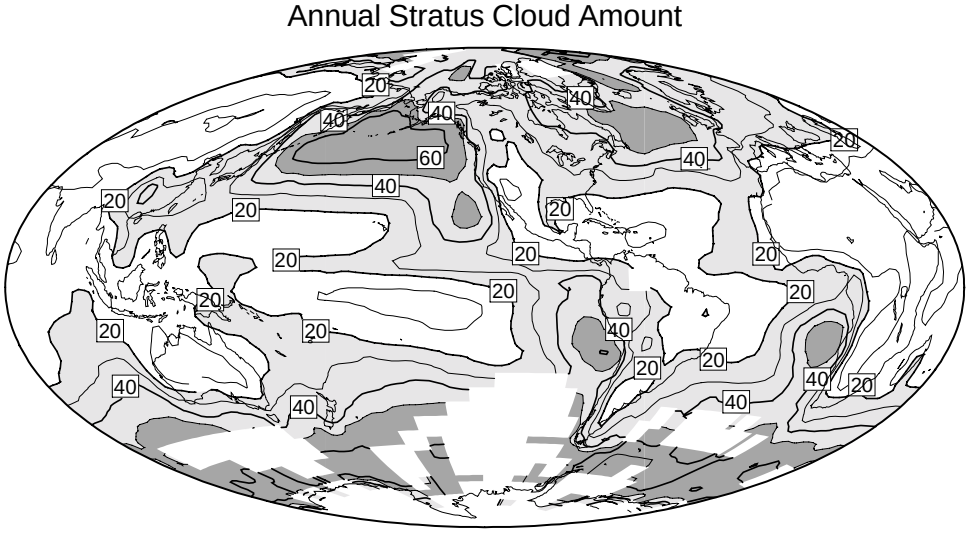

Klein and Hartmann (1993), from surface observations

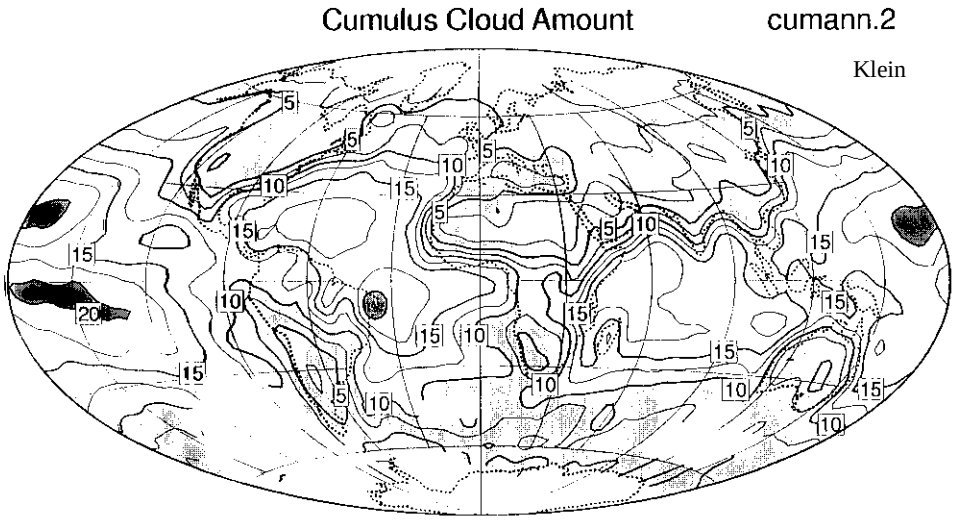

Klein and Hartmann (1993) showed that the cloud cover in these regions is highest when the sea-surface is coldest compared to the air above the boundary layer, which tends to occur in the summertime. In some parts of the Aleutian Islands, the average stratus cloud cover in June, July and August is 90%...a dreary sky indeed. Over land, there is much less stratus cloud due to the lesser availability of surface water. In most of the tropical and subtropical oceans, stratus clouds are rare. There is a very strong correlation between TOA cloud radiative forcing and stratus cloud amount due to the high albedo of these clouds, coupled with the smallness of their greenhouse effect since being low clouds, they are at a similar temperature to the underlying surface. There is an obvious correlation between cumulus cloud and a relatively warm surface. Note that cumulus cloud amount is everywhere low, even though over much of the trade wind belts, the frequency of occurrence is 70-90%. More than 100-200 km offshore, a complete lack of BL cloud is rare, occuring 1-2% of the time in most ocean locations.

BL structure of subtropical convective CTBLs

The figure above shows composite soundings from four field experiments that studied marine subtropical and tropical CTBLs (Albrecht et al. 1995). The experiments were conducted over locations with very different sea-surface temperature (SST).The typical observed boundary layer cloud structure and circulations are sketched. The experiments are FIRE SNI (July 1987, 33 N, 120 W, SST = 289 K, Cloud Fraction = 0.83), ASTEX (June 1992, SM:
37 N, 25 W, SST = 291 K, CF = 0.67; VALD: 28 N, 24 W, SST = 294 K, CF = 0.40),), and TIWE (December 1991, 0 N, 140 W, SST = 300 K, CF = 0.26).

The deeper BLs tend to have less cloud cover, a weaker inversion, and a less well-mixed structure in the total water mixing ratio $q_t = q_v + q_l$ (which is conserved following fluid motions in the absence of mixing). The stratification of θ_v is roughly dry-adiabatic below cloud base. In the cloud layer, it is moist-adiabatic within the shallow FIRE stratocumulus cloud layer and conditionally unstable in the other cases. In general, one can identify three types of BL structure:
(i) well-mixed (e. g. FIRE-SNI). A specific example is shown on the next page
(ii) diurnally decoupled (some daytime shallow Sc layers), in which there are well-mixed surface and cloud layers separated by a stable layer across which there is no turbulent transport. An example is shown on next page.
(iii) conditionally unstable, in which a well-mixed subcloud layer is topped by cumulus clouds, and

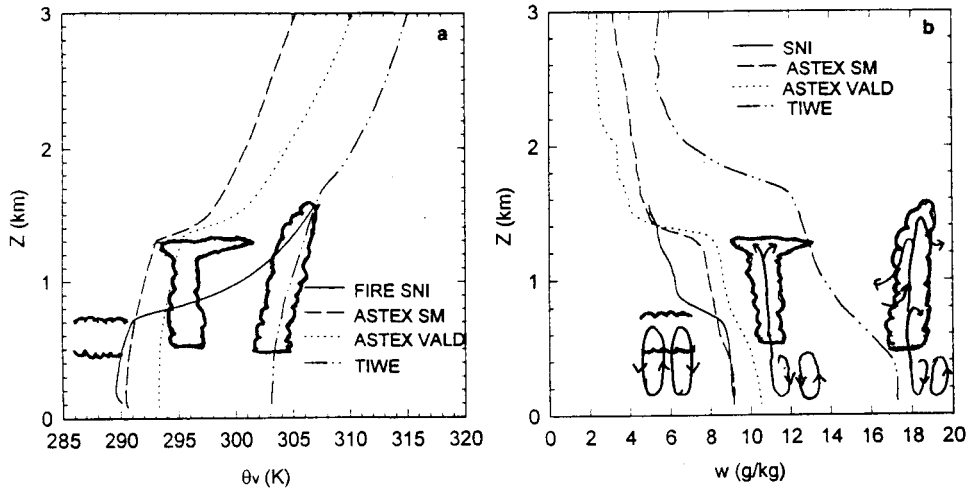

Composite θ_v and q_t from four CTBL experiments (Albrecht et al. 1995)

there may or may not be a thin stratocumulus layer below the capping inversion formed by detrainment from the cumuli. There is a very weak (< 1 K) inversion at the base of the cumuli called the transition layer that separates the region of subcloud convection below cloud base from the drier cumulus layer above. Essentially, the transition layer acts as a valve to allow only the strongest subcloud updrafts to form cumulus clouds. The capping inversion tends to be sharp if there is more Sc cloud (see figure on next page) and extends over 100-500 m if only Cu is present.

In the deep convective regions of the tropics, conditionally unstable cumulus boundary layers are also often seen extending up to around 800 mb when deep convection is suppressed. A capping inversion is not evident around deep convection; here the BL is complicated by internal BLs as shallow as 100 m due to cold dry outflow from deep convective systems. Even over a uniform sea-surface, mesoscale temperature variationsof 3-5 K are common in this situation. Surface fluxes restore the outflow air to a typical non-outflow thermodynamic state in 6-24 hrs.

Over midlatitudes, when stratocumulus or cumulus cloud is observed the soundings again fall into the above categories (Norris 1998). However, the RH of surface air may be lower and hence the depth of the subcloud layer may be as much as 1500 m, especially over land.

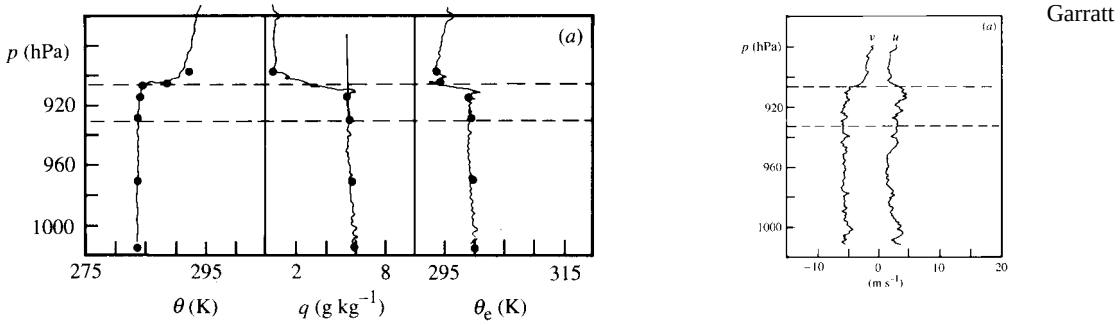

Garratt

Well-mixed Sc layer

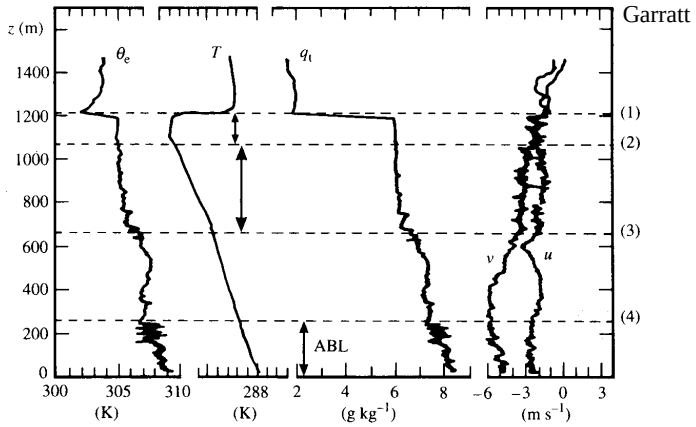

Garratt

Fig. 7.5 Observed mean profiles of thermodynamic variables and wind components made in the CTBL over the ocean during JASIN, for a decoupled stratocumulus layer. The pecked horizontal lines delineate layer boundaries as follows: (1) cloud top; (2) cloud base; (3) bottom of subcloud layer; (4) top of the surface-related Ekman layer. After Nicholls and Leighton (1986), *Quarterly Journal of the Royal Meteorological Society*.

Decoupled Sc layer

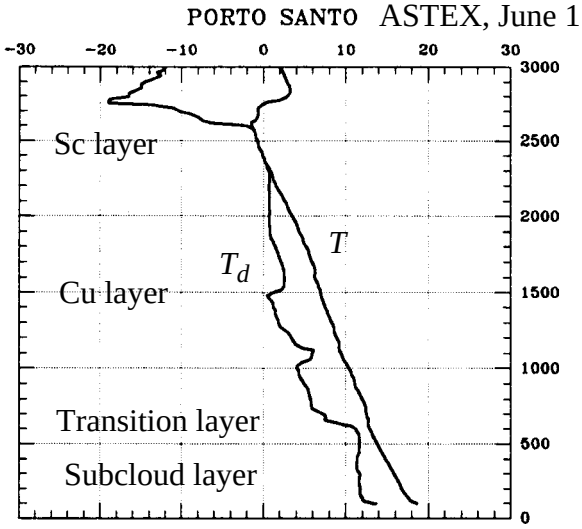

Conditionally unstable sounding with shallow Cu rising into an Sc layer

Stable CTBLs

Some cloud types (such as stratus and fog) are associated with stable BLs. Norris (1998) has used soundings from ocean weather ships taken during the 1970s to form composites for different cloud types. In these cases, the sounding is absolutely stable and the presence of cloud just reduces the effective stability. We will not discuss these BLs more, as the impact of cloud on convective BLs is more profound, especially when surface sensible heat fluxes are weak as they usually are over the ocean

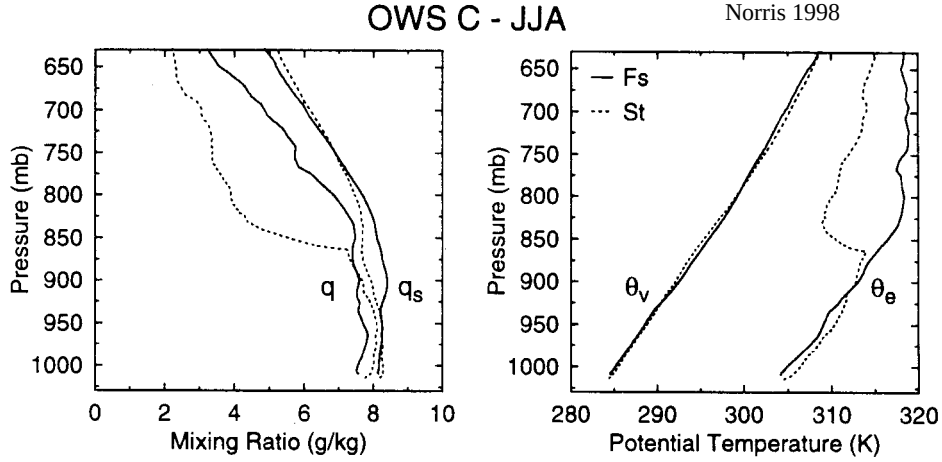

Composite profiles for stratus (St) and fractostratus (Fs)-capped (stable) CTBLs.at Ocean Weathership C in the N Atlantic Ocean.

Lecture 15. Subtropical stratocumulus-capped boundary layers

In this lecture…

- Physical processes and their impact on Sc boundary layer structure
- Mixed-layer modeling of Sc-capped boundary layers – methods and results

Physical processes and their impact on Sc boundary layer structure

Clear turbulent boundary layers over land are usually driven mainly by surface heat fluxes or drag. Stratocumulus-capped boundary layers (SCBLs) are more complicated (Fig. 1). The cloud usually forms because turbulence lifts moist air from near the surface up to its condensation level. The cloud plays an active role in maintaining the turbulence and building a sharp, strong capping inversion. Radiative cooling at cloud top and heating within the cloud, as well as latent heating due to condensation or evaporation of cloud and drizzle all have strong feedbacks on the boundary-layer structure and turbulence. The strong capping inversion inhibits turbulent mixing or entrainment of the warmer and drier overlying air into the SCBL. This keeps the boundary layer cool and moist, helping the cloud persist. A strong capping inversion goes with more lower tropospheric stability, and also keeps the boundary layer moist and cloud-capped. This is a major reason for the observed correlation between lower tropospheric stability and stratus cloudiness.

Moist-conserved variables

In the study of MBLs, it is often useful to work with moist-conserved variables preserved during adiabatic changes including phase changes between vapor and liquid, e. g. the total water mixing ratio $q_t = q_v + q_l$ (sum of vapor and liquid water). Moist-conserved temperature-like variables include the equivalent potential temperature $\theta_e \approx \theta \exp(Lq_v/c_pT_{LCL})$ (see Bolton 1980 for a more accurate definition) and the liquid water potential temperature $\theta_l = \theta \exp(-Lq_l/c_pT_{LCL})$. If the parcel vertical displacement is nearly hydrostatic (a good approximation for the MBL), one can instead use simpler moist-conserved variables, the moist static energy $h = c_pT + gz + Lq_v$, or the liquid-water static energy $s_l = c_pT + gz - Lq_l$. All four of these choices are commonly used in studies of SCBLs.

As an air parcel rises moist-adiabatically above its lifted condensation level (LCL), it becomes cloudy and condenses liquid water at a rate $(dq_l/dz)_{ma} = -(dq^*/dz)_{ma} \approx 2$ g kg^{-1} km^{-1} for thermodynamic conditions typical for Sc (cloud base temperature of 285 K, cloud base pressure of 950 hPa). Here, 'ma' stands for 'moist adiabatic'.

Mixed-layer structure

SCBLs commonly exhibit mixed-layer structure in which moist-conserved thermodynamic variables and the horizontal velocity components are approximately uniform with height. This is a sign of strong vertical mixing by turbulent eddies extending from the surface all the way to the cloud-top. In SCBLs, the eddy updrafts and downdrafts are typically on the order of 1 m s^{-1}.

Fig. 2 shows an example from the DYCOMS-II field experiment off the California coast in July 2001 (satellite picture and map showing flight track and sea-surface temperature are at upper right). Several aircraft profiles through the same cloud layer a few tens of km apart are shown. One sees well-mixed structure in q_t and s_l, and the linear rise of q_l with height above

cloud base. These measurements were all taken during the night and early morning. This time of day favors well-mixed SCBLs, as we'll explain soon. We also see the strong (10 K), sharp inversion separating the cool marine airmass from the much warmer and very dry air above, which has slowly subsided from much higher in the troposphere in the descending branch of the Hadley circulation.

Decoupled structure and the diurnal cycle

Fig. 3 shows 'decoupled' vertical structure in θ_e, q_t, and the wind components. This is also commonly seen in SCBLs, especially during mid-day – these aircraft profiles were made near noon in North Atlantic summer stratocumulus. The SCBL is separated into two mixed layers, one starting at the surface, and one extending down from the cloud layer, with a stratified layer in between. In this middle layer, there is little turbulence (visible in the slide as less fine-scale vertical variability). 'Scud' clouds can sometimes.form at the top of the surface mixed layer. Given long enough, these clouds can develop into cumulus convection, leading to a 'cumulus-coupled' SCBL in which cumulus convection fluxes moisture from the lower to the upper mixed layer.

Fig. 4 shows a 6-day time series of radiosonde profiles from the October 2001 EPIC research cruise into the SE Pacific stratocumulus region. These nicely show a pronounced diurnal cycle. The difference between cloud base and near-surface LCL (measured by the ship at a height of 15 m above sea level) is a good measure of decoupling. It would be zero in an ideal mixed layer, in which the near-surface air had exactly the same properties as cloud base air. This is never seen, because in the surface layer (lowest 5-10% of the BL) there is a 'log-layer' in which air properties transition from those in the bulk of the boundary layer and the saturated air in a mm thick skin next to the sea-surface.) However, smaller values (less than 10-15% of the cloud base height) indicate a mixed layer, and larger values (more than 250 m) indicate a more decoupled boundary layer in which the surface air is distinctly moister than that in the cloud layer. This measure shows mixed-layer structure at night and slightly decoupled structure during the day (noon local time = 18 UTC) as well as during periods of drizzle.

Radiation

The SCBL interacts strongly with longwave and shortwave radiation. Clouds as little as 50 m thick efficiently absorb and emit longwave radiation. Although the clouds mainly scatter sunlight, they also absorb a little of it. The upper left figure in Fig. 5 shows a comparison of measurements and radiative transfer model calculations for a thick summertime North Sea stratocumulus cloud around noon. The symbols S and L refer to shortwave and longwave radiation, and arrows indicate upward and downward fluxes. About 2/3 of the incident sunlight is reflected, but about 60 W m^{-2} (6%) is absorbed in the cloud. Upwelling longwave radiation emitted from the warm cloud top is almost 100 W m^{-2} larger than downwelling longwave radiation emitted by the dry and mostly colder overlying atmosphere. Within the cloud, the photon path is short and the net longwave flux is small, while below cloud base, there is a net upward longwave flux of about 10 W m^{-2} because the SST slightly exceeds the cloud base temperature.

Combining longwave and shortwave fluxes, we get the net upward radiative flux during the middle of the day. From just the longwave flux, we get the net upward radiative flux at night. (middle figures). The dashed line in the night-time panel shows the daily-averaged net upward radiative flux. Vertical convergence or divergence of the net radiative flux implies radiative heating or cooling, respectively. During the night, the flux profile implies slight radiative warming near cloud base and strong cooling in the 50 m below cloud top, with a net

60 W m^{-2} longwave cooling integrated over the SCBL in the case shown. During the daytime, the additional absorption of sunlight warms most of the cloud layer, but the strong longwave cooling still dominates at the cloud top. The 60 W m^{-2} of solar absorption roughly cancel the SCBL longwave cooling, so the effect of radiation at noon is only to destabilize the cloud layer, not the entire boundary layer. This is what causes daytime decoupling of SCBLs – surface heat fluxes cause convection near the sea-surface, and radiation causes convection in the cloud. Averaged over the whole diurnal cycle, the net longwave cooling of the SCBL is roughly 3-4 times as large as net solar heating, and radiation is strongly destabilizing the SCBL by cooling its top. This is the main driver of turbulent convection in subtropical SCBLs. The diurnal cycle of SCBL radiative energy loss is shown at lower right, where it is also compared to a typical value of surface sensible heat flux over the subtropical oceans. This plot suggests that in subtropical SCBLs, radiation is more important to the energy budget and generation of turbulence than is the surface heat flux. The strong radiative cooling also helps maintain the sharp 5-10 K inversions that usually top such boundary layers.

Theoretical studies of cloud-topped mixed layers sometimes treat the radiative flux divergence as concentrated entirely at the cloud top, and often specify it as an external parameter $\Delta R_N \approx 50$ W m^{-2} (rightmost profile). In reality, of course, ΔR_N is strongly dependent on above-SCBL humidity, cloud and temperature, as well as cloud-top temperature and insolation. In particular, ΔR_N is largest under a clear, dry atmospheric column.

Precipitation

Because stratocumulus are thin and rely on the surface for their supply of liquid water, they can be sensitive to even a little precipitation. Precipitation in stratocumulus can be somewhat artificially divided into droplet sedimentation and drizzle. Sedimentation is the slow settling of 'cloud' droplets less than 20 μm in radius. It occurs only within the cloud, but can result in downward water fluxes of several mm/day, which proves important for the water budget of the upper part of the cloud layer. Drizzle is the settling of larger drops created by collision-coalescence processes, and tends to be dominated by drops 100 μm and larger. Drizzle tends to maximize near cloud base, and rapidly evaporates below the cloud. Light drizzle is sometimes observed in shallow cloud-topped boundary layers, especially when aerosol concentrations are low or the cloud is thick (which is most common in the night and early morning).

Fig. 6 shows typical profiles of sedimentation and drizzle to the downward precipitation flux in a moderately drizzling Sc, corresponding to cloud base precipitation of 2 mm day^{-1} and surface precipitation of 0.25 mm day^{-1}. Sedimentation removes liquid water from the top of the cloud, forcing turbulence to lift it up again. This decreases entrainment (see Bretherton et al. 2007 for a detailed explanation) and tends to reduce turbulence in the cloud layer. Drizzle causes net condensation and latent heating in the cloud layer and evaporation and cooling of the subcloud layer, stabilizing the BL to convection. Often, drizzling shallow Sc layers are observed to have some stratification of potential temperature and mixing ratio, and cloud cover may be less homogeneous. Both sedimentation and drizzle are much larger when aerosol (and hence cloud droplet) concentrations are low. Thus, these processes are important to understanding the effects on anthropogenic aerosols on SCBLs and climate.

The bottom of Fig. 6 shows a 6-day time-height section of mm-wavelength upward-pointing radar returns from SE Pacific stratocumulus during the EPIC cruise. Reflectivities less than -10 dBZ correspond to nearly non-drizzling cloud; stronger reflectivities indicate drizzle. When the drizzle is weak, it all evaporates near cloud base; when the drizzle is

strong it gets down to the surface. A strong diurnal cycle of drizzle is evident, connected to night-time cloud thickening.

Entrainment

Entrainment is the incorporation of filaments or blobs of overlying non-turbulent air into the SCBL by turbulent eddies. Entrainment occurs in a thin entrainment zone near the cloud-top. Over boundary layer updrafts, the entrainment zone is thin (as little as 1 m thick), and it is thicker (up to 100 m) in downdraft regions, especially if the inversion is weak or there is a lot of wind shear at the inversion. The physical mechanisms are somewhat complicated and the cloud itself affects the entrainment process through evaporative cooling –we'll discuss this more later when we talk about entrainment closures. What is clear is that entrainment is faster if the turbulence is stronger or the overlying inversion is weaker. For now, we simply define the entrainment rate w_e, which is the rate at which overlying air is incorporated into the SCBL. For subtropical SCBLs, w_e is usually only a few mm s^{-1}.

Consider a variable F with no sources or sinks in a thin entrainment zone, and a typical value F^- below the entrainment zone and F^+ above the entrainment zone (Fig. 7, top right). The flux - $w_e F^+$ of F through the top of entrainment zone must balance the flux of F through the bottom of the entrainment zone (which has a mean component - $w_e F^-$ and a turbulent component). We deduce that a turbulent entrainment flux

$$\overline{w'F'}\Big|_e = -w_e \Delta F \ , \ \Delta F = F^+ - F^- \qquad (15.0)$$

is needed to mix the entrained air into the SCBL.

Using (15.0), we can deduce entrainment from aircraft measurements of the below-inversion flux and cross-inversion jump of suitable variables. Total water, ozone, and DMS have been successfully used for this purpose. Alternatively, we can derive a heat, moisture or mass budget for the entire SCBL, deduce the entrainment flux by measuring all other terms in the budget, and then apply the flux-jump approach. Fig. 7 shows an example of this approach, in which we see reasonable consistency between the diurnal cycle of entrainment deduced from heat, moisture and mass budgets during a 6-day period in SE Pacific stratocumulus (Caldwell and Bretherton 2005). This approach works because entrainment is a dominant term in all three budgets.

References

Albrecht, B. A., R. S. Penc, and W. H. Schubert, 1985: An observational study of cloud-topped mixed layers. *J. Atmos. Sci.*, **42**, 800-822.

Bolton, D., 1980: The computation of equivalent potential temperature. *Mon. Wea. Rev.*, **108**, 1046-1053.

Bretherton, C. S., 1997: Convection in stratocumulus-capped atmospheric boundary layers. In *The Physics and Parameterization of Moist Atmospheric Convection*, R. K. Smith, ed., Kluwer Publishers, 127-142Breth et al. 2004

Bretherton, C. S., T. Uttal, C. W. Fairall, S. Yuter, R. Weller, D. Baumgardner, K. Comstock, and R. Wood, 2004: The EPIC 2001 stratocumulus study. *Bull. Amer. Meteor. Soc.*, **85**, 967-977.

Bretherton, C. S., P. N. Blossey, and J. Uchida, 2007: Cloud droplet sedimentation, entrainment efficiency, and subtropical stratocumulus albedo. *Geophys. Res. Lett.*, 34, L03813, doi:10.1029/2006GL027648.

Caldwell, P., C. S. Bretherton, and R. Wood, 2005: Mixed-layer budget analysis of the diurnal cycle of entrainment in SE Pacific stratocumulus. *J. Atmos. Sci.*, **62**, 3775-3791.

Comstock, K. K., R. Wood, S. E. Yuter, and C. S. Bretherton, 2004: Reflectivity and rain rate in and below drizzling stratocumulus. *Quart. J. Roy. Meteorol. Soc.*, **130**, 2891-2918.

Nicholls, S., 1984: The dynamics of stratocumulus: aircraft observations and comparisons with a mixed layer model. *Quart. J. Roy. Meteor. Soc.*, **110**, 783-820.

Stevens et al. 2003: On entrainment rates in nocturnal marine stratocumulus. *Quart. J. Roy. Meteor. Soc.*, **129**, 3469-3493.

Mixed-layer modeling of stratocumulus-capped boundary layers

Mixed-layer modeling of stratocumulus was introduced in a classic paper by Lilly (1968). and has since been used in many scientific papers about SCBLs. It is not just useful for predictive modeling, but also for interpretation of observations and more complex models. A mixed-layer model is only appropriate if the SCBL is indeed well-mixed, so a MLM should be able to predict when it has reached its limit of validity (see Bretherton and Wyant 1997 for a discussion of this).

There are several complications in mixed-layer modeling of stratocumulus that are not present in a dry convective boundary layer. These include internal heating and cooling of the boundary layer by condensation, evaporation and radiation. There is also still controversy about the appropriate entrainment closure.

Deducing the cloud properties in a stratocumulus-capped mixed layer

The thermodynamic state of a stratocumulus-capped mixed layer is most easily specified in terms of two moist-conserved variables, for instance the moist static energy h_M and the total water mixing ratio q_{tM}. The mixed-layer assumption is that vigorous turbulence keeps these variables vertically uniform between the surface and the inversion height $z_i(t)$.

Quantities that are not moist-conserved, such as temperature or liquid water content, are not vertically uniform within the mixed layer; their vertical profiles must be deduced from h_M and q_{tM} and pressure $p(z)$. As for the dry mixed layer, we will neglect variations of density ρ with height within the boundary layer. We also specify the surface pressure p_s. Then the hydrostatic approximation applied to the mean state implies that

$$p(z) = p_s - \rho g z. \tag{15.1}$$

Particularly important is the cloud base height z_b, at which boundary layer air is exactly saturated. It can be calculate from the equation:

$$q_{tM} = q^*(p_b, T_b) = q^*(p_s - \rho g z_b, \ [h_M - g z_b - L q_{tM}]/c_p) \ . \tag{15.2}$$

Here $q^*(p, T)$ is the saturation water vapor mixing ratio, and subscript 'b' refers to the cloud base. This nonlinear equation can be solved for z_b in terms of known quantities. Although this looks complicated, it can be approximated by a simpler linear form. We define the mixed layer air temperature at the surface z=0:

$$T_{Ms} = [h_M - L q_{tM}]/c_p, \tag{15.3}$$

and we define the mixed layer saturation mixing ratio at z=0:

$$q^*_{Ms} = q^*(p_s, T_{Ms}). \tag{15.4}$$

We can then linearize the right hand side of (15.2) in z_b around this saturated state:

$$q^*(p_b, T_b) = q^*_{Ms} + z_b (dq^*/dz)_{da}. \tag{15.5}$$

Here $(dq^*/dz)_{da}$ is the rate at which saturation mixing ratio changes with height along a dry adiabat from the surface to the cloud base. This depends on the exact thermodynamic state, but for thermodynamic conditions typical of subtropical stratocumulus,

$(dq^*/dz)_{da} \approx$ - 4 g kg^{-1} km^{-1}. Hence, (15.2) simplifies to

$$z_b \approx (q^*_{Ms} - q_{tM}) / |dq^*/dz|_{da} \tag{15.6}$$

If the surface air is more subsaturated, z_b will be larger. A good approximation is that if the near-surface relative humidity is 80%, the cloud base (= lifted condensation level) will be about 500 m. If the near surface RH is 60%, the cloud base will be 1 km, etc. Above the cloud base, similar linearization gives the liquid water profile

$$q_l(z) = q_{tM} - q^*(p_M(z), T_M(z)) \approx |dq^*/dz|_{ma}(z - z_b), \tag{15.7}$$

where $(dq^*/dz)_{ma}$ is the rate at which saturation mixing ratio changes with height above cloud base along a moist adiabat. Typically $|dq^*/dz|_{ma} \approx$ 2 g kg^{-1} km^{-1} is about half as large as $|dq^*/dz|_{da}$ in a stratocumulus layer. We see that the liquid water content is largest at the cloud top, and that the vertically-integrated cloud liquid water content, or liquid water path, is proportional to the square of the cloud layer depth. An adiabatic subtropical stratocumulus cloud about 300 m thick has a cloud-top liquid water content of 0.6 g kg^{-1} and a liquid water path of about 100 g m^{-2}.

Fig. 8 (left) shows how various profiles behave in a stratocumulus-capped mixed layer.

MLM equations

Above the boundary layer, we assume known 'free-tropospheric' profiles $q_t^+(z)$, $h^+(z)$. These affect the entrainment flux into the mixed layer:

$$\overline{w'q_t'}(z_i) = -w_e \Delta q_t, \qquad \Delta q_t = q^+(z_i) - q_{tM}, \tag{15.8a}$$

$$\overline{w'h'}(z_i) = -w_e \Delta h, \qquad \Delta h = h^+(z_i) - h_{tM}. \tag{15.8b}$$

Since stratocumulus evolve slowly, we must also consider the mean vertical velocity $\bar{w}(z)$, which is often idealized as subsidence that increases linearly with height:

$$\bar{w}(z) = -Dz, \tag{15.9}$$

where D is the horizontal wind divergence, typically 3-6$\times 10^{-6}$ s^{-1} in subtropical stratocumulus regimes. Thus, at a height of 1 km, the mean subsidence rate is around 3-6 mm s^{-1}. This is slow but significant.

Another important boundary condition is the sea-surface temperature T_s, which determines the surface heat and moisture fluxes. From T_s, we calculate the mixing ratio within the sea-surface skin layer, $q_s = q^*(p_s, T_s)$ and the sea-surface moist static energy $h_s = c_p T_s + L q_s$. For simplicity, we will only model the thermodynamic evolution of a SCBL, not its momentum balance, so we will just specify a mixed-layer wind speed V, and we will use bulk aerodynamic formulas with a nondimensional transfer coefficient $C_T(V) \approx 10^{-3}$ to specify the surface fluxes:

$$\overline{w'q_t'}(0) = C_T V(q_s - q_{tM}), \tag{15.10a}$$

$$\overline{w'h'}(0) = C_T V(h_s - h_{tM}). \tag{15.10b}$$

Within the boundary layer, there will be a net upward radiative flux profile $F_R(z)$ (including both longwave and shortwave contributions) and a downward water flux profile $P(z)$ due to precipitation. These fluxes must be diagnosed from the mixed layer properties, including the vertical structure of the cloud layer, following the ideas presented in Lecture 2. Here we will just assume we have some algorithm for doing this. We must also have an entrainment closure for specifying the entrainment rate w_e, which we'll discuss later.

Now we are finally ready to write down the governing equations for the MLM, which express conservation of mass, water, and moist static energy in the mixed layer:

$$\frac{dz_i}{dt} = w_e + \bar{w}(z_i), \tag{15.11}$$

$$\frac{dh_M}{dt} = -\frac{1}{\rho}\frac{\partial E}{\partial z}, \tag{15.12}$$

$$\frac{dq_{tM}}{dt} = -\frac{1}{\rho}\frac{\partial W}{\partial z}. \tag{15.13}$$

Here, d/dt is the material derivative following the boundary layer air column, which moves with the mean horizontal wind. Furthermore,

$$W(z) = \rho\,\overline{w'q_t'}(z) - P(z) \tag{15.14}$$

is the upward water flux, composed of a turbulent and precipitation flux, and

$$E(z) = \rho\,\overline{w'h'}(z) + F_R(z) \tag{15.15}$$

is the upward energy flux, composed of a turbulent and a radiative flux.

If we know w_e from the entrainment closure, the MLM equations can be solved as in the dry case. Since the left hand sides of (15.12-13) are height-independent, the same must be true of their right hand sides. Hence, the energy and water fluxes must vary linearly with height between the surface and the inversion. Defining a nondimensional height $\zeta = z/z_i$:

$$W(z) = (1-\zeta)W(0) + \zeta W(z_i), \tag{15.16a}$$

$$E(z) = (1-\zeta)E(0) + \zeta E(z_i), \tag{15.16b}$$

and

$$-\frac{\partial W}{\partial z} = \frac{W(0) - W(z_i)}{z_i}, \tag{15.17a}$$

$$-\frac{\partial E}{\partial z} = \frac{E(0) - E(z_i)}{z_i}, \tag{15.17b}$$

where

$$W(0) = \rho C_T V(q_s - q_{tM}) - P(0), \quad W(z_i) = -\rho w_e \Delta q_t, \tag{15.18a}$$

$$E(0) = \rho C_T V(h_s - h_{tM}) + F_R(0), \quad E(z_i) = -\rho w_e \Delta h + F_R(z_i). \tag{15.18b}$$

This completes the specification of the right-hand sides of (15.12-13), allowing the MLM equations to be marched forward in time.

The turbulent flux profiles of q_t and h can be recovered from the energy and water flux profiles using (15.14) and (15.15), as illustrated on the right side of Fig. 8. A popular idealization is to assume a nonprecipitating cloud ($P(z) = 0$) with all the radiative cooling concentrated just under the cloud top as a specified flux divergence ΔF_R, so that

$$F_R(z) = F_R(0) \text{ for } 0 < z < z_i, \quad \text{and } F_R(z_i) = F_R(0) + \Delta F_R. \tag{15.19}$$

Buoyancy and buoyancy flux in a stratocumulus-capped boundary layer

The buoyancy $b' = -g\rho'/\rho_0 \approx gT_v'/T_0$ where T_0 is a reference temperature. The virtual (or density) temperature T_v is defined here to include the effect of liquid water loading,

$$T_v = T(1 + \delta q_v - q_l), \quad \delta = 0.61,$$
$$\approx T + T_0(\delta q_v - q_l),$$

from which we deduce that

Physical processes affecting stratocumulus

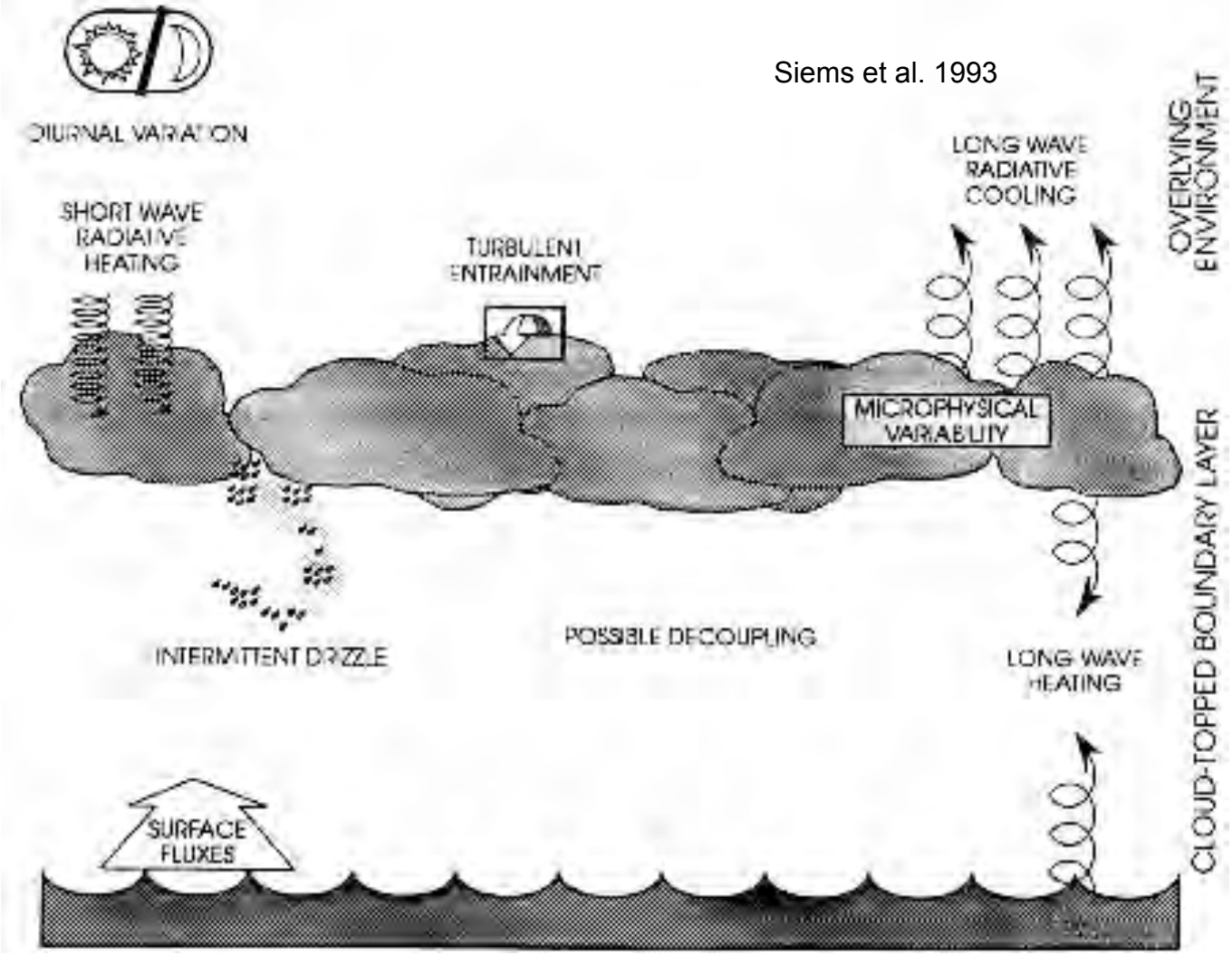

Profiles in a stratocumulus-capped mixed layer

'Well-mixed': Moist-conserved variables

$s_l = c_pT + gz - Lq_l$,

$q_t = q_v + q_l$

$h = c_pT + gz + Lq_t$

are nearly uniform with height within the MBL.

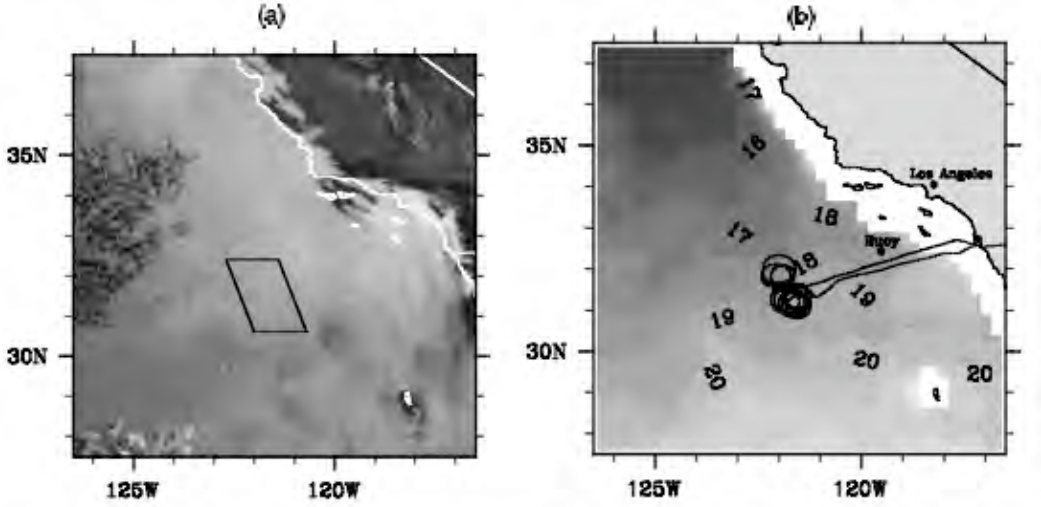

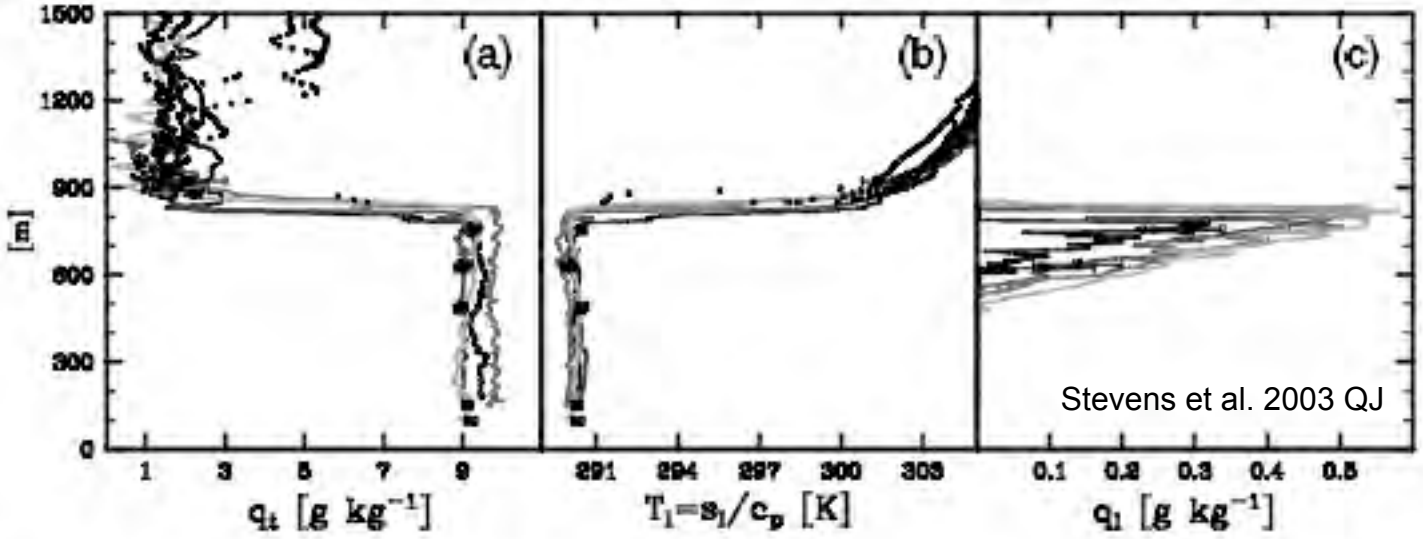

Figure 1. Cloud-layer state as observed during RF01: (a) total-water specific humidity q_t, (b) liquid-water static energy temperature s_l/c_p, and (c) liquid-water specific humidity q_l. Lines are from soundings, darker indicating earlier, filled circles and bars denote level-leg means and standard deviations, and dots denote dropsonde data from the above-cloud portion of the descent.

$\Rightarrow q_l$ increases linearly with z above cloud base

Decoupled SCBL - midday, North Atlantic.

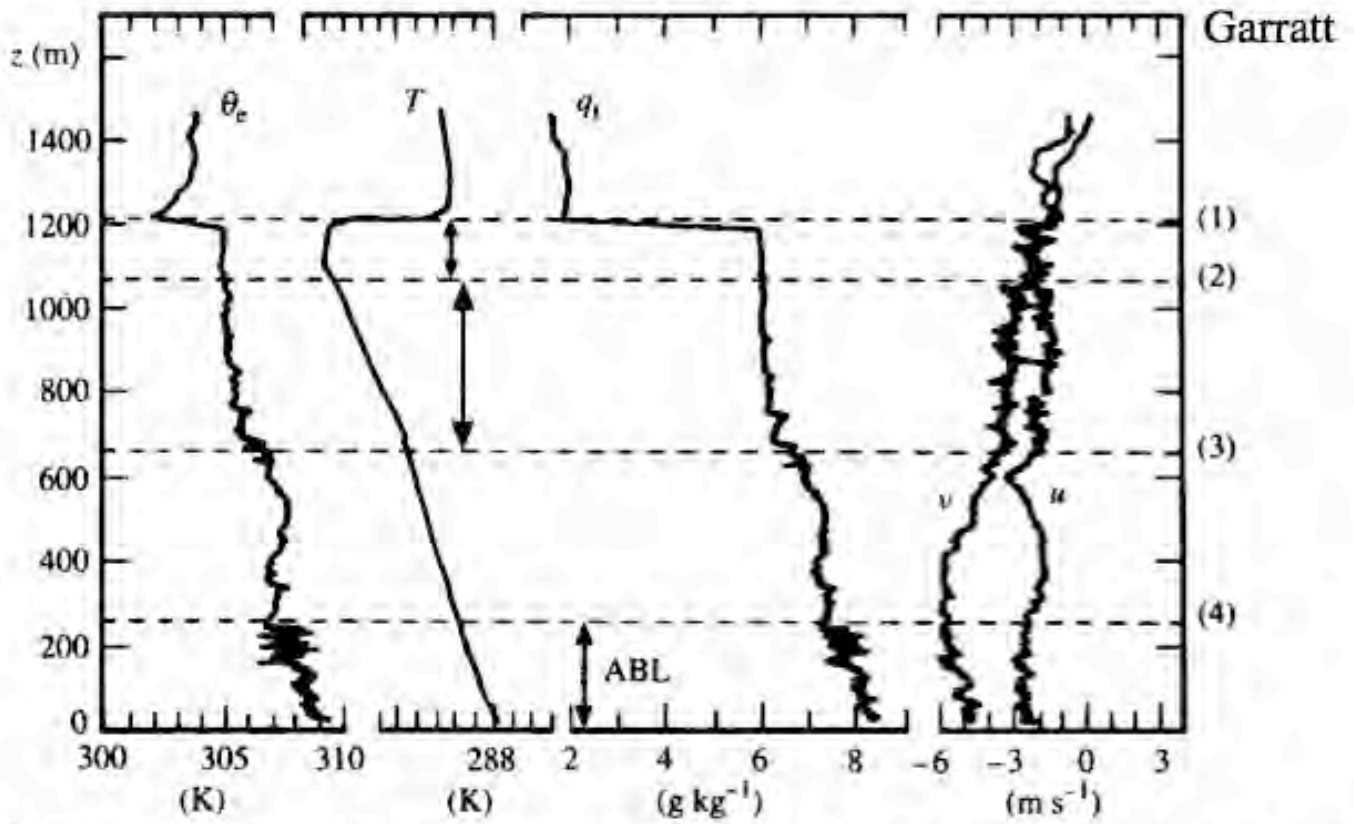

Fig. 7.5 Observed mean profiles of thermodynamic variables and wind components made in the CTBL over the ocean during JASIN, for a decoupled stratocumulus layer. The pecked horizontal lines delineate layer boundaries as follows: (1) cloud top; (2) cloud base; (3) bottom of subcloud layer; (4) top of the surface-related Ekman layer. After Nicholls and Leighton (1986), *Quarterly Journal of the Royal Meteorological Society*.

SCBL diurnal cycle in SE Pacific sonde time series

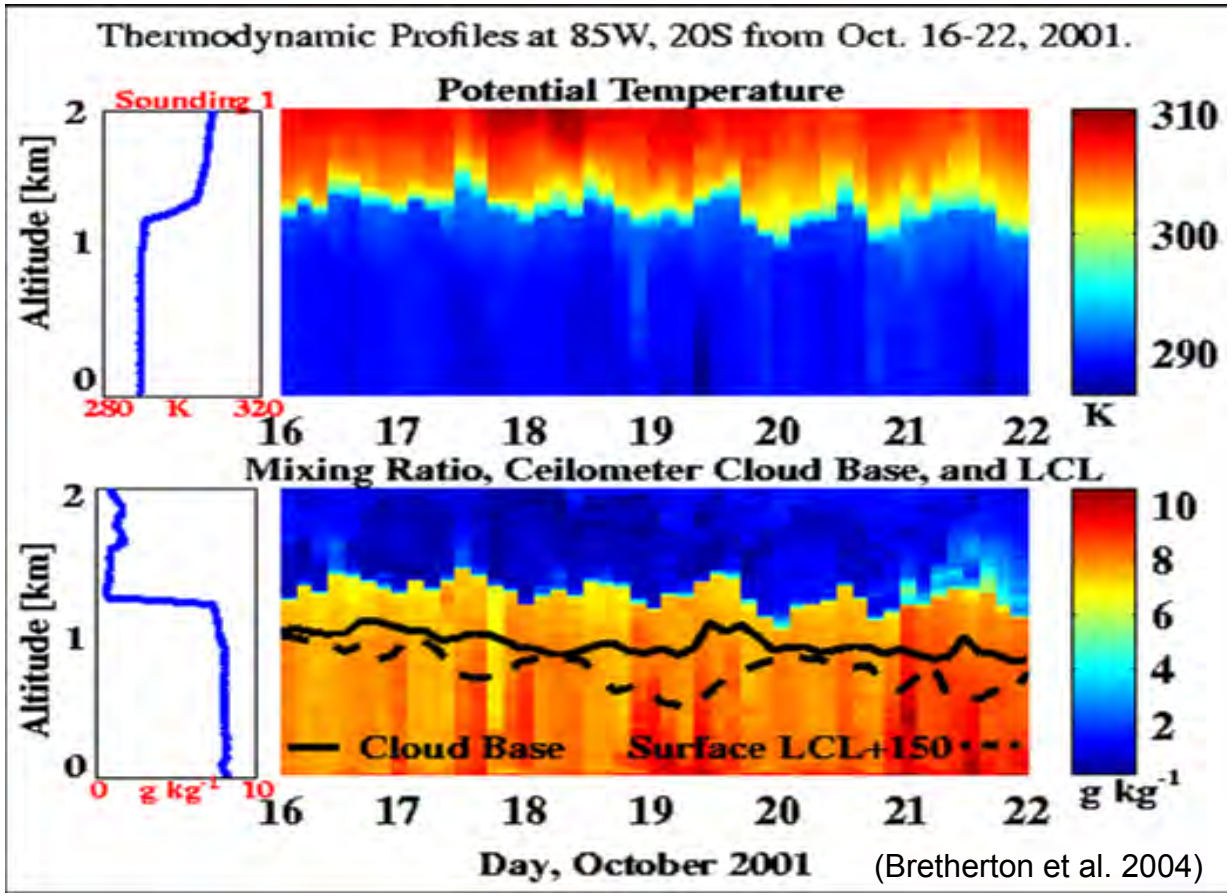

(Bretherton et al. 2004)

3-hourly sondes show:

1. Mixed-layer structure with strong sharp inversion
2. Regular night-time increase in inversion height, cloud thickness.
3. Decoupling measured by cloud base - LCL increases during daytime and during periods of drizzle on 19, 21 Oct. (local noon = 18 UTC)

Sc physical processes: Radiation

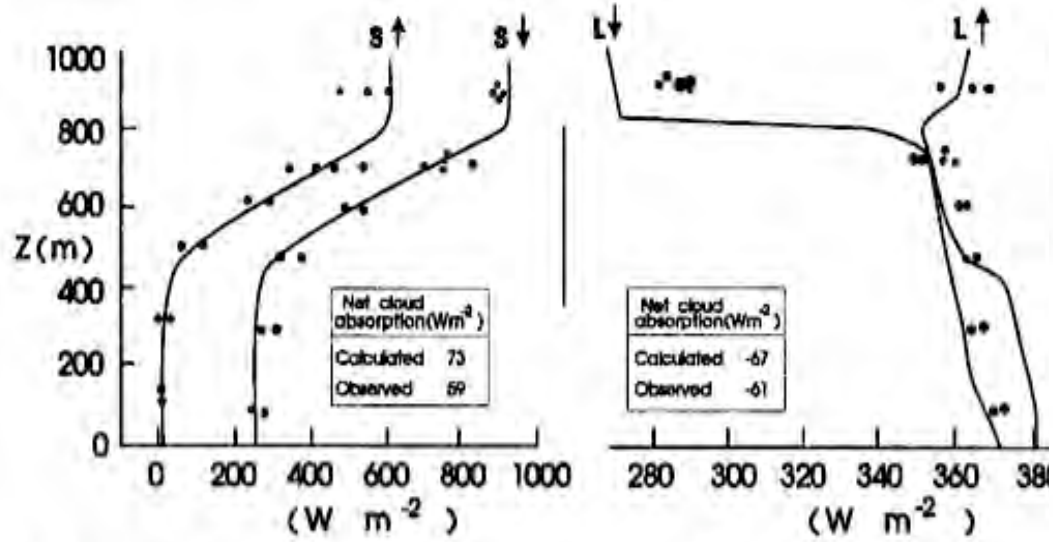

Radiative fluxes in North Sea stratocumulus (Nicholls 1984)

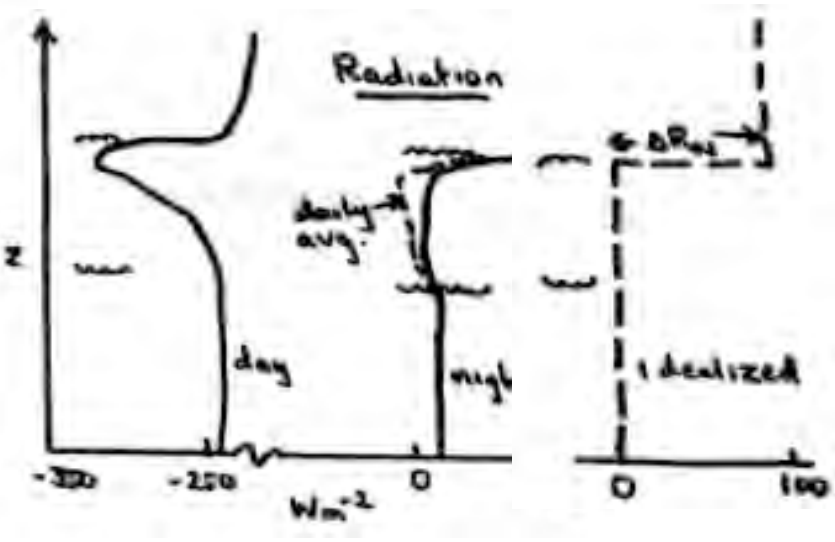

Net upward radiative flux

- Strong longwave cooling at cloud top destabilizes SCBL, creating turbulence
- Shortwave heating in cloud cancels much of the longwave cooling during the day, weakening turbulence and favoring decoupling.
- Subtropical CBL radiative energy loss is usually large compared to surface heat flux.

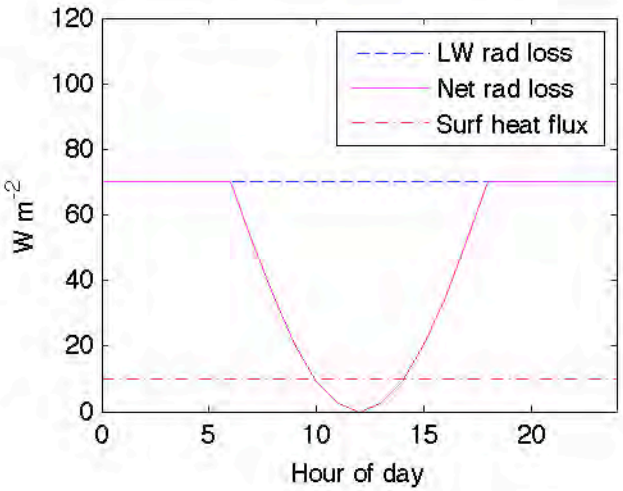

Diurnal cycle of net SCBL rad cooling

Sc physical processes: Precipitation

Drizzle: Drops > 100 μm radius, falling ~ 1 m s^{-1}.

Sedimentation (in cloud only): Cloud droplets less than 20 μm radius, falling a few cm s^{-1}.

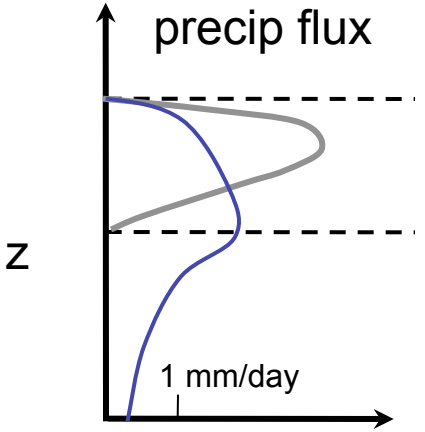

EPIC 8-mm vertically pointing 'cloud radar' observations of drizzling Sc

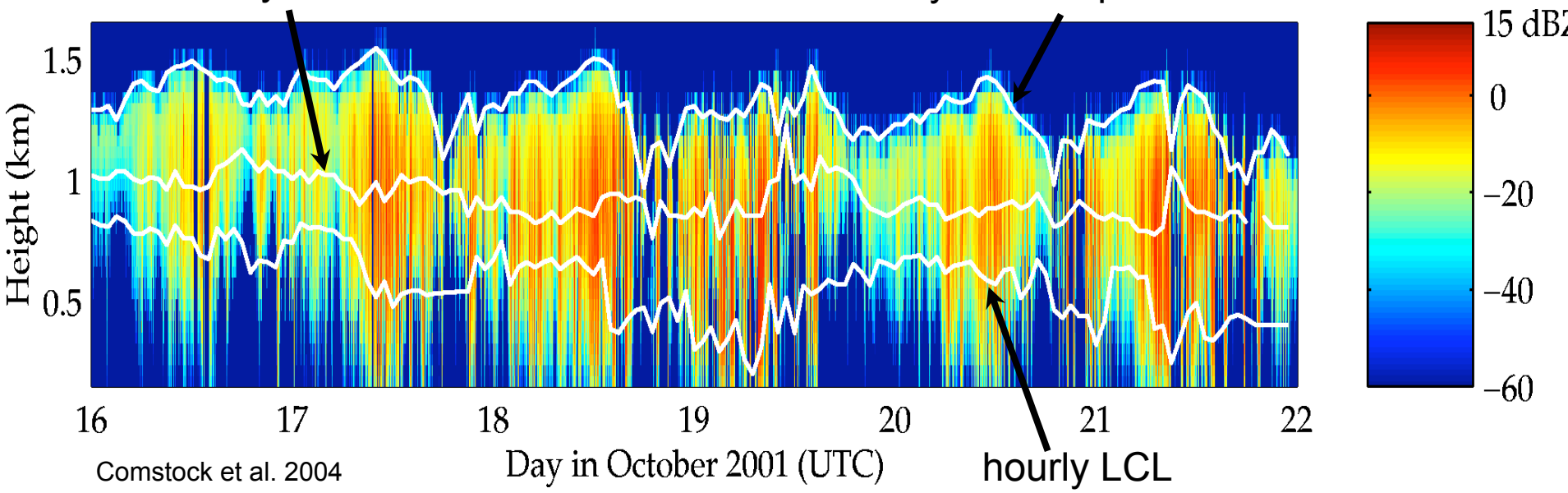

Comstock et al. 2004

Sc physical processes: Turbulent entrainment

- Driven by turbulence
- Inhibited by a strong inversion
- Must be measured indirectly (flux-jump or budget residual methods).
- The 6-day diurnal cycle of entrainment rate from EPIC (right) was independently deduced from radiosondes and other ship-based observations based on SCBL mass (black), moisture (blue) and heat budgets (red). Typical magnitudes are small (5 mm/s) and measurement uncertainties are large.

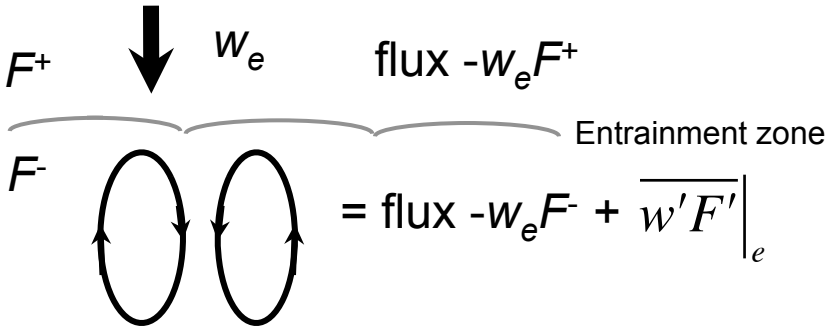

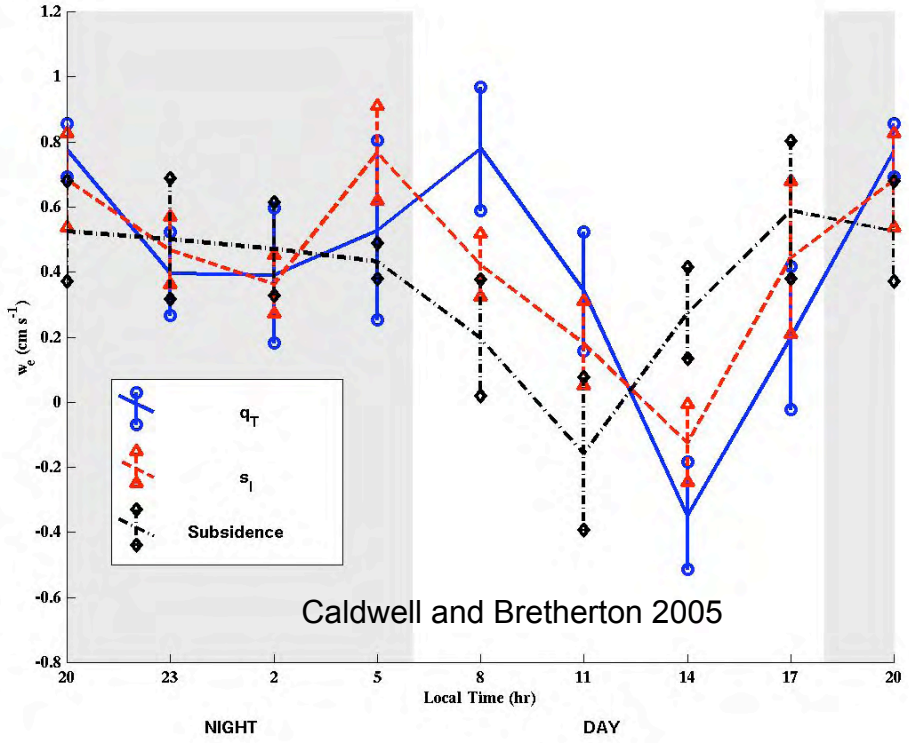

Profiles in a stratocumulus-capped mixed layer

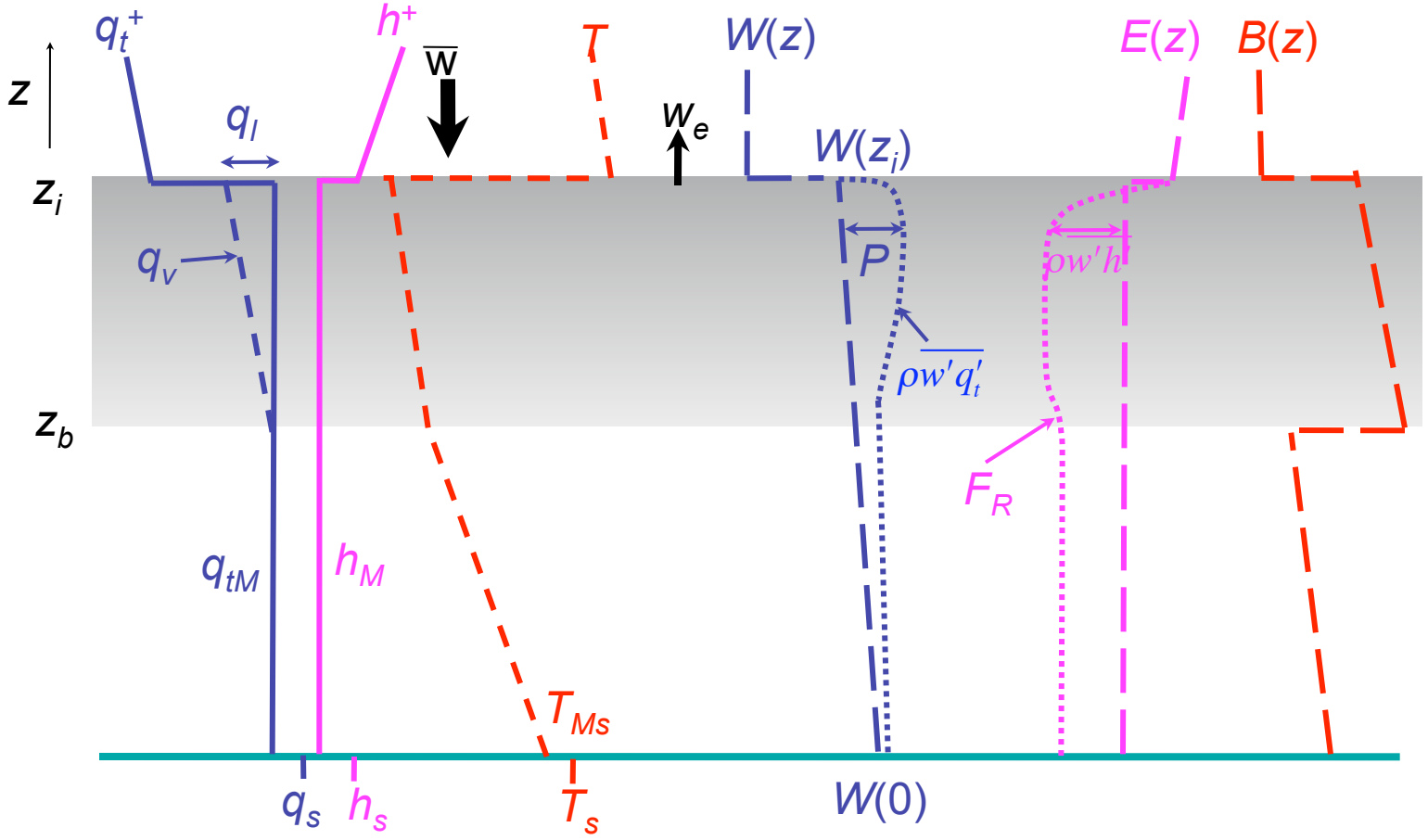

Parcel circuits in a Sc-capped mixed layer

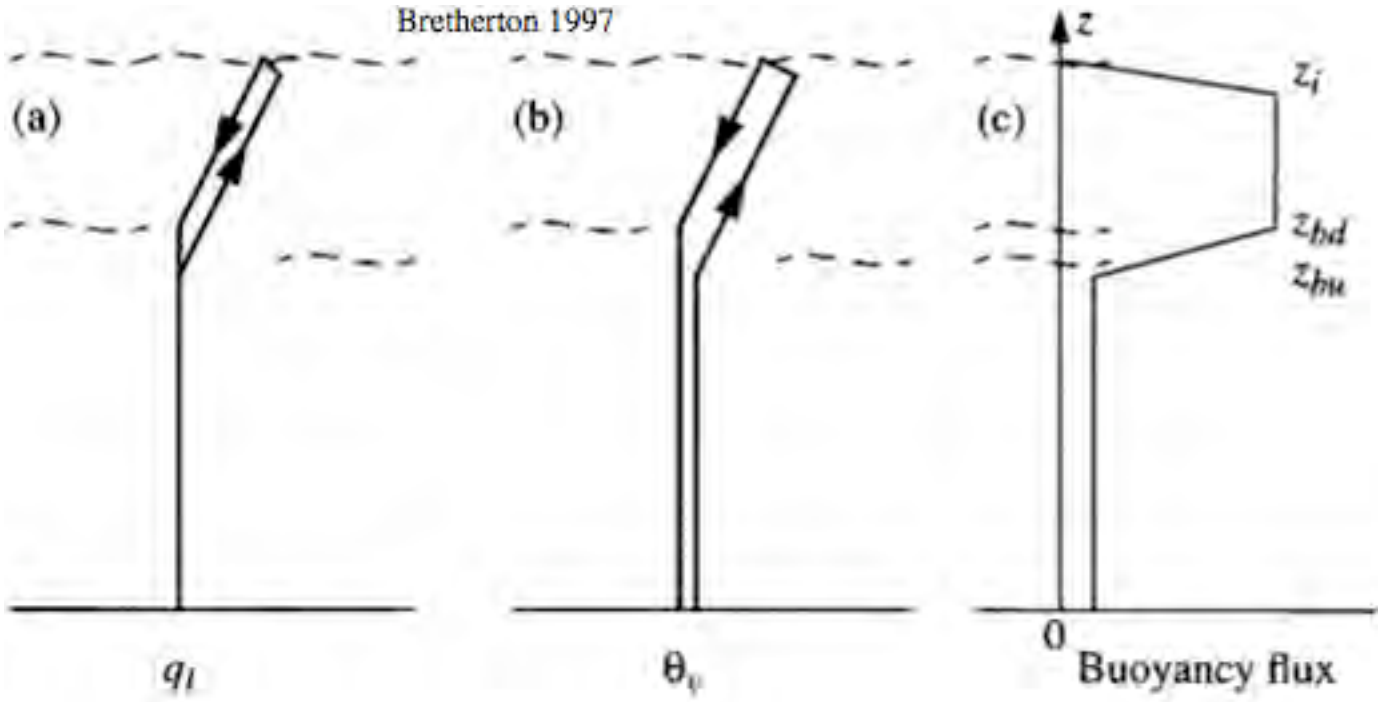

- Note implied discontinuous increase in liquid water and buoyancy fluxes at cloud base ⇒ turbulence driven from cloud, unlike dry CBL.
- Convective velocity w_* ~ 1 m s^{-1}:

$$w_*^3 = 2.5\int_0^{z_i} \overline{w'b'}dz$$

Sc MLM entrainment closure

Nicholls-Turton (1986) entrainment closure
Fit to aircraft and lab obs and dry CBL

$$w_e = A\frac{w_*^3}{z_i \Delta b}, \quad A = 0.2(1 + a_2 E), \quad \Delta b = g\,\Delta T_v / T_0$$

Evaporative enhancement: Less buoyant mixtures easier to entrain.

NT enhancement factor $E = \Delta_m / \Delta T_v$

a_2 = 15-60 $\Rightarrow$ A = 0.5 - 5 in typical Sc

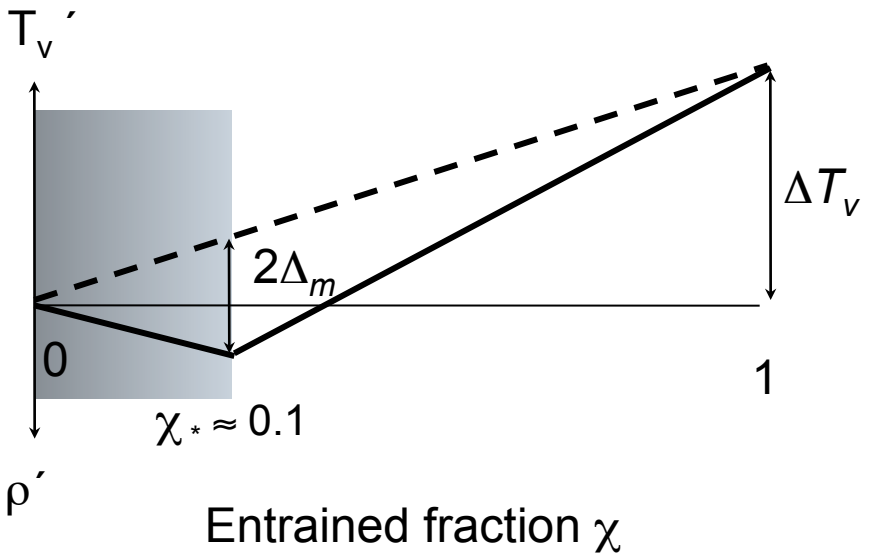

Observational test with
SE Pacific Sc diurnal cycle
(Caldwell et al. 2005)

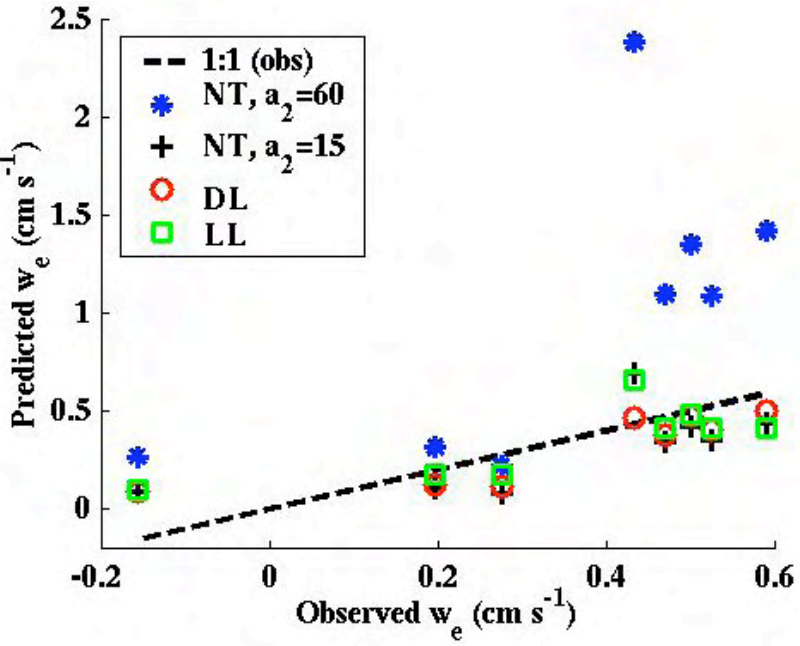

NT: Nicholls and Turton (1986)
DL: Lilly (2002)
LL: Lewellen&Lewellen (2003)

MLM examples

Steady-state solutions: Higher SST, lower divergence promote deeper mixed layer with thicker cloud.

Cloud top

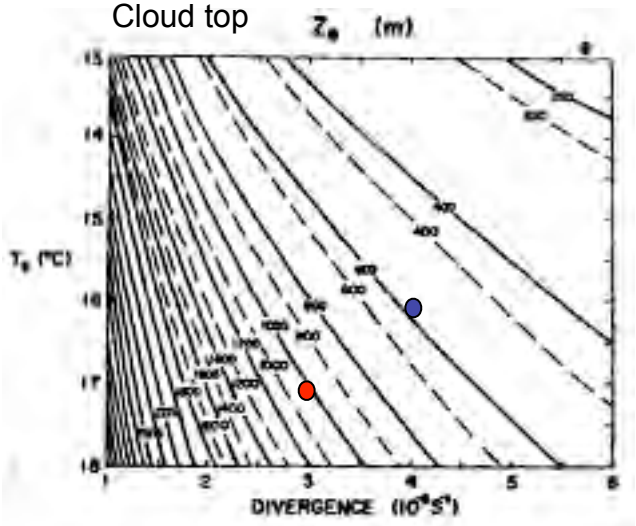

Cloud base

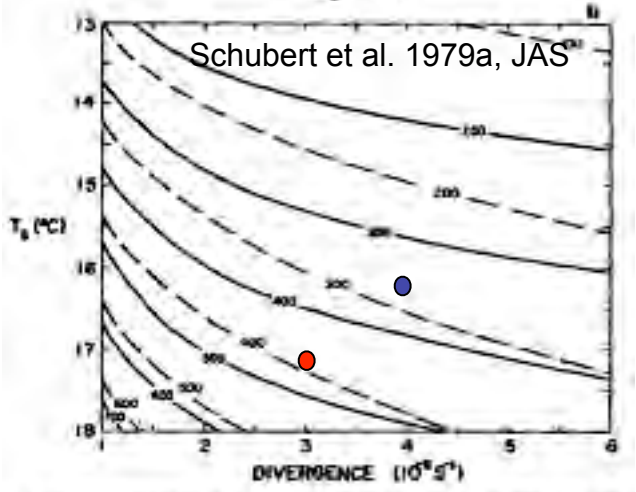

SST = 16 C, D = 4×10^{-6} s^{-1}

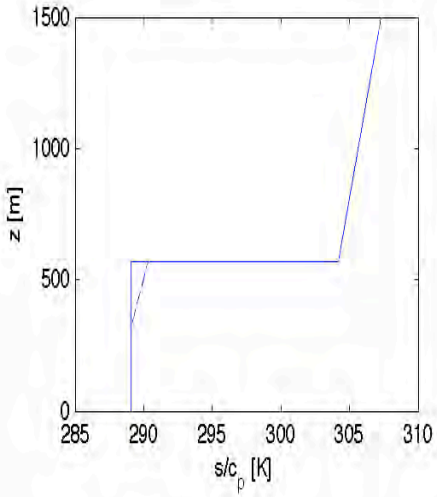

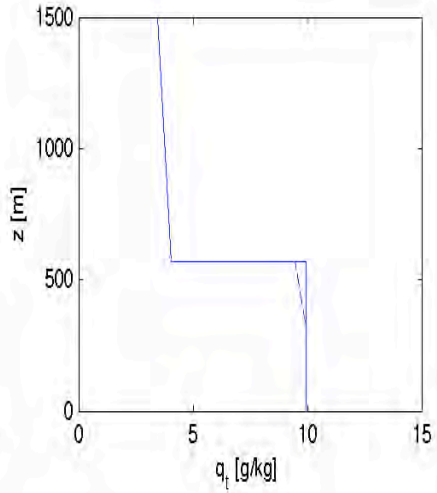

SST = 17 C, D = 3×10^{-6} s^{-1}

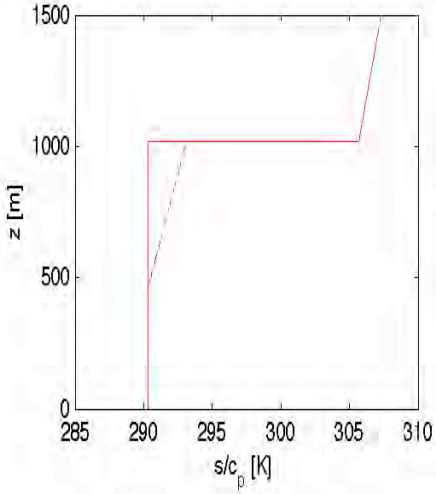

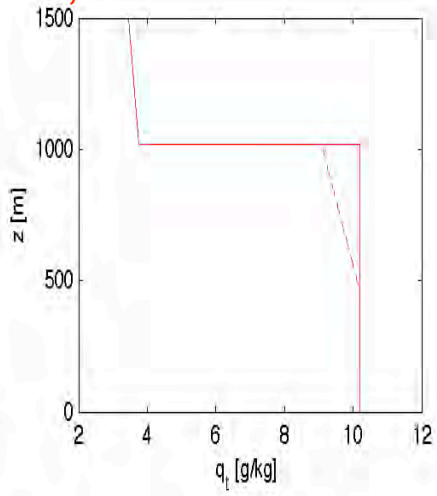

MLM response to a +2K SST jump

Two timescales:

Fast internal adjustment

$t_b = z_i / C_T V \sim 0.5$ day

Slow inversion adjustment

$t_i = D^{-1} \sim 3$ days

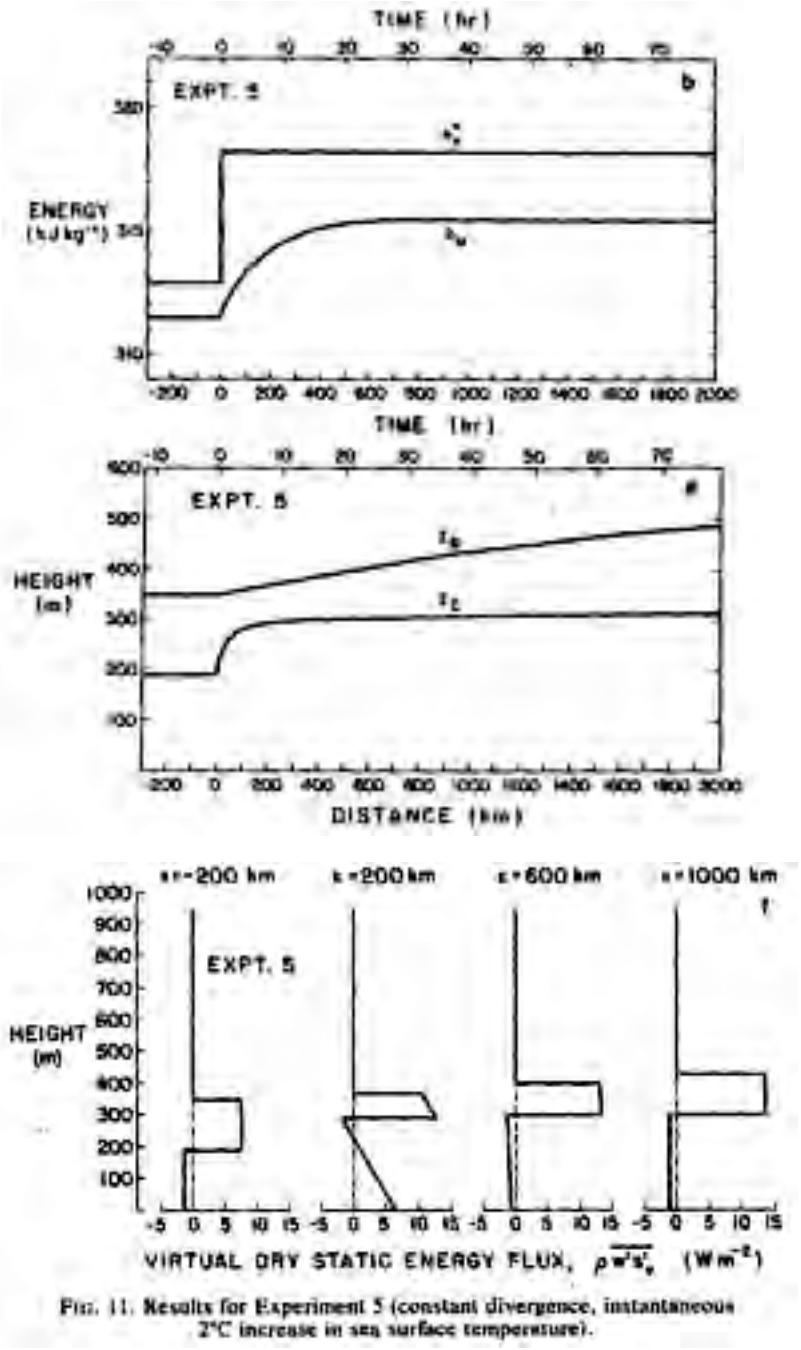

FIG. 11. Results for Experiment 5 (constant divergence, instantaneous 2°C increase in sea surface temperature).

Schubert et al. 1979b JAS

MLM diurnal cycle

MLM prediction: cloud thickens during the day because of decreased entrainment, opposite to observations. MLM breaks down during day and in deeper or drizzly BLs due to BL decoupling (next lecture)

Schubert 1976 JAS

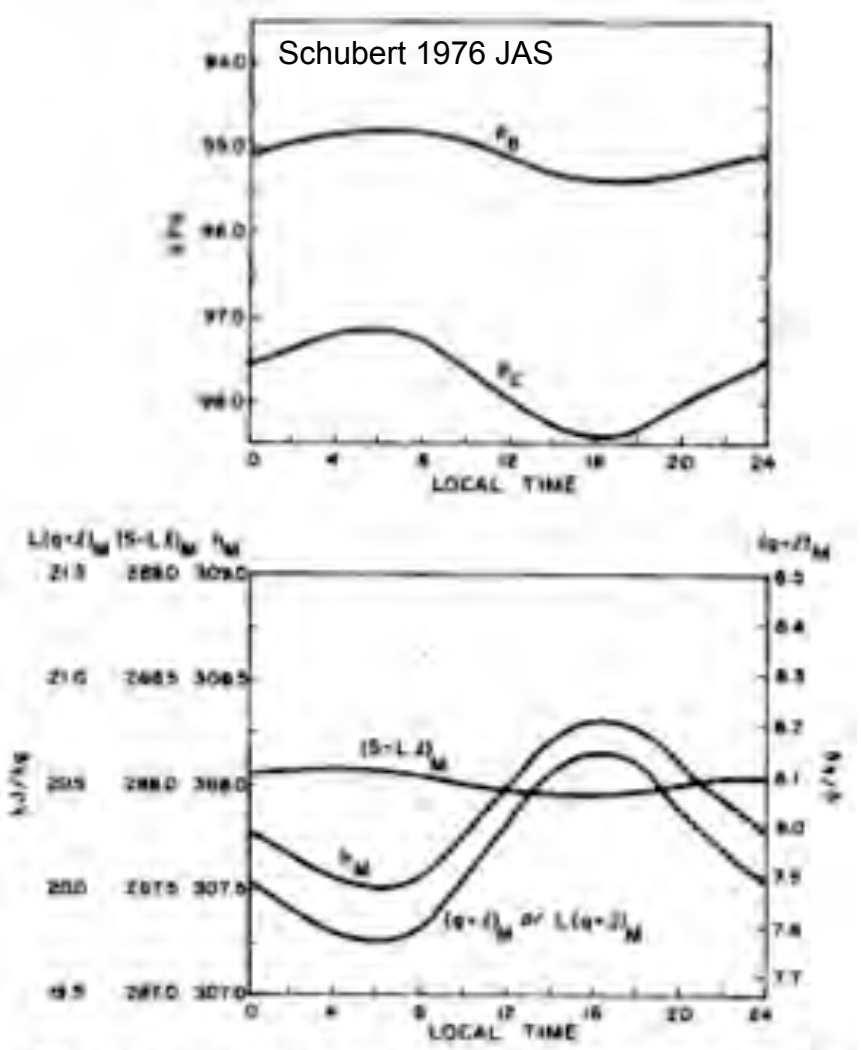

FIG. 7a. Diurnal variation of p_M and p_c (top) and h_M, $(s-Ll)_M$ and $(q+l)_M$ (bottom). Local time 1200 corresponds to noon. The large-scale divergence is 5.0×10^{-6} s^{-1}, the sea surface temperature 13°C, and the entrainment parameter 0.20.

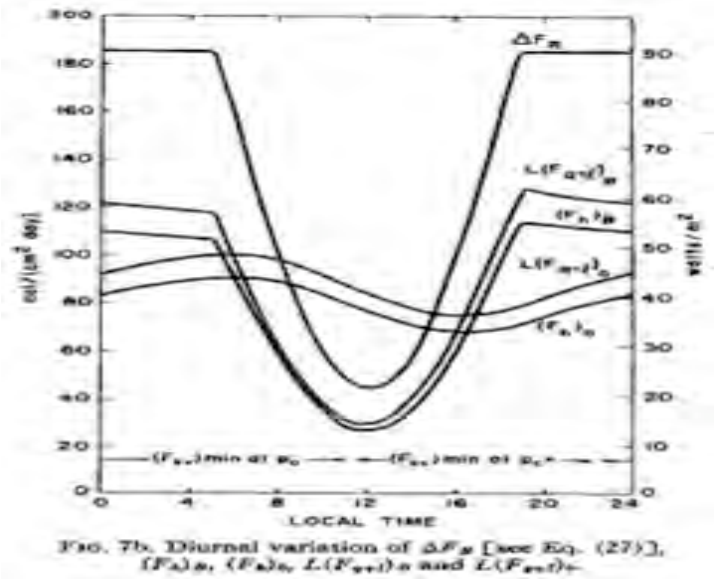

FIG. 7b. Diurnal variation of ΔF_M [see Eq. (27)], $(F_u)_M$, $(F_u)_0$, $L(F_{q+l})_M$ and $L(F_{q+l})_0$.

Lecture 16 Cloud-topped mixed layers II

An idealized marine CTML

We now step back and try to understand what controls the depth, cloud thickness and evolution timescales of a stratocumulus-capped boundary layer. Following Lilly (1968) and Schubert et al. (1979, *J. Atmos. Sci.*, **36**, 1286-1307) we consider a simplified model of a cloud-topped mixed layer (CTML), making the following assumptions:

(i) Surface transfer given by bulk aerodynamic formulas with an exchange velocity $C_T V$, where V is a BL wind speed and $C_T \approx 1.5 \times 10^{-3}$ is a neutral drag coefficient. For a typical wind speed of 7 m s^{-1}, $C_T V \approx$ 1 cm s^{-1}.

(ii) Radiation idealized as a fixed cloud-top jump ΔR_N.

(iii) No drizzle

(iv) $\overline{w} = -Dz$, where D is a specified horizontal divergence (typically 0-6 $\times 10^{-6}$ s^{-1})

(v) Geometric flux-partitioning entrainment closure with $\overline{w'b'}|_{\min} = - c\overline{w'b'}|_{\text{av}}$. Schubert et al. take $c = 0.2$.

(vi) We are following a PBL air column, so there is no horizontal advection term.

The mixed layer equations are then

$$dh/dt = w_e - Dh \tag{1}$$

$$dq_{tM}/dt = \{w_e(q_t^+(h) - q_{tM}) + C_T V(q_{t0} - q_{tM})\}/h \tag{2}$$

$$d\theta_{eM}/dt = \{w_e(\theta_e^+(h) - \theta_{eM}) - \Delta R_N/\rho c_p + C_T V(\theta_{e0} - \theta_{eM})\}/h \tag{3}$$

It is convenient to replace (3) by an equivalent equation for the liquid water virtual potential temperature $\theta_{vl} = \theta_e - (\mu L/c_P) q_t$. Noting that $\theta_{vl} = \theta_v$ in the free troposphere and at the surface (and everywhere else outside the cloud), can subtract $\mu L/c_P \times$(2) from (3) to obtain

$$d\theta_{vlM}/dt = \{w_e(\theta_v^+(h) - \theta_{vlM}) - \Delta R_N/\rho c_p + C_T V(\theta_{v0} - \theta_{vlM})\}/h \tag{4}$$

Four possibly time-dependent external parameters force the mixed layer. These are the radiative flux divergence ΔR_N, the divergence D, the SST, and the surface transfer velocity $C_T V$. In addition we must specify the free tropospheric profiles $q_t^+(z)$ and $\theta_v^+(z)$.

Steady-state structure

If the external parameters and profiles are time-independent, we may seek a steady-state solution and investigate its dependence on these parameters. It is important to understand that in reality the geographic distribution of the BL structure feeds back on the entire circulation of the troposphere, so that what we treat as 'external' depends on our perspective!

For simplicity of analysis we will for the moment take $c = 0$ (rather than 0.2) in the entrainment closure; this has little impact on the steady state solutions. Given our assumptions, the flux of θ_{vl} must be linear with height, and because there is no flux divergence in a steady state, the steady-state θ_{vl} flux must be height independent. The buoyancy flux is proportional to the θ_{vl} flux below cloud base, and will be larger above cloud base. Thus the condition that the minimum buoyancy flux in the mixed layer be zero implies that the θ_{vl} flux is zero everywhere below cloud base, including down to the sea-surface. Thus, by the bulk aerodynamic formula, the steady state or 'equilibrium' solution must satisfy

$\theta_{vl,eq} = \theta_{v0}$ (to ensure negligible surface buoyancy flux)

From the steady-state versions of (1) and (2),

$w_e = Dh_{eq}$ (subsidence balances entrainment rate)

$q_{t,eq} = \chi q_t^+ + (1 - \chi) q_{t0}$ (surface moistening balances entrainment drying)

where $\chi = w_e/(w_e + C_T V)$ can be interpreted as the mixing fraction of above inversion (vs. sea-surface) air in the mixed layer The steady-state PBL energy balance implied by (4) is

$$w_e(\theta_v^+ - \theta_{v0}) = \Delta R_N/\rho c_p$$

Setting $w_e = Dh_{eq}$, we must have

$$Dh_{eq}(\theta_v^+(h_{eq}) - \theta_{v0}) = \Delta R_N/\rho c_p \quad (5)$$

This is a quadratic for h_{eq} with one positive root. We can work backward to get the rest of the mixed layer parameters.

We will first consider a specific example using idealized free-tropospheric conditions conditions off the California coast, $\Delta R_N = 50$ W m^{-2}, $D = 5 \times 10^{-6}$ s^{-1}, SST = 290 K, and $C_T V = 1$ cm s^{-1}, a surface pressure $p_0 = 1020$ mb, and

$q_t^+(z) = 4$ g kg^{-1} and $\theta_v^+(z) = 303 + 0.004z$ K (z in meters)

At the saturated sea-surface

$q_{t0} = q^*(p_0, \text{SST}) = 12$ g kg^{-1},

$\theta_{v0} = (1000/1020)^{.285}\text{SST}(1 + .61 q_{t0}) = 290.5$ K

Thus $\theta_{vl,eq} = 290.5$ K. Solving the quadratic (5) for the given parameters, we get

$h_{eq} = 564$ m, $w_e = 0.3$ cm s^{-1}, $\theta_v^+ - \theta_{v0} = 14.8$ K

The mixing fraction of above inversion air $\chi = w_e/(w_e + C_T V) = 0.22$, so

$q_{tM} = \chi q_t^+ + (1 - \chi) q_{t0} = 10.3$ g kg^{-1}.

Together with the requirement that $\theta_{vlM} = 290.5$ K, this allows us to deduce the equilibrium mixed layer temperature 290.3 K just above the sea-surface, and the saturation mixing ratio 12.3 g kg^{-1} at that temperature . Using a formula for how fast saturation mixing ratio decreases with height in a well-mixed (dry adiabatic) stratification (4.9 g kg^{-1} km^{-1} at the given temperature and pressure), we can deduce the cloud base height at which BL air is exactly saturated:

$z_b = (12.3 \text{ g kg}^{-1} - 10.3 \text{ g kg}^{-1})/(4.9 \text{ g kg}^{-1} \text{ km}^{-1}) = 414$ m.

The cloud base is 150 m beneath the inversion, consistent with the assumption that the mixed layer is cloud-topped. However, this in not guaranteed. If the wind is too weak or the divergence much stronger than assumed above, the predicted equilibrium cloud base will be above the BL top, so the BL cannot be cloud-topped. However, for weak to moderate subsidence and typical BL wind speed and above-BL profiles, the equilibrium BL is cloud-topped.

The plots below show the variation of equilibrium cloud base and top as SST and *D* are varied for a model similar to that above, taken from Schubert *et al.* Disregard the dashed lines. For weak divergence and high SST, typical of conditions further downwind in the mean trade wind circulation, deep BLs are obtained but their cloud base is still only 500-600 m, implying very thick stratocumulus layers. An obvious question is how the cloud-top mixed layer structure breaks up into the observed shallow trade cumulus boundary layers that are seen.

Schubert et al. 1979

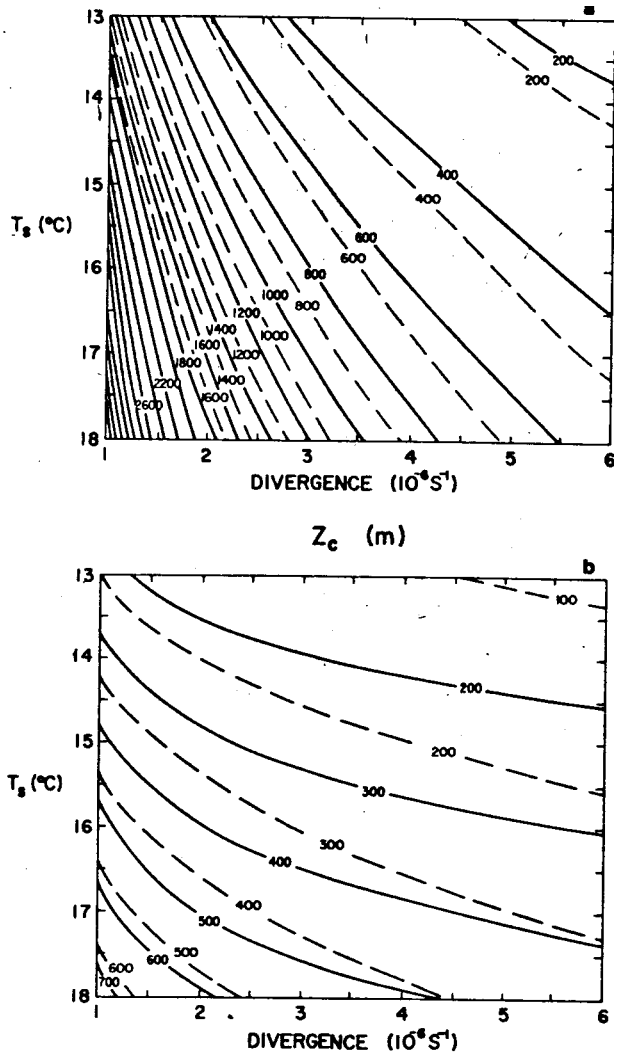

Contours of equilibrium well mixed BL top (top) and cloud base (bottom) as functions of SST and mean horizontal divergence.

Timescales

Over land, the strong diurnal cycle guarantees that the daytime convective BL never achieves a steady state. However, marine CTBLs are closer to a steady state structure. Following a very nice paper by Schubert et al. (1979, *J. Atmos. Sci.*, **36**, 1308-1324), we consider the timescales for the BL to relax toward a steady state, by rephrasing the mixed layer equations as follows:

$$dh/dt = w_e - Dh = (h_{eq} - h)/\tau_h \tag{6}$$

$$\partial q_{tM}/\partial t = \{w_e(q_t^+ - q_{tM}) + C_T V(q_{t0} - q_{tM})\}/h = (q_{t,eq} - q_{tM})/\tau_M \tag{7}$$

$$\partial \theta_{eM}/\partial t = \{w_e(\theta_e^+ - \theta_{eM}) - \Delta R_N/\rho c_p + C_T V(\theta_{e0} - \theta_{eM})\}/h = (\theta_{e,eq} - \theta_{eM})/\tau_M \tag{8}$$

where the relaxation timescales are

$\tau_h = D^{-1}$ for BL depth

$\tau_M = h/(w_e + C_T V)$ for internal thermodynamic adjustment

For typical values for subtropical Sc-topped mixed layers, $D = 5 \times 10^{-6}$ s^{-1} , $w_e = 0.5$ cm s^{-1}, $C_T V = 1$ cm s^{-1}, we find that:

τ_M = (500 m)/(0.5 + 1 cm s^{-1}) = 30,000 s ≈ 0.4 days,

τ_h = 200,000 s = 2.3 days.

The internal thermodynamic state of the BL rapidly adjusts on the time τ_M to changes in SST and free-atmospheric properties. The BL depth relaxes to an equilibrium value on a much longer timescale τ_h = 200, 000 s = 2.3 days . During this time, slow thermodynamic changes also continue as the entrainment rate and the temperature and humidity of the entrained air adjust to the changing depth of the boundary layer.

The figure below shows the response of a cloud-topped mixed layer to a 2 K step change in SST. The rapid adjustment of cloud base (i. e. the internal thermodynamic state) to the changed SST contrasts with the much slower adjustment of cloud top. In this figure, BL changes are envisioned as occuring as the BL air column advects over a changing surface with a fixed wind speed $V = 7$ m s^{-1}, so 1 day's evolution corresponds to a distance of 600 km In reality, the conditions following a BL air column are rarely nearly constant over periods of many days, so the BL height is usually not in equilibrium.

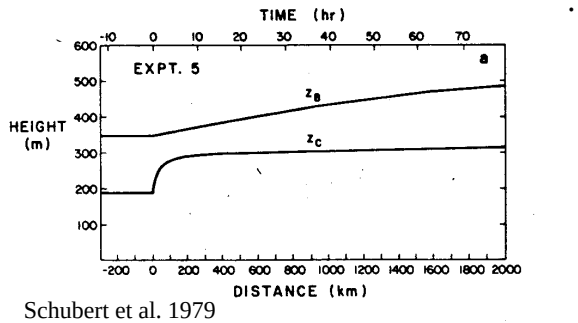

Schubert et al. 1979

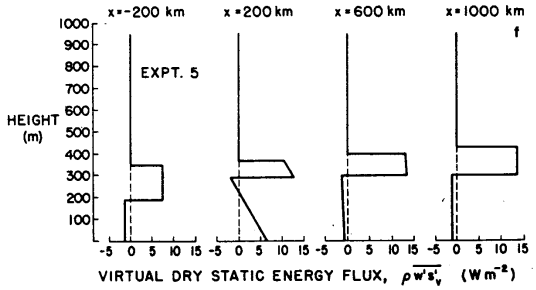

FIG. 11. Results for Experiment 5 (constant divergence, instantaneous 2°C increase in sea surface temperature).

Diurnal decoupling

Solar absorption in stratocumulus clouds has a large impact on the diurnal cycle of the marine CTBL. This was first discussed in detail by Nicholls (1984, QJRMS, **110**, 783-820). The 1987 FIRE-MSC experiment documented the diurnal cycle in Sc 100 km off the California coast. Considerable cloud thinning (a factor of four decrease in liquid water path) and a reduction in cloud albedo from 50% to 30% is observed during the morning (see figure on next page). This is not simply cloud 'burning off' due to warming of cloudy air by the absorbed sunlight, resulting in evaporation of the cloud. Instead it is mainly driven by a change in the BL turbulent structure called **diurnal decoupling**. To understand this process it is helpful to consider the effect of absorption-induced heating on the buoyancy flux profile of a mixed layer. The heating is trying to stabilize the region below it. Buoyancy fluxes must be more negative (helping keep the subcloud layer as warm as the cloud) to maintain a mixed layer.

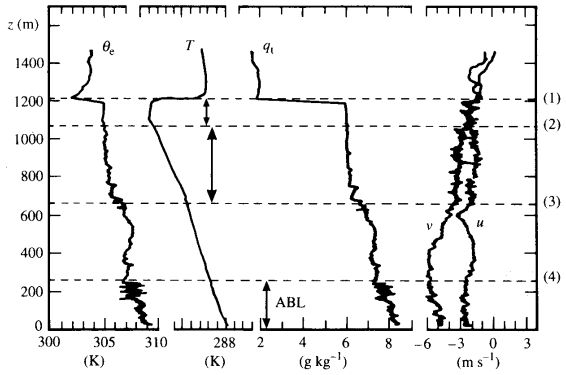

Fig. 7.5 Observed mean profiles of thermodynamic variables and wind components made in the CTBL over the ocean during JASIN, for a decoupled stratocumulus layer. The pecked horizontal lines delineate layer boundaries as follows: (1) cloud top; (2) cloud base; (3) bottom of subcloud layer; (4) top of the surface-related Ekman layer. After Nicholls and Leighton (1986), *Quarterly Journal of the Royal Meteorological Society*.

A decoupled boundary layer near local noon.

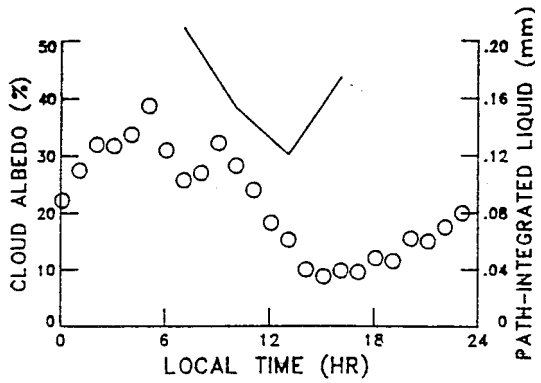

The diurnal cycle of cloud albedo (solid) and liquid water path (circles) averaged over 23 Jun - 15 Jul 1987 at San Nicholas Island off the California coast .

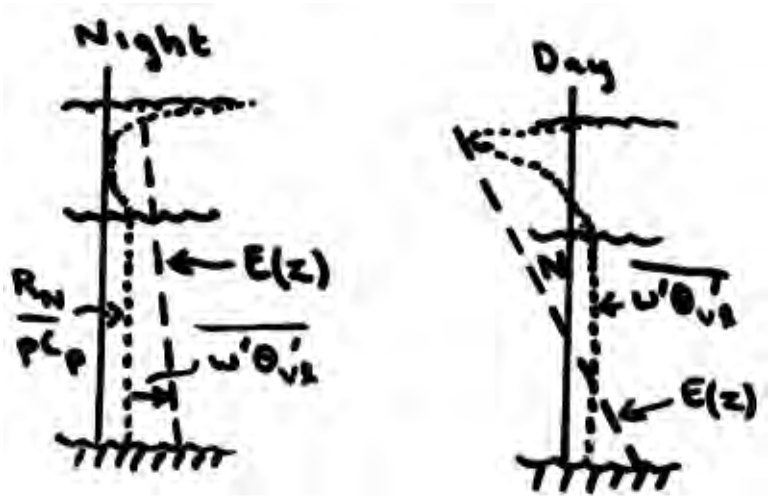

Nighttime and daytime profiles of radiative, θ_{vl} and total enegy fluxes in a mixed layer.

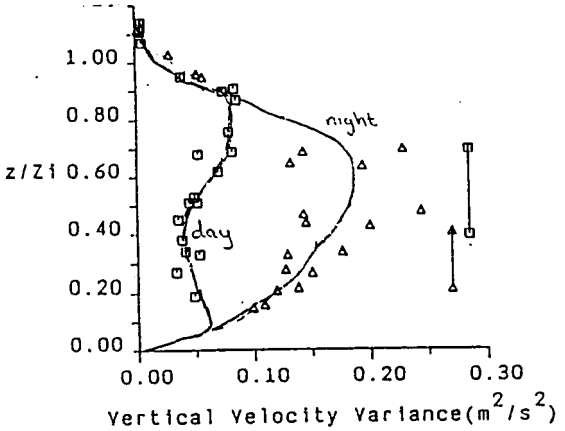

Tethered balloon measurements during three days of FIRE-MSC, 1987, showing impact of decoupling on vertical velocity variance (Hignett 1991).

The top figure above shows nighttime and daytime mixed layer profiles of θ_{vl} flux (which is proportional to buoyancy flux below cloud base) visualized as the difference between the total flux $E(z) = + R_N/\rho c_p$ forcing θ_{vl} and the radiative flux. During the day, cloudtop R_N is very small so $E(h)$ is dominated by the negative contribution of entrainment. This forces a large area, N, of negative buoyancy fluxes beneath cloud base, that suggests that the mixed layer must break down due to decoupling.

As the zone of negative buoyancy fluxes below cloudbase expands, transport of TKE becomes insufficient to sustain convection within this region, and it becomes stably stratified, separating **decoupled** convective layers near the surface (driven by surface fluxes) and within the cloud (driven by the cloud-top cooling that overlies the absorption heating). An example of a decoupled CTBL over the summertime N Atlantic around local noon is shown on the previous page. Within the two convective layers, well-mixed profiles of θ_e, q_t, u, and v are seen, separated by a stably stratified 'transition' layer characterized by intermediate values of these quantities. Mean daytime and nighttime vertical velocity variance profiles measured by a tethered balloon during FIRE-MSC are

shown above, and illustrate that during the night, the vertical velocity variance is maximum in the middle of the layer where large-eddy up and downdrafts are maximum, while during the day separate surface layer and cloud layer maxima exist, indicative of two convective layers separated by a stable layer with gravity wave activity and perhaps intermittent turbulence.

After decoupling occurs, the cloud mixed layer dries due to entrainment, so the cloud base steadily rises and the cloud may partly or fully dissipate. The surface mixed layer moistens due to surface fluxes. 'Scud' cloud may start forming at its top, well beneath the main Sc cloud base. The transition layer is usually conditionally unstable, so more vigorous scud clouds may begin to rise as cumuli into the upper Sc layer. In shallow coastal Sc, this process is not thought to contribute significantly to the overall fluxes of heat or moisture, but in deeper CTBLs it becomes of paramount importance.

Late in the afternoon, shortwave heating becomes less potent, and the upper mixed layer begins to cool more rapidly due to longwave cooling. As it cools, it penetrates further back down into the transition layer and during the evening usually 'reconnects' with the surface mixed layer. When the two layers reconnect, the cloud rapidly deepens again and a single mixed layer is reestablished. Turton and Nicholls (1987) presented an elegant simulation of this process in which two mixed layers are separated by a nonturbulent stable layer. While a mixed layer model (figure below, right) shows almost no daytime thinning of the cloud (shaded region in upper plot), their model (left) predicts that the upper mixed layer dries by 0.5 g kg^{-1} while the lower mixed layer moistens almost 1 g kg^{-1}, resulting in a 70% thinning of the upper Sc layer while thin scud develops atop the lower mixed layer. The lower panels show the corresponding diurnal evolution of the conserved variables in the two models.

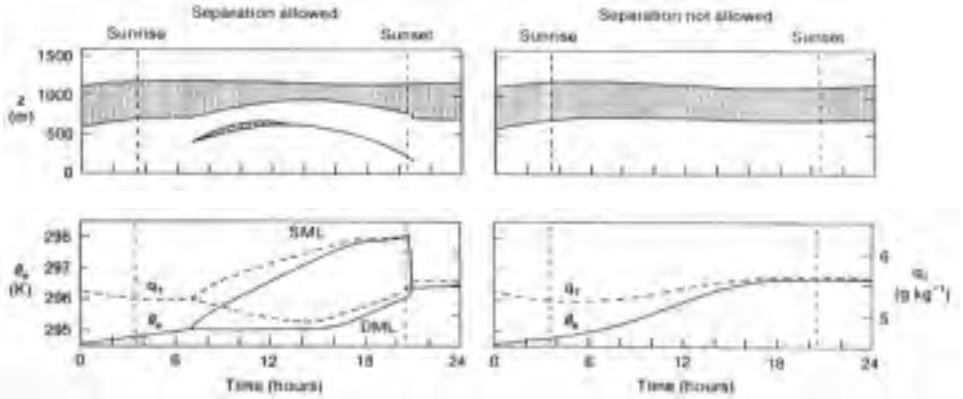

Turton and Nicholls (1987) multiple mixed-layer simulation of diurnal decoupling

Lecture 17. Dynamics of shallow cumulus boundary layers

General description

The dynamics of cumulus-topped boundary layers is an interplay between surface buoyancy and moisture input, latent heating and evaporation around the cumulus clouds, radiative cooling, and precipitation. The general features of such boundary layers are fairly universal and well understood, but many of the important details, including how to quantitatively predict the cloud cover and optical properties, remain poorly understood and important parameterization problems. Oceanic shallow cumulus boundary layers are important because of their enormous areal extent and climatic importance. Over land, shallow cumulus boundary layers are often precursors to deep convection, and can play an important role in its timing and location. In addition, even the small fractional cloud cover of shallow cumuli can have important feedbacks on the evolution of land surface temperature. Shallow cumulus clouds also vertically mix momentum.

Dynamics of a shallow cumulus BL

We discussed the typical observed structure of a shallow Cu BL in Lecture 14, and identified four sublayers - a subcloud mixed layer extending up to the cumulus cloud bases, a thin transition layer, usually identifiable on individual soundings but blurred out in the horizontal mean, a conditionally unstable layer and an inversion layer. It has been many years since a state-of-the-art shallow cumulus field experiment has been performed, and LES simulate this type of BL fairly well. Hence we first present LES simulations of a shallow cumulus ensemble based on a composite sounding, SST, and winds from a three-day period of nearly steady-state trade-cumulus convection on 22-24 June 1969 over the tropical west Atlantic Ocean during the BOMEX experiment. During this period, there were strong easterly trade winds and persistent mean subsidence. Then we discuss the dynamical balances that maintain this structure. The most comprehensive textbook description of shallow cumulus convection is Ch. 8 of Cotton and Anthes; there is also some useful, mainly theoretical, discussion at the end of Ch. 13 of Emanuel's *Atmospheric Convection*, (Oxford University Press, 1994) pp. 443-457.

<u>LES ensemble structure</u>

Figure 1 shows the mean initial sounding of temperature and winds, and model-simulated sounding after six simulated hours, showing that the models can maintain the observed steady-state if the combined advective and radiative forcings and the observed surface fluxes are specified.

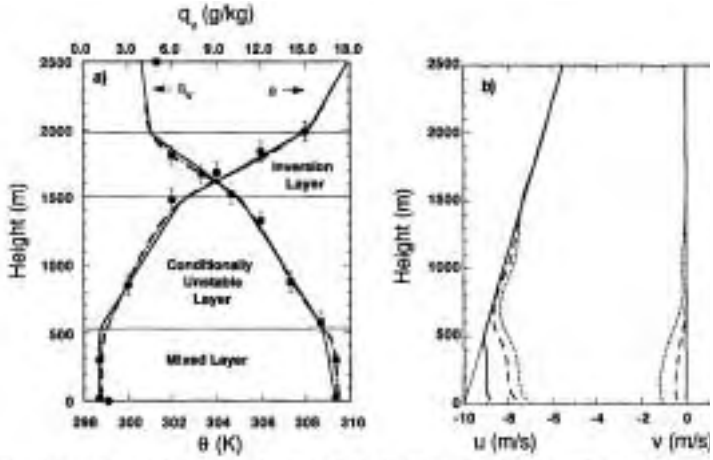

FIG. 1. Horizontally averaged vertical profiles of θ and q_v (a) and the u and v components of the velocity (b) at time t = 0 h (bold = 3 h (dotted lines), and t = 7 h (dashed lines). The circles and squares are the observed values. The thin line in (b) is the p geostrophic wind profile.

This period was chosen for a model intercomparison (Siebesma et al. 2002, *J. Atmos. Sci.*, in press), so eight LES models were run on the same case. Figure 2 shows the mean cloud fraction vs. height. The line is the mean, the grey shows intermodel variability (which is pretty small in this case). As is typical in shallow cumulus ensembles, cloud fraction is small at all levels, and decreases with height. Due to vertical shearing of the clouds, the fraction of grid columns with cloud is about 15%, which is larger that the cloud fraction at any height. 'Cores' indicate positively buoyant cloud; even within the conditionally unstable layer about 50% of the cloud is negatively buoyant as a result of mixing with the environment and consequent evaporative cooling of the mixed air. This is also clear in the θ_v profiles of clouds and cores shown in Fig. 2b. These show that even though the stratification is much more unstable than a moist adiabat, on average the clouds are only marginally buoyant. Of course, this is an average over all clouds during all phases of their lifecycle, and small amounts of nearly undilute air can be found at all levels, helping to form the most buoyant and penetrative cumulus updraft that set the upper limit of the inversion. .

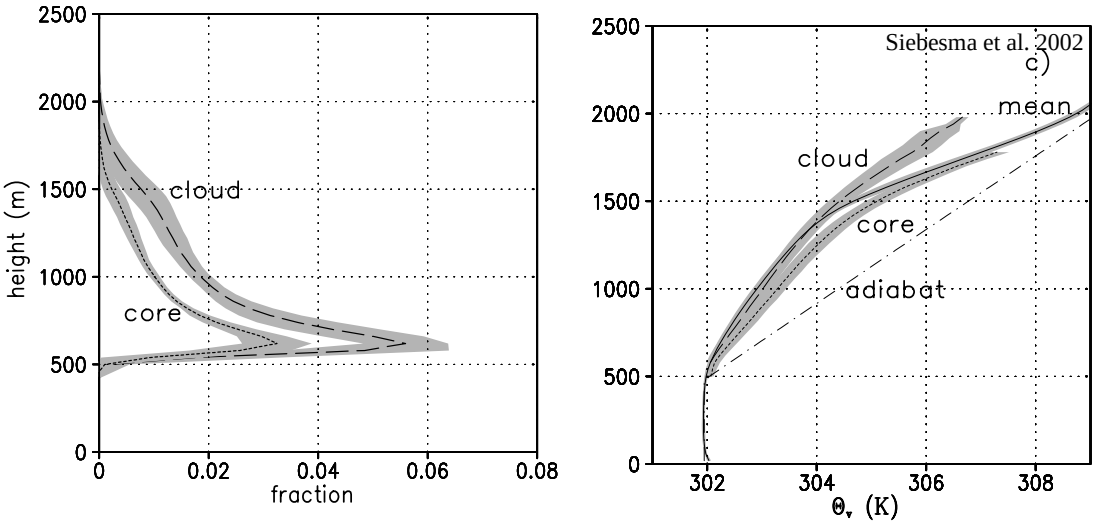

Fig. 2. LES shallow Cu profiles of (a) cloud fraction and (b) θ_v

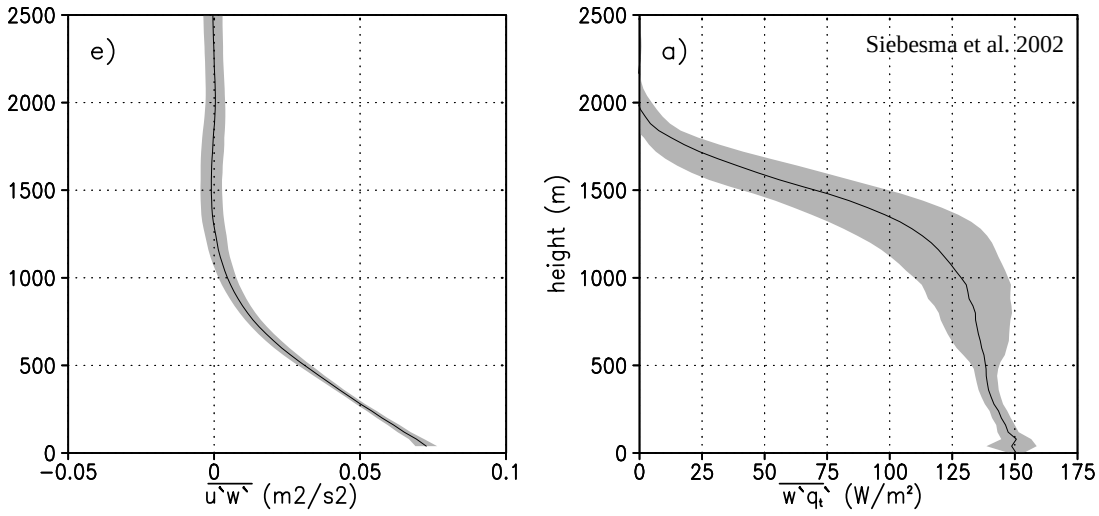

Fig. 3. LES-derived momentum and total water flux profiles.

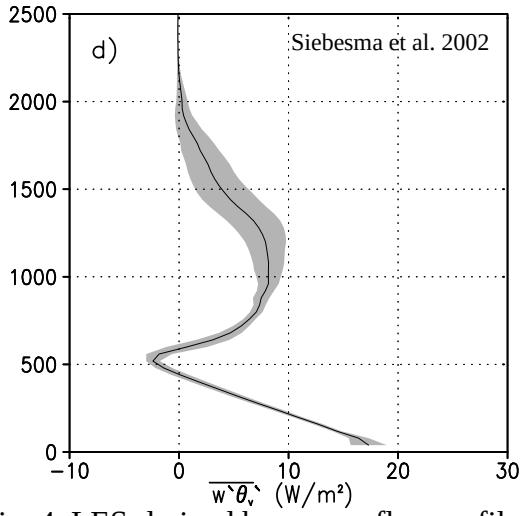

Fig. 4. LES-derived buoyancy flux profile.

The transport properties of the clouds are seen in Fig. 3, which show the LES-derived momentum, and moisture flux profiles. The momentum fluxes are largest in the subcloud layer, but are significant in the cumulus layer as well. Most of the moisture evaporated at the surface is fluxed by cumulus clouds into the inversion, where it moistens the above-inversion air being entrained into the BL. Figure 4 shows the buoyancy flux profile. Beneath the clouds it looks nearly identical to a dry convective BL, with an entrainment zone at cloud base. The buoyancy flux is positive in the conditionally unstable layer. More surprising, it remains positive even in the inversion layer, where the cumuli are overshooting their levels of neutral buoyancy. This is due to sub-cloud scale eddies..

Subcloud layer

Figure 5 shows an idealization of air parcel circuits in a shallow Cu boundary layer. We start with the subcloud layer. Typically there is fairly uniform dry convection within this layer with eddy velocities of less than 1 m s^{-1}, driven by surface buoyancy fluxes associated with air that is slightly colder than the ocean surface. Within the subcloud layer, the circuit of θ_v shows slight ra-

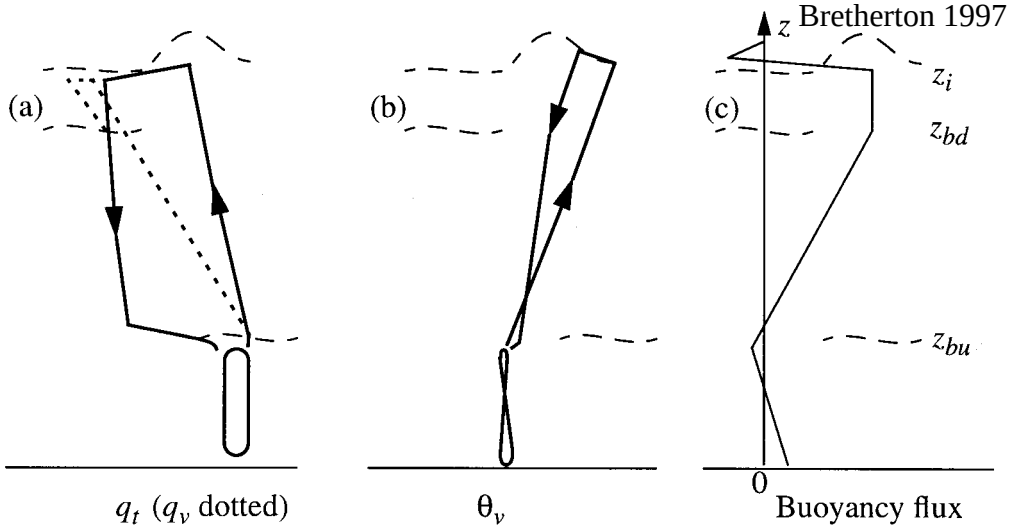

Figure 5.. Parcel paths in a shallow Cu BL capped by thin Sc.

diative cooling both as air ascends in the updraft and descents in the downdraft. The air experiences moistening and slight warming by surface fluxes and drying and slight warming by entrainment of warmer air at the top of the subcloud layer.

Transition layer

The top of this dry convection zone is marked by the weak stable transition layer (marked by a θ_v increase of a few tenths of a K), which is near the cumulus cloud base. Most of the convective updrafts in the subcloud layer do not have sufficient inertia and buoyancy to penetrate through the transition layer; this is indicated by separating the branch of the circulation that goes up into cumulus clouds from the subcloud layer circuit. In fact, it is useful to think of the transition layer as a 'valve' which regulates the number of cumuli so as to keep the top of the subcloud mixed layer close to the cumulus cloud base. This valve is subject to very rapid feedback. Were the transition layer initially above the mean LCL of subcloud air , many updrafts would form clouds on top, and the resulting latent heating would allow these updrafts to penetrate the transition layer to form cumuli. In order for lots of mass to ascend in these cumuli, a comparably large amount of mass would have to descend around the clouds ('compensating subsidence'), bringing down higher θ_v air from the upper part of the cumulus layer. This would lower and strengthen the transition layer inversion. On the other hand, were the transition layer initially well below the mean LCL of subcloud air, then no updrafts could become saturated before they become negatively buoyant. The subcloud layer would then deepen rapidly due to entrainment (a typical subcloud layer entrainment rate is about 1-2 cm s^{-1}) until the tops of updrafts start developing into Cu clouds. In equilibrium, the transition layer regulates the mass flux from the subcloud layer vented into Cu to roughly balance entrainment such that the top of the subcloud layer remains close to its LCL.

Conditionally unstable layer

Inside active cumuli, air rises vigorously through the conditionally unstable layer in turbulent updrafts of 1-5 m s^{-1} . Outside the cumuli, air is slowly subsiding (indicated by downward arrows in the circuits of q_t and θ_v) at an average rate of around 1-2 cm s^{-1} and is considerably drier than the cumulus updrafts. Mass balance implies that the cumulus updrafts comprise only about 1% of the total area at any height. Lateral entrainment of the drier ambient air by the updrafts decreases their mean q_t as they rise. Many smaller cumuli may never reach the top of the cumulus layer. These cumuli detrain moist air into the lower and middle parts of the cumulus layer, moistening the subsiding air slightly as it descends. Penetrative entrainment by cumuli mixes in warm dry air from within the inversion layer, so that the air detrained from the clouds (from which the subsiding branch of the circulation is composed) is much drier than the updraft air before it begins to subside. The resulting evaporation of cloud water also makes the detrained air less buoyant than the cloudy updrafts. As the air subsides, it cools radiatively, creating a stratification of θ_v.of around

$$d\theta_v/dz \approx \text{(radiative cooling rate)/(subsidence rate)} \approx (2\text{ K}/10^5\text{ s})/(1\text{-}2\text{ cm s}^{-1}) = 1\text{-}2\text{ K/km}$$

This is less than the moist adiabatic lapse rate, maintaining conditional instability within the cumulus layer.

When the subsiding air reaches the cumulus cloud base, it is entrained back into the much moister subcloud layer. The typical circulation time for air to rise a height of 1 km or so within a cumulus cloud, then sink back to the subcloud layer is

$$\tau_{Cu} = 1\text{ km}/(1\text{-}2\text{ cm s}^{-1}) = 0.5\text{-}1\times10^5\text{s} \approx 0.5\text{-}1\text{ day}$$

This is much longer than the 20 minute circulation time of a typical stratocumulus-capped mixed layer.

Capping Inversion

In a Cu-topped BL the capping inversion is be a stably stratified layer up to 500 m thick, over which θ_v increases by 1-5 K. Air subsiding into this inversion is subject to penetrative mixing with the most vigorous Cu updrafts. A spectrum of mixtures is created, all of which are cooler than the ambient inversion air due mainly to evaporative cooling. The most dilute of these mixtures remain within the inversion layer, causing a systematic cooling and moistening of air lower in the inversion layer, while the more strongly cooled mixtures detrain below the capping inversion.

Role of radiative forcing

Over land, the dominant thermodynamic forcing for shallow cumulus convection is surface buoyancy fluxes, augmented by latent heating within the cumulus clouds. Over the oceans, longwave radiative cooling within the boundary layer is often dominant. Shallow cumulus clouds have a typical fractional sky cover of 10-30% and a cloud fraction which is largest near the cloud base. Longwave cooling is due both to clear air and cloud sides and tops at various heights within the BL, and is distributed fairly uniformly throughout the BL, typically with cooling rates of 2 K day^{-1} or so in the subtropics, if there is no overlying stratiform cloud. Over the midlatitude and colloer subtropical oceans, where the capping inversion is stronger, shallow cumuli are commonly overlain by a thin, possibly patchy stratocumulus layer. In this case, there is a strong radiative flux divergence (cooling) at the stratocumulus cloud top and little flux divergence lower in the BL. In both cases, shortwave absorption in the clouds and clear air reduces the cooling somewhat during the day, so convection tends to be a little more vigorous at night.

For a 500 m deep boundary layer, the net diurnally averaged radiative flux divergence would typically be around 40-50 W m^{-2}, and 10 W m^{-2} if there is no cloud, so cloud greatly increases the overall BL cooling. For a 2 km deep BL typical of subtropical trade wind cumulus regimes, the typical flux divergence would be 40-50 W m^{-2} with or without cloud on top. For the deeper BL, cloud alters mainly the *distribution* of cooling within the BL, not the total amount. By comparison, surface virtual heat (buoyancy) flux tends to be only about 10 W m^{-2} over the subtropical oceans, while (though latent heat fluxes are 100-200 W m^{-2}).

Shallow Cu layers topped by Sc

Large regions of the ocean are covered by CTBLs intermediate between the Sc-topped mixed layer and the shallow Cu BLs. These BLs have a layer of Cu rising into patchy Sc. This structure is favored when the Cu layer is less than 1 km deep. In this case, the Cu updrafts tend to be less vigorous, limiting penetrative entrainment and there is less depth for them to be diluted by lateral entrainment, so the air detrained by Cu beneath the trade inversion is moist and still contains liquid water. Thus, the Sc are formed due to detrainment of liquid water from the Cu. Hence, this type of BL is sometimes called *cumulus-coupled.* The main modifications to the circulation compared to a pure shallow Cu BL are due to the radiative effects of the Sc. First, the strong radiative cooling atop the Sc helps induce turbulence within and below the Sc layer and adds a component of entrainment into the BL by the Sc. Second, there is little radiative cooling below the Sc to cool subsiding air. Hence, the stratification in the Cu layer tends to be very weak. This permits the radiatively driven turbulence induced by the Sc to extend well below the cloud layer. In fact, it is common to see a nearly well-mixed thermodynamic profile from the inversion down nearly all the

way to the transition layer, with a jump of 1-3 g kg^{-1} in mixing ratio across the transition layer.

This structure cannot persist if the BL is deeper, because it is highly conditionally unstable. Hence, if the BL is deep, the Cu updrafts would become very vigorous, forcing extensive penetrative entrainment of dry air from above the inversion, and evaporating the Sc layer. Wyant et al. (1997, JAS) demonstrate this feedback in a numerical model simulation. A conceptual model of the entire transition from subtropical stratus to cumulus capped CTBLs is presented in Figure 6.

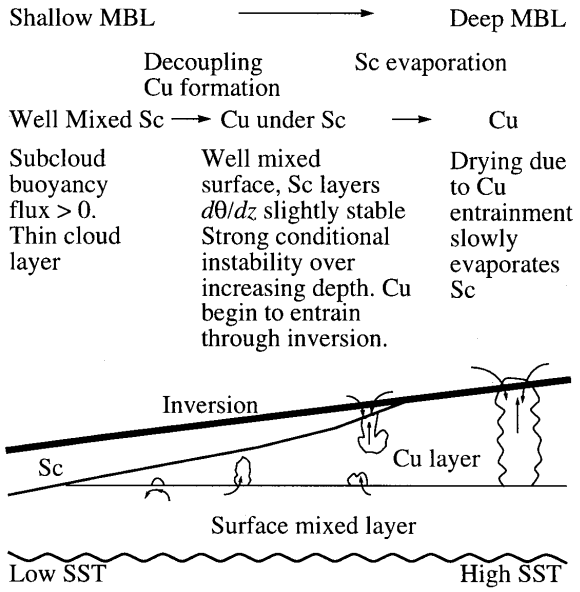

Fig. 6. A conceptual model of the subtropical stratocumulus to trade Cu transition

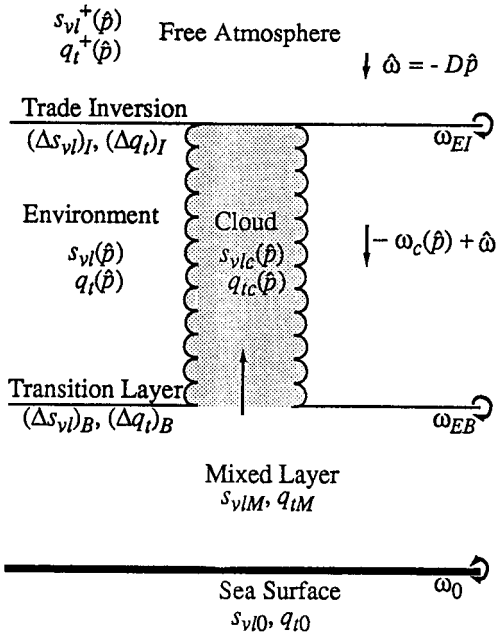

Fig. 7. Parameterized view of shallow Cu BL.

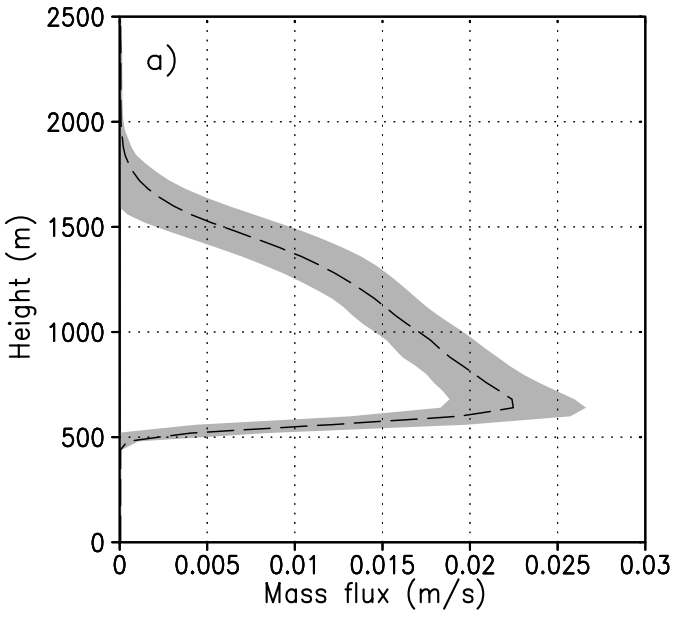

Fig. 8. LES shallow Cu core mass flux profile

Mass-flux parameterization of shallow Cu

A common approach for parameterizing shallow cumulus boundary layers is to treat the cloud ensemble as one aggregate homogeneously mixed plume that laterally entrains and detrains at each height (Fig. 7). Some parameterizations use ensembles of plumes to better represent the spectrum of observed cloud sizes; others consider a spectrum of mixtures that can be created by mixing updraft air with environmental air, and incorporate only sufficiently buoyant mixtures into the plume while detraining the rest ('buoyancy sorting'). A single entraining/detraining plume seems to capture the fluxes transported by a shallow convective layer fairly well. By looking at profiles of cumulus updraft mass flux (Fig. 8) and the dilution of an average cloud with height (fig. 2b) one can diagnose the required entrainment and detrainment rates from LES (Siebesma and Cuijpers, *J. Atmos. Sci.*, 1995).

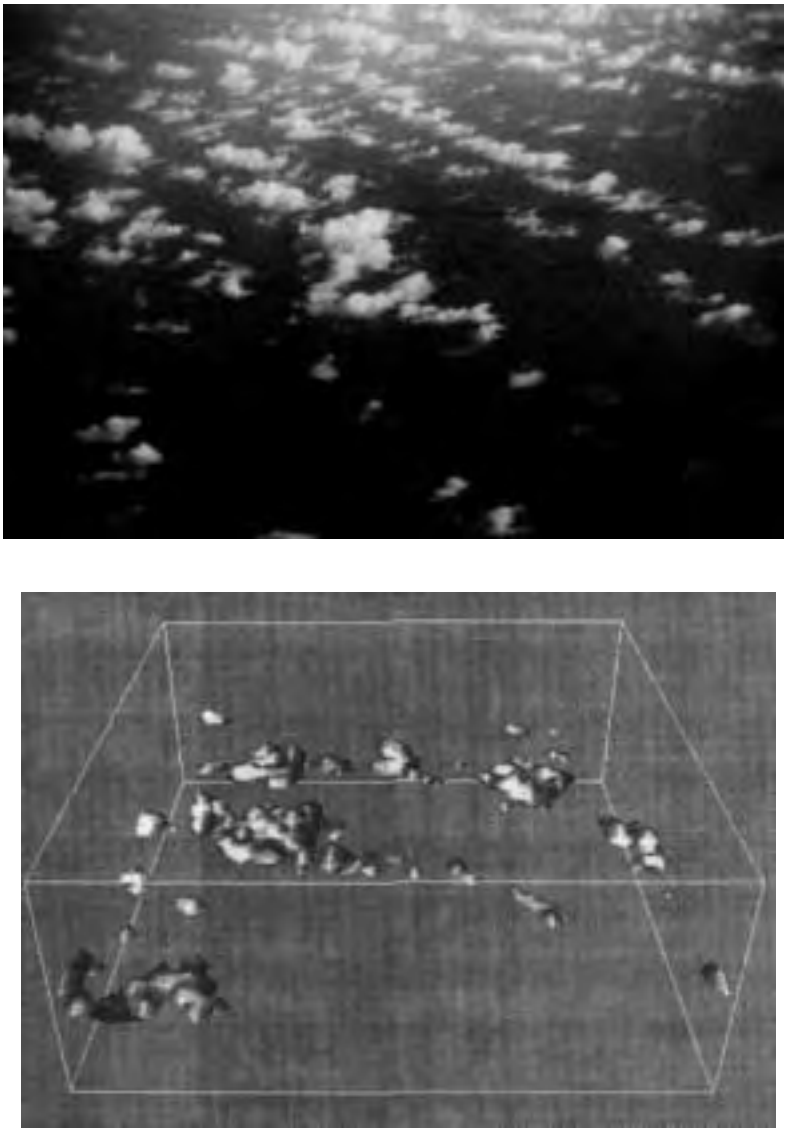

Fig. 9. Aerial view of BOMEX trade Cu and LES simulation of BOMEX cloud field.